UC San Diego
UC San Diego Electronic Theses and Dissertations

Title
Design of Robust, Low-Threshold Wavelength-Scale Nanolasers using Optical and Thermal Analysis

Permalink
https://escholarship.org/uc/item/3dp701hk

Author
Shane, Janelle Claire

Publication Date
2014

Peer reviewed|Thesis/dissertation

eScholarship.org Powered by the California Digital Library
University of California

UNIVERSITY OF CALIFORNIA, SAN DIEGO

Design of Robust, Low-Threshold Wavelength-Scale Nanolasers using Optical and Thermal Analysis

A dissertation submitted in partial satisfaction of the
requirements for the degree
Doctor of Philosophy

in

Electrical Engineering (Photonics)

by

Janelle Claire Shane

Committee in charge:

Professor Yeshaiahu Fainman, Chair
Professor Prabhakar Bandaru
Professor Vitaliy Lomakin
Professor Andrea Tao
Professor Paul Yu

2014

Copyright
Janelle Claire Shane, 2014
All rights reserved.

The dissertation of Janelle Claire Shane is approved, and it is acceptable in quality and form for publication on microfilm and electronically:

____

____

____

____

____

Chair

University of California, San Diego

2014

EPIGRAPH

Horses like to run.
And talk to the others.
It is funto ouna horse i bet.
I like horses.

I bet you like horses too.
This is another horse.
A pony.
What is a pony?
A horse that is very pretty.
This is one.

Horses put there sharp heels up and but around the other horses.
That is called galloping.

Ask your mom or dad to take you to the zoo.
That is a good place to get a look.
Tri to see a horse in real life.
I have seen a horse in real life.
Tri to.

—Janelle Shane, age 6, first published academic work (excerpt)

TABLE OF CONTENTS

Signature Page iii

Epigraph iv

Table of Contents v

List of Acronyms viii

List of Nomenclature ix

List of Figures xi

List of Tables xiii

Acknowledgements xiv

Vita xv

Abstract of the Dissertation xvii

Chapter 1 Introduction 1
- 1.1 Motivation: nanolasers for chip-scale optical communication . . 1
- 1.2 Wavelength-scale nanolasers 2
  - 1.2.1 The challenges of subwavelength operation and room-temperature electrical injection 2
- 1.3 Metal-clad subwavelength semiconductor lasers (MCSELs) . . . 4
- 1.4 Toward robust operation and higher output power 5
- 1.5 The work in this dissertation 6
- 1.6 Acknowledgements 7

Chapter 2 Optical simulation 8
- 2.1 Introduction 8
- 2.2 Finite element analysis using COMSOL 8
  - 2.2.1 Model construction 8
  - 2.2.2 Meshing the model 10
  - 2.2.3 Solving the model 10
- 2.3 Automation 11
  - 2.3.1 Assigning subdomains 11
  - 2.3.2 Identifying boundaries 12
  - 2.3.3 Processing optical simulation results 12
  - 2.3.4 Building input files for SILVACO simulation 13

Chapter 3 Thermal considerations in electrically-pumped metallo-dielectric subwavelength nanolasers . . . 14
3.1 Introduction . . . 14
3.2 Thermal model overview . . . 15
3.3 Self-heating sources . . . 17
3.3.1 Joule heating . . . 18
3.3.2 Junction heating . . . 20
3.3.3 Heterojunction heating . . . 20
3.3.4 Surface recombination heating . . . 21
3.3.5 Auger recombination heating . . . 22
3.4 Heat dissipation . . . 22
3.5 Discussion . . . 25
3.6 Acknowledgements . . . 26

Chapter 4 Amorphous Al_2O_3 shield for thermal management in electrically pumped metallo-dielectric nanolasers . . . 28
4.1 Abstract . . . 28
4.2 Introduction . . . 29
4.3 Device fabrication and characterization . . . 32
4.4 Device analysis - optical . . . 37
4.5 Device analysis - electrical and thermal . . . 40
4.6 Cavity design for room-temperature operation . . . 44
4.7 Discussion . . . 47
4.8 Acknowledgements . . . 49

Chapter 5 Effect of undercut etch on performance and fabrication robustness of metal-clad semiconductor nanolasers . . . 51
5.1 Abstract . . . 51
5.2 Introduction . . . 52
5.3 Optical simulation . . . 54
5.3.1 Effect of sidewall tilt on threshold gain for lasers without undercut . . . 54
5.3.2 Effect of undercut etching on threshold gain for lasers with sidewall tilt . . . 56
5.4 Electrical and thermal simulation . . . 63
5.4.1 Ohmic resistance . . . 63
5.4.2 Self-heating . . . 65
5.4.3 Operating temperature . . . 67
5.5 Conclusion . . . 69
5.6 Acknowledgements . . . 72

Chapter 6 Effect of dielectric shield material choice on metal-clad nanolaser optical and thermal performance . . . 73
6.1 Introduction . . . 73
6.2 Optical simulation . . . 75
6.3 Thermal simulation . . . 79

6.4 Conclusion . . . 84
6.5 Acknowledgements . . . 85

Chapter 7 Conclusion and future work . . . 86
7.1 Conclusion . . . 86
7.2 Identification of additional factors affecting nanolaser performance 87
7.2.1 Pedestal shape . . . 87
7.2.2 Cladding shape and thickness . . . 88
7.2.3 Detailed simulation of fabricated lasers . . . 89
7.3 Closed-loop multidomain simulation . . . 90
7.4 Experimental measurement of laser operating temperature . . . 91
7.5 Investigation of strain gradients . . . 92
7.6 Acknowledgements . . . 92

Bibliography . . . 93

LIST OF ACRONYMS

ALD	atomic layer deposition
CW	continuous wave
DC	direct current
HSQ	hydrogen silsesquioxane
MCSEL	metal-clad subwavelength semiconductor laser
MOSFET	metal-oxide-semiconductor field-effect transistor
MQW	multiple quantum well
PECVD	plasma-enhanced chemical vapor deposition
QFL	quasi Fermi level
RF	radio frequency
RIE	reactive ion etching
SEM	scanning electron microscopy
SPP	surface plasmon polariton
TE	transverse electric
TM	transverse magnetic
TMA	trimethylaluminum
VCSEL	vertical cavity surface emitting laser
WGM	whispering gallery mode

LIST OF NOMENCLATURE

A	Auger coefficient
A_{active}	surface area of the active region
C_p	heat capacity
ϵ	relative permittivity
Γ	confinement factor
g_{th}	modal threshold gain
I	current
I_{inj}	injected current
I_{th}	threshold current
k	thermal conductivity
λ_0	free-space wavelength
μ	carrier mobility
M	azimuthal mode number
n	carrier density
P_a	heating power generated from Auger recombination
P_{jn}	heating power dissipated at junction
P_s	heating power generated from surface recombination
Q	quality factor
ρ	material density
R	Ohmic resistance
Δr_{lower}	difference between r_{core} and r_{lower}
r_{core}	average radius of gain core
r_{lower}	average radius of lower pedestal
σ	conductivity
τ_s	surface recombination carrier lifetime
T_{amb}	ambient temperature
T_c	thermal conductivity
T_{ss}	steady-state temperature
undercut	difference between r_{core} and r_{lower}, as percentage of r_{core}
undercut ratio	ratio between average radius of upper and lower pedestal
U_a	Auger recombination rate
U_s	rate of surface recombination

υ_s	surface recombination velocity
V_{active}	volume of the active region
V_{jn}	junction voltage

LIST OF FIGURES

Figure 1.1: Diagram of a basic electrically-pumped laser cavity 3
Figure 1.2: Material gain spectra with temperature as a parameter 4

Figure 2.1: Diagram of an example nanolaser 9

Figure 3.1: Diagram of electrically-pumped nanolaser to be analyzed 16
Figure 3.2: Result of electronic simulation 20
Figure 3.3: Amount and location of heating sources 23
Figure 3.4: Boundary conditions used in heat transport simulation 24
Figure 3.5: Calculated steady-state operating temperature 25

Figure 4.1: A schematic of the electrically pumped nanolaser 33
Figure 4.2: SEM images of pedestal pillar lasers 34
Figure 4.3: Measured device performance at an ambient temperature of 77K . . . 36
Figure 4.4: Electrical simulation results 41
Figure 4.5: Temperature distribution 42
Figure 4.6: Room-temperature optical simulation results for laser with undercut . 44
Figure 4.7: Temperature distribution, maximum steady-state temperature, and heat flux of the designed device 45
Figure 4.8: Material gain spectrum 47

Figure 5.1: Diagram of an example simulated nanolaser... 53
Figure 5.2: Effect of sidewall angle on lasers without undercut 56
Figure 5.3: SEM images of three example nanolasers 58
Figure 5.4: Effect of undercut on threshold gain... 59
Figure 5.5: Effect of increasing undercut amount on the characteristics of the lowest-threshold mode 60
Figure 5.6: Reflection coefficient of the lower pedestal 61
Figure 5.7: Effect of undercut etch on Ohmic resistance and electric field 64
Figure 5.8: Amount of Auger, surface recombination, Joule, and junction + heterojunction self-heating... 68
Figure 5.9: Laser steady-state operating temperature 70

Figure 6.1: Diagram of an example metal-clad nanolaser 74
Figure 6.2: Simulated threshold gain (a, b) and mode wavelength (c, d) 76
Figure 6.3: Behavior of laser with r_{core}=225nm and SiO_2 shield of thickness 50nm - 300nm 77
Figure 6.4: g_{th} of lowest-threshold modes for r_{core}=225nm laser with AlN shield . 78
Figure 6.5: Amount and locations of heat sources 81
Figure 6.6: teady-state temperature distribution at 1mA pump current 82
Figure 6.7: Maximum steady-state temperature of the gain region 83

Figure 7.1: An electrically pumped nanolaser before (a) and after (b) deposition of metal cladding 88

Figure 7.2: SEM images (a, c) and COMSOL model geometries (b, d) of two fabricated lasers . . . 89
Figure 7.3: Resonant wavelength of selected modes . . . 91

LIST OF TABLES

Table 3.1: Dimensions and material parameters of MCSEL laser 17
Table 3.2: Material thermal parameters 23

Table 4.1: Optical and thermal properties of materials 31
Table 4.2: Simulated optical mode characteristics at 77K 38
Table 4.3: Optical mode simulation of the lasing cavity mode 39
Table 4.4: Simulated optical characteristics of the lowest-threshold gain mode of the designed device 46

Table 6.1: Material parameters used in optical and thermal simulations 80

ACKNOWLEDGEMENTS

I would like to thank Prof. Shaya Fainman for his support as my adviser, through several years and several research projects.

I'd also like to thank the UNO research group for their mentoring and friendship, particularly my officemates Qing Gu and Olesya Bondarenko.

The support of my friends and family has been vital - huge thanks to you all.

Chapter 1, in part, is a reprint of material currently accepted for publication in Nanophotonics Journal, 2014. Qing Gu, Joseph ST Smalley, Janelle Shane, Olesya Bondarenko and Yeshaiahu Fainman. (2014) The dissertation author was an author of this review paper.

Chapter 3, in full, is a reprint of the material as it appears in The Proceedings of SPIE, 2014. Janelle Shane, Qing Gu, Felipe Vallini, Brett Wingad, Joseph S. T. Smalley, Newton C. Frateschi, and Yeshaiahu Fainman. (2014) The dissertation author was the primary investigator and author of this paper.

Chapter 4, in full, is a reprint of the material as it appears in IEEE Journal of Quantum Electronics, 2014. Qing Gu, Janelle Shane, Felipe Vallini, Brett Wingad, Joseph S. T. Smalley, Newton C. Frateschi, and Yeshaiahu Fainman. (2014) The dissertation author was the second investigator and author of this paper, and performed the optical and thermal simulation work.

Chapter 5, in part is currently being prepared for submission for publication of the material. Shane, Janelle; Gu, Qing; Fainman, Yeshaiahu. The dissertation author was the primary investigator and author of this material.

Chapter 6, in part is currently being prepared for submission for publication of the material. Shane, Janelle; Gu, Qing; Fainman, Yeshaiahu. The dissertation author was the primary investigator and author of this material.

VITA

2007	B. S. in Electrical and Computer Engineering *honors*, Michigan State University
2009	M. Phil in Physics, University of St Andrews, Scotland
2014	Ph. D. in Electrical Engineering (Photonics), University of California, San Diego

PUBLICATIONS

Qing Gu, Joseph ST Smalley, Janelle Shane, Olesya Bondarenko and Yeshaiahu Fainman, *"Temperature effects in metal-clad semiconductor nanolasers,"* Nanophotonics Journal, (Accepted).

Qing Gu, Janelle Shane, Felipe Vallini, Brett Wingad, Joseph ST Smalley, Newton C. Frateschi and Yeshaiahu Fainman, *"Amorphous Al2O3 shield for thermal management in electrically pumped metallo-dielectric nanolasers,"* IEEE Journal of Quantum Electronics 15, 7, p.499-509 (2014).

O. Bondarenko, Q. Gu, J. Shane, A. Simic, B. Slutsky, and Y. Fainman, *"Wafer bonded distributed feedback laser with sidewall modulated Bragg gratings,"* Appl. Phys. Lett. 103, 043105 (2013).

J. Shane*, M. Mazilu*, W. M. Lee, and K. Dholakia. *"Effect of pulse temporal shape on optical trapping and impulse transfer using ultrashort pulsed lasers."* Optics Express 18, 7 (2010). *Equal contribution

J. Shane, V. Lozovoy, and M. Dantus. *"Binary search space mapping: Getting a picture of coherent laser control."* Journal of Physical Chemistry A 110, 40 (2006).

D. A. Harris, J. Shane, V. Lozovoy, and M. Dantus, *"Automated phase characterization and adaptive pulse compression using Multiphoton Intrapulse Interference Phase Scan in air,"* Optics Express, 15, 1932-1938 (2007).

V. Lozovoy, X. Zhu, T. Gunaratne, D. A. Harris, J. Shane, and M. Dantus, *"Control of molecular fragmentation using binary phase-shaped femtosecond laser pulses,"* Journal of Physical Chemistry A 7, 2471-2473 (2006).

V. Lozovoy, J. Shane, B. Xu, and M. Dantus. *"Selective nonlinear excitation with pseudorandom Galois fields."* Physics Review A 74, 4 (2006).

L. Schelhas, J. Shane, and M. Dantus. *"Advantages of ultrashort phase-shaped pulses for selective two-photon activation and biomedical imaging,"* Journal of Nanomedicine 2, 3, 177-181 (2006).

V. Lozovoy, T. Gunaratne, J. Shane, and M. Dantus, *"Control of chemical reactions using binary phase shaped femtosecond laser pulses,"* ChemPhysChem, 7, 2471-2473 (2006).

V. Lozovoy, J. Shane, B. Xu, and M. Dantus. *"Spectral phase optimization of femtosecond laser pulses for narrow-band, low-background nonlinear spectroscopy."* Optics Express 13, 10882-10887 (2005).

ABSTRACT OF THE DISSERTATION

Design of Robust, Low-Threshold Wavelength-Scale Nanolasers using Optical and Thermal Analysis

by

Janelle Claire Shane

Doctor of Philosophy in Electrical Engineering (Photonics)

University of California, San Diego, 2014

Professor Yeshaiahu Fainman, Chair

Wavelength-scale nanolasers are a crucial component of future photonic systems integrated on chip. As nanolasers progress from their first proof-of-concept demonstrations to robust designs working at room temperature far above their lasing threshold, their thermal behavior, as well as the effects of fabrication imperfections, need to be better understood. This dissertation presents the first integrated optical, electrical, thermal, and material analysis of wavelength-scale nanolaser performance, and uses these results to analyze a failed laser design, as well as to suggest design changes to improve robustness and performance. The dissertation begins by describing methods for optical and thermal analysis, including methods to automate long sweeps of operating current and/or geometry parameters. Next, a nanolaser with poor laboratory performance is analyzed, and the performance-limiting parameter is found not to be thermal issues, as had been

expected, but the sloped sidewalls of the fabricated laser. The next chapter expands the analysis of sloped sidewalls and finds that, although this effect is very detrimental to laser performance, an increase in the amount of undercut etching can render the laser insensitive to sidewall slope, with no significant Joule heating penalty near threshold. Finally, the analysis of laser performance is applied to lasers designed to operate well above threshold, showing the thermal benefits of using heat-conducting dielectric shield layers, and analyzing the effect of shield material choice on optimal shield thickness.

Chapter 1

Introduction

1.1 Motivation: nanolasers for chip-scale optical communication

As the world's economy demands ever-higher rates of data transfer, the limitations of electronics for high-speed communication become an increasing problem. Already these limitations have prompted a shift from electronic-based transmission lines to fiber optics, first for long-distance data transmission, and then for shorter-distance transmission within datacenters. As data transmission rates continue to rise, efforts have turned toward using optical communication for even shorter distances, between and even within computer chips, with light sources, modulators, guides, and detectors all incorporated on the same chip. A recent postdeadline paper by researchers at IBM and Aurrion stated that "over the past decade, silicon photonics has transformed from a fringe research topic in specialty conferences to being viewed as the key solution to meeting the demands of next generation telecom and datacom systems" [1].

The integration of an optical communication network onto a single chip requires great research effort toward miniaturization of the optical components, similar to the effort that has led to the extensive miniaturization of electronic components. For applications involving communication in a photonics layer between different components on the same chip, the photonic components must be comparable in size to the electronic components, and must interfere minimally with each other when densely packed.

Of the components of an optical communication network, one of the most crucial and difficult to miniaturize for dense chip-scale networks is the light source. A common

approach in current integrated silicon photonics modules has been to integrate everything but the laser onto the chip, and bring in the laser light from a larger, off-chip source, treating the laser as a power supply. Recent advances use laser directly integrated with silicon waveguides; however, these lasers usually have large footprints, with cavities that are hundreds of microns to millimeters in length[1, 2, 3], or modes that spill out of the cavity, preventing these lasers from being densely packed[2]. Reliable nanolasers with much smaller footprints will be needed to enable dense integration of light sources for chip-scale optical communication.

1.2 Wavelength-scale nanolasers

1.2.1 The challenges of subwavelength operation and room-temperature electrical injection

The lasers currently used in optical communication networks typically operate in the telecom wavelength range of around 1530-1565nm, sometimes known as the C-band, a range in which the absorption of silicon and silicon dioxide are minimal. A micron or sub-micron device footprint would require these lasers to be subwavelength in size, smaller than the free-space wavelength of light they emit. In this regime, interesting physical effects emerge[4, 5, 6]. However, building a working laser of this size poses a significant engineering challenge. Many of the requirements for a laser to be a practical light source become difficult at these sizes: room-temperature operation, electrical (rather than optical) injection of carriers, and a low operating current.

To see why these difficulties arise, consider a basic laser, consisting of a gain medium that amplifies light, and a cavity that confines the amplified light, sending it back into the gain medium for additional amplification (Fig. 1.1). Both of these aspects of laser operation - amplification and confinement - become difficult at very small cavity sizes.

Amplification becomes a problem because of the high surface-to-volume ratio of the gain region in wavelength-scale cavities. The surface of the gain region is prone to damage during fabrication, and to other sources of surface defects that cause carriers to recombine rather than to undergo stimulated emission and emit light[7, 8]. Consequently, much of the injected current is wasted to surface recombination losses, so the laser requires a higher injection current to reach lasing threshold. Surface recombination produces heat,

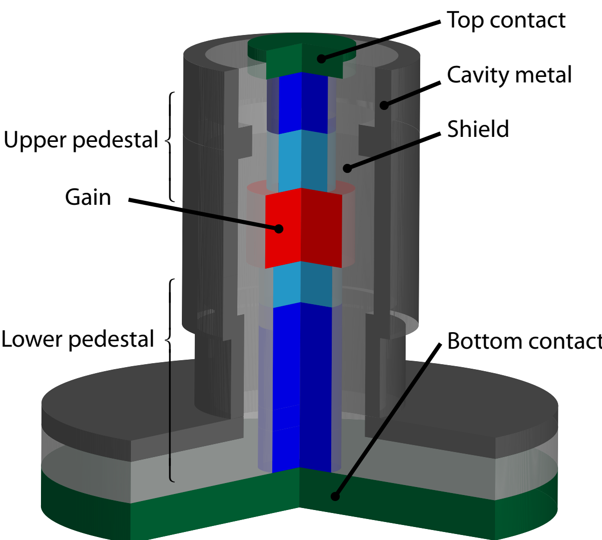

Figure 1.1: Diagram of a basic electrically-pumped laser cavity, showing the gain region (red) and the metal that surrounds the laser (dark grey), creating the cavity. Above and below the gain region are pedestal layers designed to conduct electricity through the laser (blue). Top and bottom contacts are shown in green.

which can help to raise the operating temperature of the laser above ambient temperature. The heating problems associated with surface recombination are exacerbated by other sources of self-heating that worsen for smaller lasers; one of the most significant is Joule heating, caused by the injection of current through the narrow nanolaser diameter. At these higher operating temperatures, the effectiveness of the gain material decreases, requiring even larger numbers of injected carriers to reach the same material gain levels (Fig. 1.2). In addition, metals absorb more light at higher temperatures, meaning that for a laser that uses metal as part of the cavity, metal absorption becomes an increasing problem[9]. At even higher operating temperatures, the materials in the laser may melt or crack. The problems associated with higher operating temperatures are the reason why many initial demonstrations of nanoscale lasers have taken place under cryogenic cooling.

Another major problem for wavelength-scale lasers is that of confinement of light to the cavity, with the challenge of balancing strong confinement with a small overall device footprint without introducing other forms of loss.

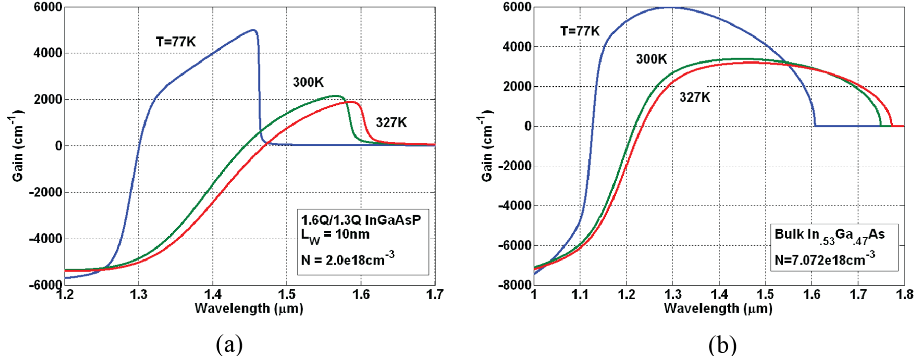

Figure 1.2: Material gain spectra with temperature as a parameter for (a) 10nm 1.6Q/1.3Q InGaAsP QW with carrier density of N=2.0e18 cm^{-3} and (b) bulk $In_{0.53}Ga_{0.47}As$ with carrier density of N=7.072e18 cm^{-3}.

1.3 Metal-clad subwavelength semiconductor lasers (MCSELs)

A variety of nanolaser designs have been demonstrated and/or proposed to address some of the challenges listed above. Although many promising classes of laser design exist, such as microdisk lasers[10, 11, 12, 13], nanowire/nanorod lasers[14, 15], nanomembrane lasers[16], and photonic crystal lasers[17], we focus here on lasers that have been demonstrated with mode and cavity dimensions that are subwavelength in all three dimensions. These designs use metal to achieve high mode confinements without the use of large Bragg or photonic crystal structures.

The optical modes of metal-clad cavities can be grouped into two main categories, namely surface plasmon polariton (SPP) modes and photonic modes. SPP modes rely on the extremely small wavelength of surface plasmons traveling through metal to tightly concentrate the optical mode. Plasmonic structures can confine the mode to areas that are deeply subwavelength in size, allowing the use of extremely small gain volumes. However, a relatively high mode overlap with metal is required, bringing with it a high degree of metal absorption loss. Furthermore, the best mode confinements occur at wavelengths near the plasmon resonance, where metal is extremely lossy. Metal loss has been a major limitation of plasmonic lasers, and both the problems of metal loss and high gain threshold are exacerbated at higher temperatures. Consequently, although cryogenic temperature operation has been demonstrated[7, 18], the high threshold gain of SPP modes in such cavities has prevented lasing at room temperature.

In the case of photonic modes, the mode overlap with the metal is usually much smaller than that of SPP modes. Hence, photonic lasing modes typically have higher Q-factors and lower threshold gain values, albeit at the expense of reduced mode confinement. This dissertation will focus on metal-clad photonic-mode lasers, which have recently been demonstrated operating at room temperature under CW electrical injection[19].

1.4 Toward robust operation and higher output power

Since the first demonstration of a subwavelength metal-clad nanolaser in 2007 by Hill and colleagues[7], researchers have worked to increase the suitability of these lasers for dense chip-scale integration. One major challenge is that of room-temperature operation, or even tolerance of ambient temperatures higher than room temperature, due to the worsening of metal loss and gain material performance, as described in Section 1.2.1. Another challenge is that of operation under CW electrical pumping, as opposed to pulsed electrical pumping or optical pumping.

The subwavelength nanolaser demonstrated by Hill and colleagues [7] was CW electrically pumped, but operated at 77K due to the high overlap of the mode with metal. The use of a thicker dielectric layer to isolate the mode from the metal enabled Nezhad and colleagues to achieve room temperature operation[20, 21] under pulsed optical pumping. Later work by the same group led in 2011 to a subwavelength CW electrically pumped laser demonstrated operating at 100K by Lee and colleagues (a larger laser operated at 140K), using a wet etching process to isolate the mode from the substrate[22]. In 2012, Ding and colleagues demonstrated room-temperature CW electrically pumped operation of a laser whose volume was subwavelength but which was still larger than wavelength scale in at least one dimension. Room-temperature CW electrically pumped operation of a laser subwavelength in all three dimensions was finally demonstrated in 2013 by Ding[19] and colleagues, thanks in part to fabrication advances that reduced surface recombination and mode leakage to the substrate.

The achievement of room temperature operation indicates the promise of metal-clad nanolasers for on-chip photonic communication. However, room-temperature lasing is still difficult to reliably achieve, and the lasers that have been demonstrated so far suffer from high threshold currents, typically on the order of 1mA or more, along with low output powers. In addition to studying the novel physics enabled by small laser cavity

dimensions[4, 5, 6, 9], current metal-clad nanolaser research is focusing on identifying and addressing factors that limit nanolaser performance[8, 23, 24].

1.5 The work in this dissertation

This dissertation describes modeling-based investigations into the performance of wavelength-scale and sub-wavelength nanolasers. This work uses a combination of optical, electrical, and thermal simulation, which together illuminate the effects of nanolaser shape and material choice on performance. Chapter 2 describes the methods used in this dissertation for optical simulation of nanolasers, as well as for automating the systematic study of nanolaser cavity shape, and for processing the results of these simulations. Chapter 3 describes the methods used for study of nanolaser self-heating and heat conduction, and applies these to a study of the effect of shield thermal conductivity on nanolaser operating temperature. Chapter 4 applies the optical, thermal and electrical methods described in Chapter 2 and 3 to the analysis of a fabricated laser design, comparing the performance of the actually-fabricated laser with the idealized shape typically simulated in nanolaser studies. This analysis reveals that the main detriment to laser performance in this case was not nanolaser self-heating, as typically assumed, but the non-vertical gain and pedestal sidewalls. Chapter 5 investigates a technique for overcoming the effect of sidewall tilt on nanolaser performance: undercut etching, already used to reduce gain threshold in straight-walled nanolasers. Systematic analysis of nanolasers with a range of diameters, sidewall angles, and undercut amounts shows that a moderate 25% undercut etch reduces laser threshold gain to 100 cm^{-1} or less, regardless of gain or pedestal sidewall angles, enough to allow room-temperature lasing. Although the resulting narrower pedestals increase Ohmic heating in these lasers, study of nanolaser heating reveals that the additional heating is insignificant near the lasing threshold. Chapter 6 presents work toward making nanolasers that can deliver higher output power, by using a thermally-conductive shield to dissipate heat. In combination with the techniques described in Chapter 5 for lowering threshold current, the ability to effectively dissipate heat allows these lasers to operate at pump currents far above threshold. The optical simulations in this chapter determine the optimum shield thickness for the lowest threshold gain, for two commonly-used shield materials as well as for two materials with high thermal conductivity. Thermal simulations compare the thermal performance of nanolasers with these four shield materials at their optically-optimum thicknesses. Finally, Chapter 7

concludes the dissertation with a discussion of future work.

1.6 Acknowledgements

The material gain simulations in Fig. 1.2 were performed by Joseph S. T. Smalley.

This chapter, in part, is a reprint of material currently accepted for publication in Nanophotonics Journal, 2014. Qing Gu, Joseph S. T. Smalley, Janelle Shane, Olesya Bondarenko and Yeshaiahu Fainman. (2014) The dissertation author was an author of this review paper.

Chapter 2

Optical simulation

2.1 Introduction

Optical simulation is an important method of evaluating laser performance, used to determine the frequency of each cavity mode, as well as their losses and mode/gain overlap. For simple lasers and mode structures, these modal parameters can sometimes be determined by treating the cavity as a modified waveguide [21]. For a complex 3D cavity, such as a nanolaser with non-vertical sidewalls, a numerical treatment is usually necessary. This chapter details the 3D optical simulations used in this work, as well as a brief overview of the Matlab automation for simulating and analyzing sweeps of multiple geometry parameters.

2.2 Finite element analysis using COMSOL

2.2.1 Model construction

We use COMSOL 3.5a's RF electromagnetic waves finite element analysis module to solve for the nanolaser cavity modes. Although our lasers are designed with axial symmetry, we must use the full 3D analysis to find modes that vary azimuthally, or to evaluate the effects of asymmetries that occur during fabrication.

Fig. 2.1 shows a diagram of a typical metal-clad laser. We model the 3D shape of each nanolaser by approximating the laser's shape as a series of stacked cones with different sidewall angles. Most regions of the laser are approximated by single cones. Due to the effects of the wet undercut etching step, the bottom section of the lower

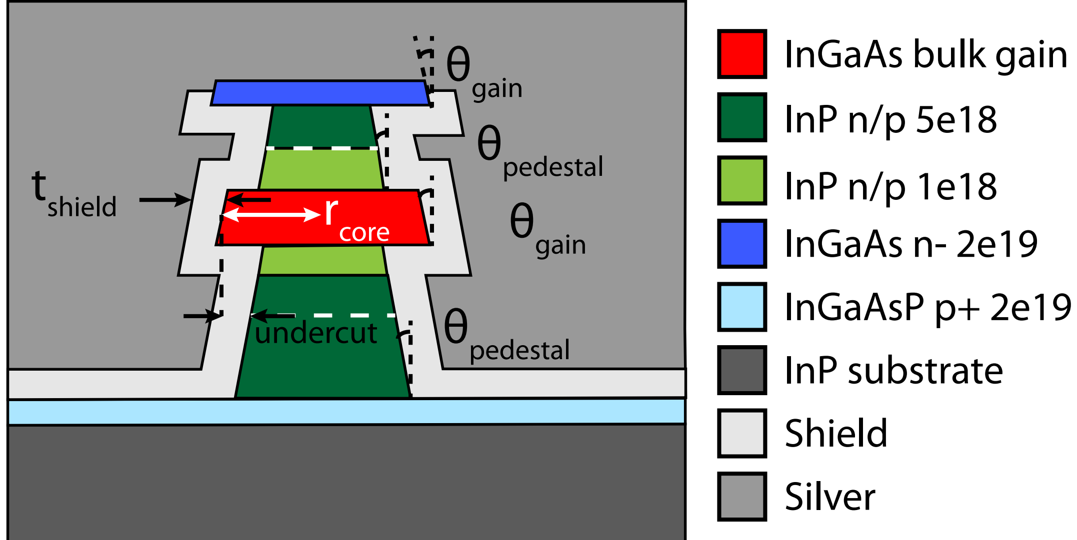

Figure 2.1: Diagram of an example nanolaser, consisting of stacked semiconductor layers on top of a thick InP substrate, covered in a dielectric shield material and surrounded by a metal cladding.

pedestal can have sidewall angles that vary with height, and so this layer is allowed to be comprised of arbitrarily many sublayers. We model the substrate below the nanolaser as well, since this is a major source of modal loss.

Surrounding the laser is a dielectric shield whose thickness is constant for a given laser design, but which may vary from experiment to experiment. The shield is formed through atomic layer deposition (ALD) or Plasma-Enhanced Chemical Vapor Deposition (PECVD) and conformally coats the structure. The shield layer therefore needs to be constructed so that its thickness is constant with respect to the surface normal, including the underside of any overhanging layers. For a shield with thickness t_{shield} , the diameter d_{shield} of the shield at the base of a layer with base diameter d_{layer} , sidewall angle θ and thickness h is

$$d_{shield} = d_{layer} + \frac{2t_{shield}}{\cos\theta}$$

For the shield covering a layer that is allowed to overhang adjacent layers, such as the gain region, the bottom of the shield region starts a distance t_{shield} below the layer, and the shield's diameter at this point is

$$d_{shield} = d_{layer} + 2t_{shield}\tan\theta + \frac{2t_{shield}}{\cos\theta}$$

Surrounding the shield layer is a metal cladding of thickness t_{metal}. Because the

skin depth of our wavelength in metal is only a few nanometers, the thickness of the metal cladding beyond a few nanometers does not affect the optical simulation. As a result, we let metal fill the rest of the simulation space beyond the shield, as shown in Fig. 2.1, allowing us to use a perfect electric conductor as a simple boundary to our simulation, at the outer edge of the metal. For the simulation boundaries at the edge of the substrate, lower contact, unetched lower pedestal (if applicable), and substrate shield, we use perfectly-matched layers to prevent light back-reflection.

2.2.2 Meshing the model

In finite element analysis, the simulation area is decomposed into many small subareas, called finite elements. The number of elements required to adequately simulate the model depends on how rapidly the local solution changes, which in turn depends on the wavelength of light in the material, and on the size of features in the structure. COMSOL refers to the grid of finite elements as the model mesh. Although COMSOL automatically adjusts the mesh fineness based on feature size, accounting for the wavelength in the material must be done manually. We set the maximum element size in each domain to be λ_0/n, where λ_0 is the free-space wavelength corresponding to our initial eigenvalue frequency guess, and n is the refractive index of the material in each domain. In addition, for the domains in which we expect the field to be changing quickly, we multiply this maximum element size by an additional fraction. For the gain region, this extra mesh factor is 1/9, while for the rest of the laser column and shield, this factor is 1/3.

2.2.3 Solving the model

We use COMSOL's PARDISO solver to search for eigenvalues around a given initial frequency guess, $\omega_{guess} = 2\pi c/\lambda_{0,guess}$, where $\lambda_{0,guess}$ is our initial guess of the free-space resonance wavelength. Typically we ask the solver to return 100 eigenvalues, since the solver returns not only the best-confined modes, but also many weakly-confined modes. This returns eigenvalues with free-space wavelengths within a 200-400nm range of our initial guess, depending on the size of the laser (larger lasers have more closely-spaced modes, so the range for a larger laser will be narrower). Depending on the gain bandwidth available at our chosen operating temperature and pump level, we may later discard the eigenvalues returned in part of this range.

From the real and imaginary components of each eigenvalue returned by the simulation, we can calculate key information about the cavity mode corresponding to this eigenvalue. The frequency of each eigenvalue λ can be calculated as $\omega_0 = |imag\{\lambda\}|$, while the cavity quality factor Q is calculated as $Q = \omega/(2 \cdot real\{\lambda\})$. We can also calculate the confinement factor Γ using $\Gamma = \iiint_{gain} W \cdot \partial V / \iiint_{everywhere} W \cdot \partial V$, where W is the total electric energy density. Similarly, we can calculate confinement factors for other regions, such as shield or metal, to determine overlap with these regions. Another important parameter is the threshold gain, which we calculate in this work as

$$g_{th} = \frac{\omega_0 n_{gain}}{c\Gamma Q}$$

For more accuracy, the group index of the mode should be used instead of n_{gain}; this change will make the largest difference for modes whose overlap with the dielectric shield is significant, making their group indexes significantly lower than n_{gain}.

2.3 Automation

In the course of the work reported in this dissertation, hundreds of nanolaser designs needed to be simulated, many according to parameter sweeps that affected multiple geometry aspects simultaneously. Matlab control was used to automate both the building of nanolaser models, the running of simulations, the ananlysis of eigenvalues, and the compilation of results. The following sections provide an overview of some aspects of this automation.

2.3.1 Assigning subdomains

When matching materials with simulation subdomains, COMSOL numbers the subdomains according to their spatial locations. As a result, depending on geometry parameters such as shield thickness and undercut amount, the same subdomains may be numbered in a different order for different laser designs. For Matlab automation of geometry sweeps, therefore, some method is needed to automatically determine which subdomain numbers correspond to which regions of the laser.

The method used in this work involves identifying subdomains based on the geometry objects (cones, prisms, etc) that each subdomain overlaps. In the case of our pedestal nanolasers with a fixed number of layers in the semiconductor stack, there is a limited number of possible configurations for the subdomain/geometry object overlaps,

so it is possible to enumerate them all. Each possible set of geometry object overlaps is listed in a table along with a group number indicating the corresponding laser material. Then, for every subdomain that COMSOL numbers, the table can be searched for a match to that combination of geometry object overlaps. A table with 25 entries was sufficient to cover all the laser geometries used in this dissertation.

This strategy requires the user to manually update the table of geometry object overlaps every time the number of layers in the semiconductor stack changes, including if new diameter control points are added. A more robust future strategy would be to identify subdomains based on their location.

2.3.2 Identifying boundaries

For the optical simulation, boundaries are numbered automatically by COMSOL, since all but the simulation outer boundaries are identical simple continuity boundaries. However, for the thermal simulations, the boundaries must all be individually identified, since some are heat sources or heat sinks. Because there were only a few possible boundary numbering orders among the thermal goemetries simulated in this dissertation, was even more limited for the thermal simulation than for the optical simulation, it was possible to use a simple switch statement to choose between these, based on, for example, whether the thickness of the shield was greater or less than that of the top layer of the lower pedestal. A location-based strategy of identifying boundaries would be a more robust way to handle a variety of future geometry changes.

2.3.3 Processing optical simulation results

When searching for enough eigenvalues to cover a large wavelength range, each simulated nanolaser design can yield hundreds of eigenmodes. Automation greatly aids in the processing of eigenmodes as well. For each solution returned by simulation, Matlab automation extracts the eigenvalue and calculates ω_0, λ_0, Q, g_{th}, and Γ, as well as the confinement factors for other regions such as substrate, shield, and metal. These results, along with the geometry control parameters, are stored in two text files, one in wavelength order and one sorted by threshold gain. In addition, images of the normalized electric field from side, top, and a 3D perspective view are exported. To verify correct subdomain assignment and material parameters, a side view of the refractive index is also exported.

2.3.4 Building input files for SILVACO simulation

The calculation of laser self-heating (as detailed in Chapter 3) requires the use of an additional simulation program, SILVACO's ATLAS. Although ATLAS does not have a Matlab interface, its inputs and outputs are in the form of text files that can be generated via Matlab. The same user inputs that were used to build the COMSOL simulations, therefore, were translated into the formatting of a SILVACO input file (with the addition of additional electrical material parameters). The generation of lists of SILVACO input files was automated in Matlab. The parsing of SILVACO output files was automated as well, and these results were fed into the heat source calculations of Matlab-controlled COMSOL.

Chapter 3

Thermal considerations in electrically-pumped metallo-dielectric subwavelength nanolasers

3.1 Introduction

Metal-clad subwavelength semiconductor lasers (here, referred to as MCSELs) have shown promise for chip-scale integration of compact, densely spaced laser sources, thanks to the high mode confinement provided by their metal cladding[22, 8]. Lasing has been demonstrated in devices that are smaller than their free-space emission wavelengths in all three dimensions[7, 20], opening new avenues of research on the physics particular to small laser cavities [25, 4, 6, 26]. Recently, room-temperature electrically-pumped lasing has been demonstrated in these devices [19], beginning the transition of MCSELs from the first proof-of-concept devices to optical sources suitable for large-scale integration.

As MCSEL performance and reliability continue to improve, and as novel geometries continue to be explored, it becomes increasingly important to consider multiple aspects of nanolaser design, rather than focusing on cavity electromagnetic properties. Other important aspects of nanolaser design include surface passivation to reduce non-radiative surface recombination [27, 28], reducing material damage during fabrication [29], and efficient use of available material gain [9].

In this manuscript, we focus on thermal considerations, including self-heating and heat dissipation. Despite their importance in limiting device performance, the thermal properties of MCSELs have received little attention to date. The ability to model the laser's operating temperature allows the evaluation of the impact of self-heating on laser performance, as well as the design of new lasers with improved thermal properties. We present here a simple thermal modelling analysis that takes into account multiple sources of self-heating, and apply this model to an example MCSEL. In Section 3.2, we give an overview of the thermal modelling strategy that will be discussed in this paper, and present the example MCSEL design to which we will be applying this model. In Section 3.3, we adapt thermal models from vertical cavity surface emitting lasers (VCSELs) to include additional self-heating sources resulting from non-radiative carrier recombination: surface recombination and Auger recombination. We apply this model to calculate the total self-heating in an example MCSEL. In Section 3.4, we discuss the modeling of heat transport and dissipation in a nanolaser cavity, and apply this model to calculate the operating temperature of the example MCSEL analyzed in the previous section. In Section 3.5, we discuss the limitations of this thermal analysis and future improvements that might be made to increase accuracy.

3.2 Thermal model overview

The thermal modelling strategy described in this paper is based on models used in VCSELs[30], with modification to include features specific to nanoscale lasers. In the first step, detailed in Section 3.3, we calculate the total self-heating power generated by the laser at a given operating current and operating temperature. These self-heating sources are located within the laser's semiconductor layers, as well as at the semiconductor junctions. In the second step, described in Section 3.4, we use finite element simulation to model the temperature distribution throughout the laser and surrounding substrate/cladding, for the self-heating sources calculated above. In our example, the temperature increases are moderate, so we calculate steady-state operating temperature given the self-heating sources and material thermal parameters at the laser's initial temperature. For a more complete analysis, necessary for a device where the temperature changes are very significant, this process should be performed iteratively, with the self-heating sources and operating temperature recalculated at each time step.

We apply this thermal analysis to the example MCSEL shown in Figure 3.1.

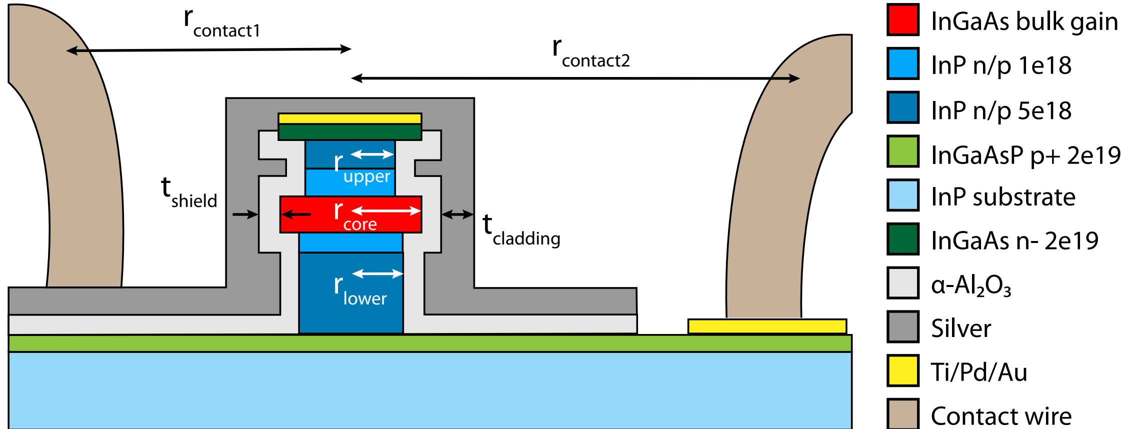

Figure 3.1: Diagram of electrically-pumped nanolaser to be analyzed. The laser has an InGaAs gain region of radius r_{core} surrounded by a lower InP plug of radius r_{lower} and upper InP plug of radius r_{upper}. The laser is surrounded by a dielectric shield of amorphous Al_2O_3 (α-Al_2O_3), of thickness t_{shield}, which is in turn surrounded by a metal cladding layer (silver) of thickness $t_{cladding}$. The metal cladding layer connects the laser's InGaAsP top contact layer to the top electrical contact wire, at a distance $r_{contact1}$ from the laser's center. The bottom contact InGaAsP layer is connected to the bottom electrical contact wire at a distance $r_{contact2} \gg r_{contact1}$.

The laser is based on the same epitaxially-grown wafer stack as used in previous work [7, 22]. The gain layer is InGaAs lattice-matched to InP, with radius r_{core}. The radii and thicknesses of the other layers comprising the InP pedestals and InGaAsP top and bottom contact layers are given in Table 3.1. This laser's upper and lower InP pedestals both have radii less than r_{core}, due to a two-step etching process that increases modal confinement to the gain layer by undercutting the pedestals[22]. The etching rate is different depending on layer composition and doping, so the upper plug radius r_{upper} is smaller than the lower plug radius r_{lower}. The layer radii are measured from SEM images of a fabricated structure, although the sidewalls have an idealized vertical shape.

The laser is surrounded by a dielectric shield of amorphous Al_2O_3 (α-Al_2O_3) of thickness $t_{shield} = 168$ nm, which is in turn surrounded by a metal cladding layer (silver) of thickness $t_{cladding} = 258$ nm around the gain region. In this laser design, the distance $r_{contact1}$ of the top contact wire from the center of the laser is 20 μm, while the bottom contact wire is a far enough distance $r_{contact2} \gg r_{contact1}$ from the laser's center that it does not play a role in heat dissipation.

Table 3.1: Dimensions and material parameters of MCSEL laser simulated in this paper. The layer compositions, doping, and thicknesses are those of the InP/InGaAs/InP double heterostructure grown on InP, used in previous work [7, 22]. The layer radii are for an example nanolaser geometry, based on the SEM-measured dimensions of an experimentally-fabricated nanolaser. Conductivities are calculated from the doping level and carrier mobility using Equation 3.3.

Layer	Material	doping	Thickness	Radius	Carrier mobility	Conductivity
Top contact	InGaAs, n-	2e19 cm^{-3}	125 nm	574 nm	2.5e3 $\left(\frac{cm^2}{V*s}\right)$ [31]	8.011e5 S/m
Upper pedestal top	InP, n	5e18 cm^{-3}	235 nm	358 nm	1.25e3 $\left(\frac{cm^2}{V*s}\right)$ [32]	1.001e5 S/m
Upper pedestal base	InP, n	1e18 cm^{-3}	235 nm	358 nm	2e3 $\left(\frac{cm^2}{V*s}\right)$ [32]	3.204e4 S/m
Gain	InGaAs bulk	-	300 nm	574 nm	-	-
Lower pedestal top	InP, p	1e18 cm^{-3}	125 nm	431 nm	80 $\left(\frac{cm^2}{V*s}\right)$ [32]	1.282e3 S/m
Lower pedestal base	InP, p	5e18 cm^{-3}	725 nm	431 nm	35 $\left(\frac{cm^2}{V*s}\right)$ [32]	2.803e3 S/m
Bottom contact	InGaAsP, p+	2e19 cm^{-3}	135 nm	N/A	50 $\left(\frac{cm^2}{V*s}\right)$ [31]	1.602e4 S/m

3.3 Self-heating sources

Our first step in determining the nanolaser's operating temperature is to determine the amount and location of the nanolaser's self-heating sources. Following the effective heat source model used for VCSELs[30], the major sources of self-heating are Joule heating, junction heating, and heterojunction heating, which are calculated as described below. To these self-heating sources we add heat generated by non-radiative recombination; namely, surface and Auger recombination heating. Surface recombination heating is important in lasers with nanoscale gain regions, and Auger recombination heating is important at high carrier concentrations. In this investigation, we assume ideal contacts; non-ideal contacts may contribute additional resistive and Schottky heating. These self-heating terms are dependent on operating current as well as on ambient temperature.

Most of the heat source calculations described below depend on the nanolaser's electronic behavior. To perform these electronic simulations, we use SILVACO's ATLAS, a 2D electronic device simulator that self-consistently solves the Poisson equation, the Schrödinger equation, and the carrier transport equation to calculate voltage, carrier density, and quasi-Fermi level separation. The results from these electronic simulations, for the nanolaser described in Figure 3.1 and Table 3.1, are shown in Figure 3.2.

3.3.1 Joule heating

Joule heating is self-heating due to the resistance of each of the semiconductor layers, and is given by

$$Q_J = I^2 R_s \tag{3.1}$$

where I is the operating current and R_s is the stack resistance of the semiconductor layer. The stack resistance of the ith layer may be calculated from the layer's radius r_i, thickness t_i, and conductivity σ_i using the standard formula for stack resistance[30],

$$R_i = \frac{t_i}{\sigma_i \pi (r_i)^2} \tag{3.2}$$

The material conductivity of the ith layer may be calculated using

$$\sigma_i = n_i \mu_i q_e \tag{3.3}$$

where n_i is the doping level, μ_i is the carrier mobility, and q_e is the electron charge.

The bottom contact layer behaves like a cylindrical thin film contact geometry. The resistance in this layer is given by[33]

$$R_{bc} = \frac{1}{2\pi\sigma_{bc}t_{bc}} \ln\left(\frac{r_{bc}}{r_{lp}}\right) + \frac{1}{4\sigma_{bc}r_{lp}} \bar{R}_c\left(\frac{r_{lp}}{t_{bc}}, \frac{\sigma_{bc}}{\sigma_{lp}}\right) \tag{3.4}$$

where the first term is the resistance of the bottom contact layer region between the nearest contact wire and the laser's lower pedestal, and the second term is the resistance of the bottom contact layer directly underneath the laser's lower pedestal. r_{lp} is the radius of the lower pedestal and r_{bc} is the distance between the laser's center and the nearest contact wire. For our laser, $r_{lp} = r_{lower}$ and $r_{bc} = r_{contact1}$ as drawn in Figure 3.1. σ_{bc} is the conductivity of the bottom contact layer, while σ_{lp} is the conductivity of the laser's lower pedestal. An empirical expression for $\bar{R}_c$ is numerically found to be[33]

$$\bar{R}_c\left(\frac{r_{lp}}{t_{bc}}, \frac{\sigma_{bc}}{\sigma_{lp}}\right) \cong \bar{R}_{c0}\left(\frac{r_{lp}}{t_{bc}}\right) + \frac{\Delta\left(\frac{r_{lp}}{t_{bc}}\right)}{2} \cdot \frac{2\sigma_{bc}}{\sigma_{bc} + \beta\left(\frac{r_{lp}}{t_{bc}}\right)\sigma_{lp}} \tag{3.5}$$

where $\bar{R}_{c0}\left(\frac{r_{lp}}{t_{bc}}\right)$ and $\Delta\left(\frac{r_{lp}}{t_{bc}}\right)$ are defined differently depending on the ratio $\frac{r_{lp}}{t_{bc}}$.

For $0.0011 \leq \frac{r_{lp}}{t_{bc}} \leq 1$ (lower pedestal radius is less than bottom contact thickness),

$$\bar{R}_{c0}\left(\frac{r_{lp}}{t_{bc}}\right) = 1 - 2.2968\left(\frac{r_{lp}}{t_{bc}}\right) + 4.9412\left(\frac{r_{lp}}{t_{bc}}\right)^2 - 6.1773\left(\frac{r_{lp}}{t_{bc}}\right)^3 \ldots + 3.811\left(\frac{r_{lp}}{t_{bc}}\right)^4 - 0.8836\left(\frac{r_{lp}}{t_{bc}}\right)^5$$

$$\Delta\left(\frac{r_{lp}}{t_{bc}}\right) = 0.0184\left(\frac{r_{lp}}{t_{bc}}\right)^2 + 0.0073\left(\frac{r_{lp}}{t_{bc}}\right) + 0.0808$$

while for $1 < \left(\frac{r_{lp}}{t_{bc}}\right) < 10$ (lower pedestal radius is larger than bottom contact thickness),

$$\bar{R}_{c0}\left(\frac{r_{lp}}{t_{bc}}\right) = 0.295 + 0.037\left(\frac{r_{lp}}{t_{bc}}\right)^{-1} + 0.0595\left(\frac{r_{lp}}{t_{bc}}\right)^{-2}$$

$$\Delta\left(\frac{r_{lp}}{t_{bc}}\right) = 0.0409x^4 - 0.1015x^3 + 0.265x^2 - 0.0405x + 0.1065$$

where $x = \ln\left(\frac{r_{lp}}{t_{bc}}\right)$.

For both cases,

$$\beta\left(\frac{r_{lp}}{t_{bc}}\right) = 0.0016\left(\frac{r_{lp}}{t_{bc}}\right)^2 + 0.0949\left(\frac{r_{lp}}{t_{bc}}\right) + 0.6983$$

For the laser whose geometry is listed in Table 3.1, $\frac{r_{lp}}{t_{bc}} = \frac{431}{135} = 3.2$, which yields $\bar{R}_{c0} = 0.312$, $\Delta = 0.333$, and $\beta = 0.715$, leading to $\bar{R}_c = 0.64$ using the expressions above. Therefore, the second term in Equation 3.5, the contribution to the bottom contact resistance by the region just below the laser pedestal, is 23 Ω. This is small compared to the first term of Equation 3.5, the contribution by the rest of the bottom contact, which is 282 Ω. Since in most nanolaser geometries $r_{bc} \gg r_{lp}$, the first term of Equation 3.5 will be much larger than the second term. In our thermal simulation in Section 3.4, we distribute the total resistance from both terms of Equation 3.5, 305 Ω, across the entire bottom contact layer. For greater accuracy, the resistive heating resulting from the second term can be modeled as located directly beneath the laser pedestal, while the resistive heating resulting from the first term can be distributed across the rest of the bottom contact.

The Joule heat sources for our example nanolaser are listed at the left of Figure 3.3, and contribute a total of 0.226 mW of heating power to the nanolaser. The largest source of Joule heating is the lower pedestal, followed by the bottom contact. The bottom contact is expected to contribute negligibly to laser heating, since the intensity of heat generated is low, and the heat can easily flow out of this region into the substrate and bottom contact wire. Similarly, the lower pedestal is adjacent to the bottom contact, which can easily remove heat from the laser pedestal. Compared to the other heating sources shown in Figure 3.3, Joule heating is a minor contribution to laser self-heating.

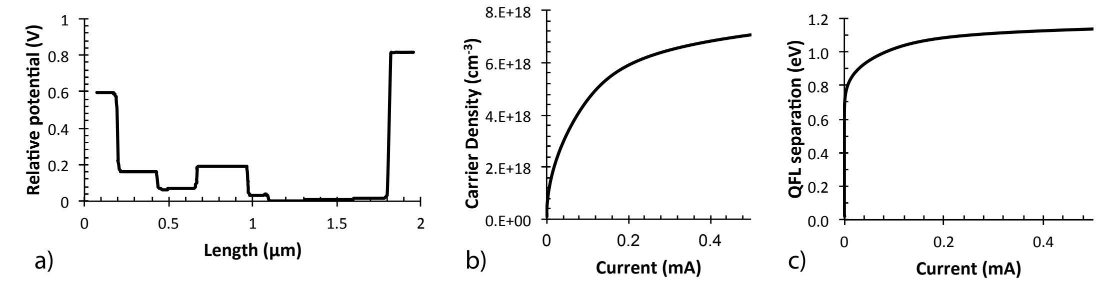

Figure 3.2: Result of electronic simulation. (a) Potential difference as a function of vertical distance from the top of the top contact. Length = 0 corresponds to the top of the top contact layer, and length = 1.88 μm corresponds to the bottom of the bottom contact layer. (b) Carrier density as a function of injection current. (c) Quasi Fermi level (QFL) separation as a function of injection current.

3.3.2 Junction heating

Junction heating is the heat generated by the voltage change at the junction between the undoped gain layer and the adjacent doped semiconductor layers. To calculate the voltage changes, the device's electrical behavior should be simulated; we use SILVACO's ATLAS to calculate voltage, carrier density, and quasi-Fermi level separation. Using the voltage change V_{jn} at the nth junction, the power dissipated will be $P_{jn} = I_{th}V_{jn}$, where I_{th} is the laser threshold operating current.

For the laser described in Figure 3.1 and Table 3.1, the device voltage, carrier density, and I-V curve are shown in Figure 3.2 (a), (b), and (c), respectively. The potential difference at each junction between differently-doped layers is visible in Figure 3.2 (a). For this example we use a threshold current of $I_{th} = 0.4$ mA and a slightly larger operating current of $I = 0.5$ mA, which were experimentally used for a fabricated nanolaser with dimensions similar to this example.

Figure 3.3 lists the calculated junction heating sources for this laser, located at junctions 3 and 4 (all other junctions in the laser contribute to heterojunction heating instead, as described in Section 3.3.3). Together these two junctions contribute 0.110 mW of self-heating.

3.3.3 Heterojunction heating

Similar to junction heating, heterojunction heating is the heat generated by the voltage change at the remaining junctions, between the doped semiconductor layers. As before, the power dissipated at the nth junction is $P_{jn} = IV_{jn}$. This time, the current

used is the operating current, rather than threshold current.

Figure 3.3 lists the calculated heterojunction heating sources for the laser described in Figure 3.1 and Table 3.1. Heterojunction heating adds 0.678 mW of self-heating to the laser. Most of this heating, however, takes place at the junction between the pedestals and the top or bottom contacts, and is easily dissipated via the contacts.

3.3.4 Surface recombination heating

Surface recombination is an additional heating term that is not usually considered for larger lasers, but becomes important for small lasers, for which the ratio of surface area to volume is large. The rate of surface recombination U_s in the gain region is given by

$$U_s = \frac{n}{\tau_s} \tag{3.6}$$

where n is carrier density (from the electronic simulation described in Section 3.3.2) and τ_s is carrier lifetime[7]. The carrier lifetime is given by

$$\frac{1}{\tau_s} = \frac{A_{active}}{V_{active}} \upsilon_s \tag{3.7}$$

where A_{active} and V_{active} are the area and volume of the gain region, and υ_s is the surface recombination velocity. To calculate υ_s at 300K for InGaAs, we use the value of υ_s at 77K, $\upsilon_s = 6.7 \times 10^3 cm/s$, along with the knowledge that the υ_s is proportional to the square root of temperature [7]. Thus, at 300K,

$$\upsilon_s(300K) = \upsilon_s(77K)\frac{\sqrt{300}}{\sqrt{77}} = 1.3 \times 10^4 cm/s \tag{3.8}$$

Using the above calculations to get the surface recombination rate U_s, we can then use our simulation of the quasi-Fermi level (QFL) from Figure 3.2(c) to calculate the heating power generated from surface recombination,

$$P_s = U_s \cdot V_{active} \cdot QFL \tag{3.9}$$

For our example nanolaser operating at T=300 K and at injection current I=0.5 mA, we calculate a QFL separation of 1.14 eV and a carrier concentration of 7.07e18 cm^{-3}. Using Equation 3.9, the surface recombination heating is calculated to be 0.393 mW.

3.3.5 Auger recombination heating

The last heating source we consider is Auger recombination [34] which, like the surface recombination heating, becomes a source of heat in the gain region. The Auger recombination rate U_A is given by

$$U_A = An^3 V_{active} \tag{3.10}$$

where n is the carrier density, V_{active} is the volume of the gain region, and A is the Auger coefficient. For InGaAs at 300K, the Auger coefficient is $9.8 \times 10^{-29} cm^6/s$ [34].

Using the carrier density for our example MCSEL at an injection current of 0.5 mA as calculated in Figure 3.2(b), we calculate the Auger recombination rate U_A to be $1.075 \times 10^{16} s^{-1}$. The Auger heating is then calculated as

$$P_A = U_A \cdot QFL$$

which yields 1.963 mW. This is by far the largest source of self-heating for the nanolaser, and because this heat source is located in the middle of the semiconductor stack, will also be the most difficult to dissipate.

In Figure 3.3 we summarize the self-heating sources for the example MCSEL and show their locations in the semiconductor stack. The junction and heterojunction heating sources are implemented as area heating sources located at the interfaces between layers, while Joule, surface recombination, and Auger recombination heating are volume heating sources implemented as distributed within each semiconductor layer. Only half of the device cross-section is shown since the device is approximated to be axially symmetric.

Note that each of these heat sources is dependent on operating temperature and on injection current. For the most accurate reflection of nanolaser temperature behavior, these heat sources should be updated to reflect the changing temperature as the nanolaser self-heats.

3.4 Heat dissipation

Once the sources of laser self-heating are known, the next step toward calculating laser operating temperature is to model the heat transport and dissipation in the laser. Heat transport heavily depends on the thermal parameters of the laser's constituent

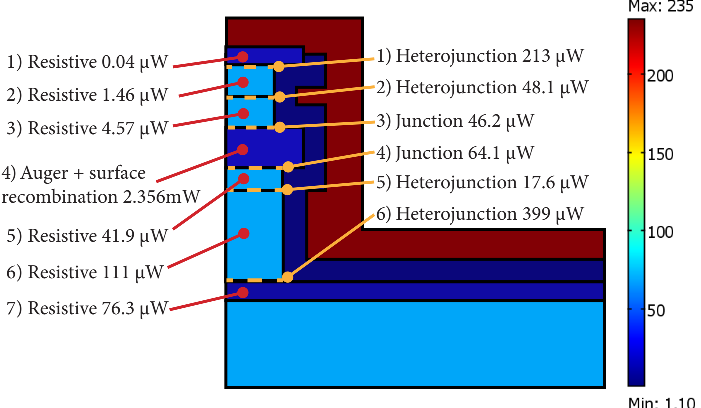

Figure 3.3: Amount and location of heating sources in the example MCSEL laser, at 300K ambient temperature and 0.5mA operating current. Each region is colored according to its thermal conductivity at 300K.

Table 3.2: Material thermal parameters used in heat transport simulations of the example MCSEL. All values are reported for T=300K.

	$\alpha - Al_2O_3$ (ALD)	SiO_2 (PECVD)	InP	$In_xGa_{1-x}As$ x=0.53	$In_xGa_{1-x}As_yP_{1-y}$ x=0.773, y=0.493	Ag
Thermal conductivity k $(W \cdot m^{-1} \cdot K^{-1})$	1.7-20 [35, 36, 37]	1.1 [38]	68 [32]	16 [39]	11 [31]	429 [40]
Heat capacity Cp $(J \cdot kg^{-1} \cdot K^{-1})$	880 [37]	725 [41]	310 [32]	320 [31]	320 [31]	235 [42]
Density ρ $(kg \cdot m^{-3})$	3690 [37]	2200 [43]	4810 [32]	5500 [31]	5120 [31]	10490 [42]

materials; thermal parameters for the materials used in the example MCSEL nanolaser, as well as a few other common nanolaser materials, are tabulated in Table 3.2. The values reported for amorphous aluminum oxide ($\alpha - Al_2O_3$) are for material deposited via atomic layer deposition (ALD). The range of thermal conductivities represents the range of values found in the literature[35, 36, 37] for $\alpha - Al_2O_3$. For all these materials, the thermal (and optical) parameters depend on the deposition conditions, so for the best accuracy, they should be measured for each new deposition recipe.

In addition to the heat sources and thermal parameters, another important factor affecting laser operating temperature are the device's heat dissipation capabilities. Depending on the experimental setup, heat may be dissipated through the sample's substrate into a heat sink (with the quality of heat transfer dependent on the thermal contact between substrate and heat sink) or through the electrical contact wires, or to

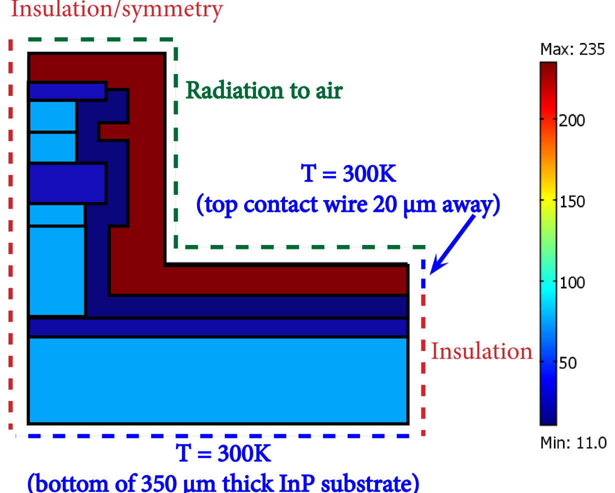

Figure 3.4: Boundary conditions used in heat transport simulation. The laser is simulated as a 2D axially-symmetric structure; the left edge is the axis of symmetry. The top surface of the metal cladding is surrounded by air, and is allowed to dissipate heat to ambient through radiation. The InP substrate is 350 μm thick (full thickness included in the model but not shown here), the bottom of which is set to a constant temperature of 300 K. This represents a perfect heat sink at the substrate bottom. Another perfect heat sink is located at the far right edge of the metal cladding, 20 μm away (again, full distance included in the model but not shown here); this represents heat conduction through the top contact wire. The rest of the simulation's right edge is set to insulation, since the right edge of the substrate is much farther away than the top contact wire and, because this surface faces air, is assumed to contribute negligibly to heat dissipation.

the surrounding air via radiation or convection. In our simulation we allow for both these situations, with the contact wires and substrate bottom approximated as perfect heat sinks. Figure 3.4 shows the boundary conditions for our thermal simulation, which define the locations and mechanisms of heat dissipation.

We model the heat transport in this MCSEL nanolaser using COMSOL's 2D axial-symmetric steady-state heat conduction model. In our case, we directly model the steady-state laser operating temperature, assuming that the temperature rise will be moderate and the temperature dependences of the heat sources and thermal parameters are relatively small. For the most accurate simulation, especially in the case where temperature change and/or temperature dependence is large, the temperature should be iteratively solved and the heating sources and material parameters adjusted at each time step. The results of our steady-state simulation are found in Figure 3.5, with temperature represented as color, and heat flux magnitude and direction represented by arrows.

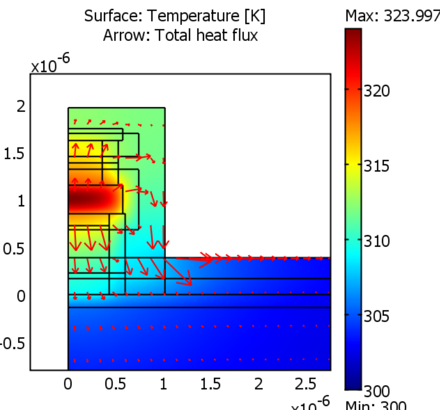

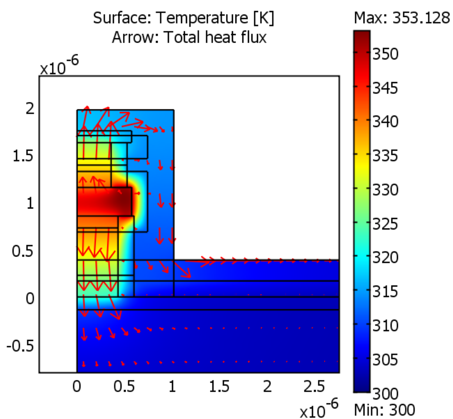

Figure 3.5: Calculated steady-state operating temperature of the MCSEL at 0.5 mA injection current and 300 K ambient temperature. Arrows represent the direction of heat flux, with the length of the arrow representing the amount of heat flux. Here, the dielectric shield is (a) $\alpha - Al_2O_3$ with thermal conductivity of k = 20 $W \cdot m^{-2} \cdot K^{-1}$, the highest literature value reported, or (b) SiO_2 with thermal conductivity of k = 1.1 $W \cdot m^{-2} \cdot K^{-1}$, also comparable to the lowest literature value reported for ALD $\alpha - Al_2O_3$ (Table 3.2).

From these results, we see that the mechanism of heat dissipation depends strongly on the dielectric shield's thermal conductivity. For higher-conductivity shields (Figure 3.5 (a)), the laser can dissipate heat through the shield layer, while for lower-conductivity shields (Figure 3.5 (b)), the primary method of laser heat transfer is through the InP upper and lower pedestals. By setting each boundary in turn to insulation, we determined that once the heat leaves the laser cavity, the most significant avenue for heat dissipation is conduction through the metal shield. In the higher-conductivity case, the laser's steady-state operating temperature is a maximum of 324 K, which occurs in the center of the gain region. In the lower-conductivity case, the laser heats to a maximum of 353 K, with the heat less able to escape from the edges of the gain region.

3.5 Discussion

Simulation of nanolaser operating temperature is important in the diagnosis of laser thermal problems, as well as in identifying design changes that may improve nanolaser thermal performance. Here, we demonstrated an example thermal model by calculating the magnitudes and locations of self-heating sources in a nanolaser, and simulating heat transport. We recognize that further improvements in the accuracy of

MCSEL thermal models will increase their usefulness, as well as reveal the nanolasers' temperature-dependent dynamics.

One significant improvement could be made by incorporating thermal feedback. For example, this basic model assumed a relatively modest temperature rise that does not significantly affect the laser's carrier density or material parameters. In the future, a self-consistent solution including the interdependences of self-heating sources and thermal parameters on laser's operating temperature, such as in VCSELs [29], will more fully reflect the true operating temperature and temperature-dependent dynamics.

The thermal parameters of nanolaser materials vary not only with temperature, but also with fabrication recipe. For the most experimentally-relevant models, these thermal parameters should be experimentally measured for each fabrication recipe. This measurement can be performed with the 3ω method[44] , which has been adapted to measure thermal conductivity in solids [44] and thin films [45, 46], as well as across junctions [47]. Another alternative is scanning thermal microscopy, which has been used to measure thermal conductivities and probe the local temperatures of nanoscale structures [48, 49]. When combined with high-sensitivity bi-material cantilevers, very high spatial and thermal resolution may be achieved [48, 50]. Such high-resolution measurements may provide experimental validation of nanolaser thermal models.

In addition, the use of nanoscale heat transport models, rather than macroscale, should be investigated for these nanolasers. Although the few MCSEL thermal studies that exist have used macroscale heat transfer[**?**], the dimensions of these nanolasers are comparable to the phonon mean free paths in many of their constituent materials, putting them in the nanoscale heat transfer regime[51]. We are currently expanding our model to include nanoscale heat transport, including an analysis of the circumstances under which the difference between macroscale and nanoscale heat transport become significant.

3.6 Acknowledgements

The authors would like to thank Dr. Boris Slutsky and Mr. Dor Gabay for helpful discussions. This work was supported by the Defense Advanced Research Projects Agency (DARPA), the National Science Foundation (NSF) through the Center for Integrated Access Networks (CIAN) NSF ERC under grant #EEC−0812072, the Cymer Corporation, the Office of Naval Research MURI program, and the U.S. Army Research Office. This work was also partly supported by the Brazilian financial agencies: FAPESP,

CNPQ, CAPES and done within the National Institute for Science and Technology (FOTONICOM) and the Center for Optics and Photonics (CePOF).

This chapter, in full, is an adaptation of the material appearing in The Proceedings of SPIE, 2014. Janelle Shane, Qing Gu, Felipe Vallini, Brett Wingad, Joseph S. T. Smalley, Newton C. Frateschi, and Yeshaiahu Fainman. (2014). The dissertation author was the primary investigator and author of this paper, and performed all the optical and thermal simulations and analysis in this chapter. Felipe Vallini performed the SILVACO simulations in Fig. 3.2.

Chapter 4

Amorphous Al_2O_3 shield for thermal management in electrically pumped metallo-dielectric nanolasers

4.1 Abstract

We analyze amorphous Al_2O_3 (α-Al_2O_3) for use as a thick thermally conductive shield in metallo-dielectric semiconductor nanolasers, and show that the use of α-Al_2O_3 allows a laser to efficiently dissipate heat through its shield. This new mechanism for thermal management leads to a significantly lower operating temperature within the laser, compared with lasers with less thermally conductive shields, such as SiO_2. We implement the shield in a continuous wave electrically pumped cavity, and analyze its experimental performance by jointly investigating its optical, electrical, thermal, and material gain properties. Our analysis shows that the primary obstacle to room temperature lasing was the device's high threshold gain. At the high pump levels required to achieve the gain threshold, particularly at room temperature, the gain spectrum broadened and shifted, leading to detrimental mode competition. Further simulations predict that an increase in the pedestal undercut depth should enable room temperature lasing in a device with the same footprint and gain volume. Through the integrated treatment of various physical effects, this analysis shows the promise of α-Al_2O_3 for nanolaser thermal management, and enables better understanding of nanolaser behavior, as well as more informed design of reliable nanolasers.

4.2 Introduction

During the last decade, numerous wavelength and subwavelength scale semiconductor lasers have been demonstrated, including dielectric nano-discs [11], photonic crystal lasers [17], nano-bowties [52], nano-wires/rods [14, 15], nano-membranes [16], and metal-clad cavities [7, 20, 28]. While all these devices enable fundamental studies of various nanoscale phenomena [6, 4, 26], the design of nanolasers to date has focused almost exclusively on the optical mode, i.e. pure electromagnetic consideration, with other design aspects ignored. In particular, while thermal dynamics in vertical-cavity surface-emitting lasers (VCSELs) has been studied in depth [29, 30], it has been overlooked in nanolasers. Liu et al. [**?**] did consider the device temperature of CW optically pumped microdisk lasers with an ambient temperature of 45K, but only to the extent of observing the steady-state temperature's dependence on the semiconductor pillar pedestal width, in a stand-alone heat conduction model.

While designing and demonstrating new cavity geometries with novel optical mode configurations continue to be of great interest, other physical phenomena and design aspects, including electrical, thermal and temperature dependent material properties, are also important. They can play crucial roles, especially in developing stable and reliable devices operating in the electrically pumped CW mode at room temperature, which is necessary for practical insertion of nanolasers into densely integrated chip-scale photonic circuits. By combining optical and electrical simulations with laser rate equations, Vallini et al. [24] compared multiple quantum well (MQW) and bulk gain media in metallo-dielectric semiconductor nanolasers. This work revealed that the choice of gain medium for nanolasers is non-trivial, and highlighted the importance of design considerations other than the cavity's electromagnetic properties.

Metal-clad nanolasers are excellent candidates for the optical source in chip-scale integrated circuits because of the elimination of optical interference between adjacent devices, and the first demonstration of room temperature lasing behavior further advanced this type of nanolaser from proof-of-concept demonstrations to a technologically relevant light source [19]. Although the rotational symmetric emission from the subwavelength aperture of these nanolasers poses difficulties in coupling the emitted light into integrated waveguides, it has been proposed that efficient out-coupling into an integrated Si waveguide positioned at the bottom of the nanolaser structure can be achieved [53]. This method relies on breaking the symmetry of the transverse electric (TE) mode of the

cavity, and can be realized in a hybrid III-V/Si platform [3].

In metal-clad nanolasers, metal losses may be minimized using a metallo-dielectric composite structure, in which a shield layer is placed between the active region and the metal cladding[21]. In the case of electrical injection, the dielectric shield also serves as the electrical insulation layer and the passivation layer. From a purely electromagnetic perspective, the optimal shield thickness, corresponding to minimal threshold gain of a cavity mode, can be determined numerically [21], and may be approximated analytically [54]. However, the shield's effects on electrical and thermal properties are often ignored. The choice of shield material and thickness can strongly affect the cavity's ability to dissipate heat, and the resulting temperature-dependent changes in the material gain spectrum [9] may strongly affect the laser's performance. In some cases, the shield's effect on thermal management may limit the practical shield thickness, preventing devices with the optimal shield thickness for the optical mode from lasing [28].

Two types of dielectric materials, namely silicon dioxide (SiO_2) and silicon nitride (SiN_x), have been used in metallo-dielectric nanolasers. For SPP mode operation, the dielectric layer is on the order of 20nm to provide electrical insulation; SiN_x is used because of its effectiveness as a passivation layer [7, 55]. For photonic mode operation, the optimal shield thickness is much greater than 100nm for minimal threshold gain, from the electromagnetic point of view [28, 21]; SiO_2 is preferred because of its lower refractive index than SiN_x and therefore better mode confinement [56].

From the thermal management perspective, however, both SiO_2 and SiN_x are not the best candidates because of their poor thermal conductivities. To this end, sapphire (crystalline Al_2O_3) would be ideal as a low refractive index, thermally conductive dielectric layer. Indeed, sapphire is chosen over air as the membrane or substrate material in sapphire-bonded photonic crystal lasers, because of its ability to conduct heat better than air [57]. Sapphire is also a common substrate material for nanowire lasers, owing to its epitaxial compatibility (matching Wurtzite crystal structures) with semiconductor nanowires, as well as its optical transparency over a wide range of wavelengths [58, 59]. However, thin film deposition techniques, which are required to create shield layers on nanolasers, yield α-Al_2O_3, rather than the crystalline sapphire form. α-Al_2O_3 has a lower thermal conductivity than its crystalline counterpart, but, depending on the deposition conditions, can be a significantly better thermal conductor than SiO_2 or SiN_x. The thermal properties of SiO_2 [60] and Si_3N_4 [61] deposited via plasma-enhanced chemical vapor

Table 4.1: Optical and thermal properties of materials used in numerical modeling, at 1550nm and 300K

Material	Permittivity ε	Thermal conductivity T_c ($W \cdot m^{-1} \cdot K^{-1}$)
α-Al_2O_3	2.69	1.7-20
SiO_2	2.1	1.1
Si_3N_4	4.49	0.7
InP	6.96	68
$In_xGa_{1-x}As$ (x=0.53)	11.56	16
$In_xGa_{1-x}As_{1-y}P_{1-y}$ (x=0.773,y-0.493)	11.83	11
Ag	-130.6-j3.33	429

deposition, and α-Al_2O_3 deposited via atomic layer deposition (ALD) [35, 36, 37] are listed in Table 4.1.

α-Al_2O_3 created by wafer fusion has been explored as a thermally conductive membrane layer in photonic crystal microlasers, but its thermal advantages for metallo-dielectric nanolasers have not been explored so far. Although ALD deposited α-Al_2O_3 with thickness typically less than 20nm has been used in nanolasers, its role was strictly for electrical insulation or passivation, which utilizes its surface smoothness [62, 63]. It was mentioned in [64] that Al_2O_3 or diamond can potentially replace SiO_2 as the low-index membrane in silicon nano-membrane reflector VCSELs, such that improved thermal conductivity and power dissipation handling can be achieved, but so far this discussion has not been followed by experimental implementation.

α-Al_2O_3 also shows promise because of its surface smoothness when deposited via ALD. The breakdown voltage and leakage current of a device are directly related to the number of surface states, and in turn, surface roughness. Although SiN_x is traditionally used as the passivation layer [55], high-k dielectrics deposited by ALD have shown advantages over SiN_x for MOSFETS and solar cells by having atomic layer smoothness [65, 66]. In nanoscale devices, as the surface to volume ratio becomes significant, ALD deposited α-Al_2O_3 becomes an especially good candidate.

In this manuscript, we present, to the best of our knowledge, the first analysis of a combination of the nanolaser's physical phenomena such as optical, electrical and thermal performance, and show the interplay of various design parameters. We show how

resistive heating of the device due to CW electrical pumping, as well as non-radiative recombination induced heating in the gain region, can lead to a temperature in the semiconductor that is higher than the ambient temperature. Additionally, we consider the effect of the resulting temperature increase on the threshold gain of the lasing mode, and on the available material gain. We also report the first experimental implementation of α-Al_2O_3 as a thick thermally-conductive shield in metallo-dielectric nanolasers, exploring α-Al_2O_3's superior thermal properties over other dielectric shield candidates. We characterize a device with a cavity volume of $0.86\lambda^3$ (λ=1515nm), operating under CW electrical pumping at 77 K, and observed linewidth narrowing to 2nm, along with increasing mode competition at higher pump levels. Joint optical, electrical and thermal simulations reveal that the unsatisfactory performance is a result of poor optical mode confinement rather than self-heating. Our simulations also reveal the promise of α-Al_2O_3 shields as a method to improve thermal performance, crucial to the design of reliable electrically pumped nanolasers for dense chip-scale integration applications.

In Section II, we provide details of device fabrication and characterization, with emphasis on the formation and the subsequent etching of the α-Al_2O_3 shield. In Section III, we detail the optical simulation of the fabricated device, and show that significantly different mode behavior is predicted for the realistic device geometry and the approximate device geometries that are typically simulated. In Section IV, we present the electrical, thermal, and material gain analysis of the fabricated device. In Section V, we predict that, while keeping the device footprint unchanged, a slight modification of the cavity design should enable room temperature lasing in these lasers. This new design is based on a 2-step InP selective etching process calibrated specifically for our material system and device dimension (the process is detailed in Section II), and the numerical modeling of realistic structures. Lastly, in Section VI, we discuss the limitations of the current numerical approach, and of current fabrication methods, and conclude with an outlook toward further improvements in nanolaser thermal performance.

4.3 Device fabrication and characterization

The platform for our devices is an InP/InGaAs/InP double heterostructure grown on InP, used in [7, 22, 67]. The schematic of the device is depicted in Fig. 3.1. The gain medium is the intrinsic bulk $In_{0.53}Ga_{0.47}As$ layer of 300nm thickness. The upper and lower doped InP layers, as well as the highly doped top InGaAs and bottom InGaAsP

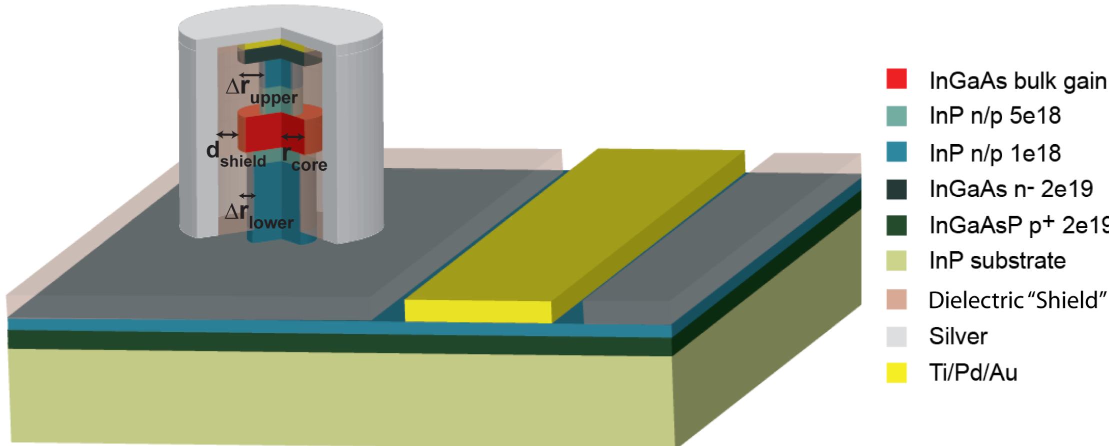

Figure 4.1: A schematic of the electrically pumped nanolaser with α-Al2O3 shield and InP pedestals, where rcore is the radius of InGaAs gain layer, Δrupper and Δrlower are the undercut depths of the upper and lower InP pedestals, respectively. dshield is the thickness of α-Al2O3 shield layer.

layers, serve as electrical channels through which the injected carriers flow into the active region. Efficient lateral mode confinement is achieved by incorporating a dielectric shield layer between the metal cladding and the gain core [21]. In the vertical direction, the index contrast between $In_{0.53}Ga_{0.47}As$ and doped InP layers provides mode confinement. To further increase the vertical confinement without increasing the total height of the device, we undercut the doped InP layers using the two-step wet etching process described below.

For fabrication, the initial circular masks for the pillars are created by e-beam lithography with hydrogen silsesquioxane (HSQ) negative resist. Reactive ion etch (RIE) is then used to form cylindrical pillar structures of ~1.5μm height, as shown in Fig. 4.2(a). Subsequently, we wet etch the doped InP layers, without affecting the InGaAs gain layer, to create InP pedestals, employing a two-step selective etching process. In the first step of the selective etching, the $HCl{:}H_3PO_4$ (1:4) etchant combination is used. Due to the $HCl{:}H_3PO_4$ combination's anisotropic etching, the etch rate is slowest in the (111) plane, resulting in cone shaped regions (Fig. 4.2(b)), similar to those obtained in Lee et al. [22]. In the second step, the $HCl{:}CH_3COOH$ (1:4) combination is used, whose anisotropic etch rate in the (111) plane also produces cone shaped regions, but in the opposite direction of that from the $HCl{:}H_3PO_4$ etchant combination, if used alone (Fig. 4.2(c)). Therefore, applying the two chemistries sequentially with the proper ratio of

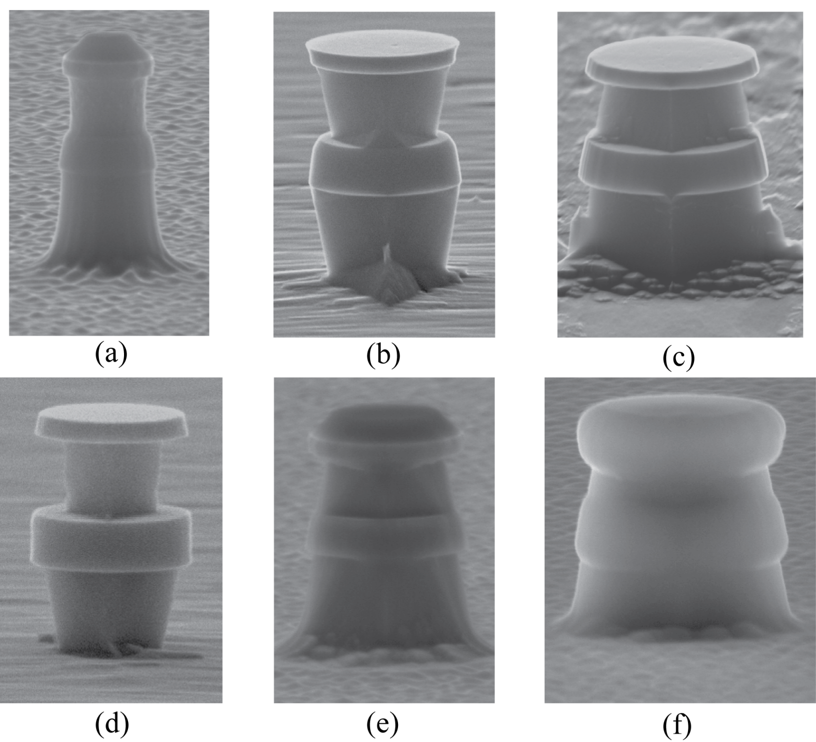

Figure 4.2: SEM images of pedestal pillar lasers (a) after RIE, (b) after HCl:H_3PO_4 etching alone, (c) after HCl:CH_3COOH etching alone, (d) after the 2-step selective etching. (e) Fabricated device after the 2-step selective etching. (f) Fabricated device after α-Al_2O_3 deposition

etching times, vertical pedestal sidewalls can be obtained, (Fig. 4.2(d)). Because the etching rate varies for different dopant types and concentrations, the upper InP layer is always narrower than the lower InP layer. Fig. 4.2(e) shows the InP pedestals after the two-step etching. For the measured device in Fig. 4.2(e), only a slight selective etching (5 seconds in HCl:H_3PO_4 (1:4), followed by 2 seconds in HCl:CH_3COOH:H2O (1:4:35)) is employed.

After removing the HSQ mask following the InP etching, α-Al_2O_3 is conformally coated around the semiconductor pillar using thermal ALD (Beneq TFS 200 system). The growth temperature is set at 250C. Trimethylaluminum $Al(CH_3)_3$ (TMA) precursor is used as the Al source, and H_2O is used as the oxygen source. One layer of α-Al_2O_3 is grown by 45ms of TMA exposure, 850ms of N_2 purge, 50ms of H_2O exposure, and 850ms of N_2 purge, and the procedure is repeated until the desired thickness is reached. The purpose of the N_2 purge is to minimize the parasitic chemical vapor deposition during the growth. The film thickness is then measured, using both ellipsometry and SEM (Fig. 4.2(f)). To access the n- InGaAs contact layer in preparation for n−type electrode deposition, the α-Al_2O_3 region on top of the pillar structure is removed through photoresist planarization and etching of α-Al_2O_3. Although the CHF3:Cl2 chemistry is usually used in Al_2O_3 etching, we avoid the use of Cl_2 due to its reactivity with III−V semiconductors. Instead, we use CHF_3:Ar (50:10sccm) plasma at 40mTorr and 150W RF power in a RIE chamber, resulting in an etch rate of ~8nm/min. Electrodes (Ti/Pd/Au) and cavity metal (Ag) are formed through multiple photolithography steps, metal deposition or sputtering, lift−off and annealing processes, similar to those described in [22].

For measurement, the device is forward biased by a DC voltage source, and CW emission through the substrate is collected through a 20x objective lens into a monochrometer with a maximum spectral resolution of 0.35nm. We characterize the device (SEM images of which are shown in Fig. 4.2(e) and (f)) of $r_{core} \approx$ 575nm, d_{shield} $\approx$ 170nm, $\Delta r_{upper} \approx$ 90nm and $\Delta r_{lower} \approx$ 20nm. We note that the shield thickness and InP undercut depth are not optimized for the device. Fig. 4.3(a)−(c) depict the device's behavior at an ambient temperature of 77K. The side-view schematic of the fabricated device is shown in the inset of Fig. 4.3(a), where different regions are represented by their respective refractive indexes. Fig. 4.3(a) shows the measured emission spectra, from a broadband electroluminescence (EL) at low injection currents, to an emission peak with 2nm linewidth at 1515nm at high injection currents.

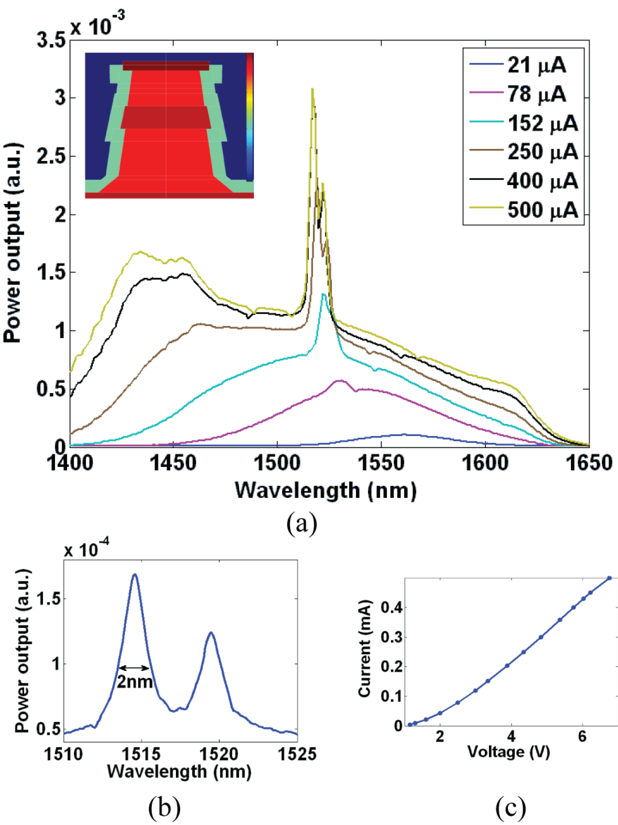

Figure 4.3: Measured device performance at an ambient temperature of 77K. (a) Spectral evolution with increasing injection current. Inset: side-view of the fabricated device schematic. (b) Linewidth measurement by a monochrometer with 0.35nm resolution, at an injection current of 0.4mA. c) I—V curve at 77K.

The peak at 1515nm is one of two degenerate whispering gallery modes (WGM), as shown in Fig. 4.3(b). At higher pump levels, as depicted in Fig. 4.3(a), a broad peak appears at shorter wavelengths than the main peak, due to the existence of an additional cavity mode at 1423nm (see Table 2). This cavity mode begins to compete with the 1515nm mode, with the help of a broadened and blue-shifted material gain spectrum at high pump levels (shown in Fig. 8). When the injection current is increased beyond 450µA, the 1515nm mode shows negligible further linewidth narrowing or increase in amplitude, and the mode at 1423nm continues to increase in amplitude. While lasing threshold might not have been reached for the 1515nm mode, for our analysis in the following sections we approximate the threshold current to be the current level beyond which this mode linewidth stops significantly narrowing, ~400µA in this case [68]. The linewidth under this condition is depicted in Fig. 4.3(b). In Fig. 4.3(c), we plot the measured current–voltage (I–V) curve at 77 K.

4.4 Device analysis - optical

We perform 3D simulation of the fabricated device at 77K using commercial finite element software (COMSOL Multiphysics). The cavity resonance wavelength depends on temperature to the extent that the complex relative permittivity $\varepsilon=\varepsilon'+j\cdot\varepsilon''$, of the metal and semiconductor depend on temperature. Specifically, the resonant wavelength depends on the real part of the permittivity, whereas the imaginary part determines gain or loss. We use silver permittivity values at 1550nm from [9], $\varepsilon(Ag,77K)=-132.5-j0.5$, which is calculated via a temperature dependent Drude model [69, 70] and scaled to match the empirical data of Johnson and Christy [71]; at room temperature, $\varepsilon(Ag,300K)=-130-j4.2$. The imaginary part of silver's permittivity is strongly dependent on temperature: it changes by nearly an order of magnitude, while the real part changes only by 2%. The real permittivities of semiconductors are only weakly dependent on temperature. Therefore, the effect of temperature on the cavity resonance wavelength is small [9]. Due to the lack of empirical thermo-optic data at temperatures other than 300K for the various semiconductor compositions in our cavity, we assume constant permittivity values with respect to temperature. Given that the thermo-optic coefficients are generally on the order of 10^{-4} [72, 73], this assumption has a minor effect on the resulting locations of the cavity resonances.

Table 4.2 lists the simulated optical mode behavior of the two experimentally

Table 4.2: Simulated optical mode characteristics at 77K of experimentally observed competing modes

λ_{cav} (nm)	g_{th} (cm^{-1})	Q	Γ	Degeneracy
1423	8415	67	0.268	Yes
1515	10622	51	0.259	Yes

observed competing modes in terms of resonant wavelength λ_{cav}, cavity Q-factor, mode confinement factor Γ, and threshold gain $g_{th} = 2\pi n_g / (\lambda Q \Gamma)$ where n_g is the group refractive index. At 77K, two degenerate WGM modes, with azimuthal mode number M=5, reside at around 1515nm, in agreement with the two narrow emission peaks observed at the same wavelengths (Fig. 4.3(b)). Even though the degenerate modes at 1423nm have similar g_{th}, the magnitude of the material gain at those wavelengths is less than that at 1515nm at low to moderate pump levels. At higher pump levels, as well as at higher ambient temperature, these modes compete, limiting laser performance; the effects of gain broadening and shift will be discussed more fully in Section V.

Even though self-heating is sometimes believed to be the most detrimental effect in nanolaser performance at high temperatures and/or under CW pumping [74], as we will show in the next section, this is not the case in our fabricated device. Instead, the most detrimental effect to the operation of our device is the angled gain sidewalls and the negligibly undercut lower InP pedestal, causing high radiation loss and poor mode confinement, and thus high threshold gain. In order to reach such high gain values in the material, both cryogenic temperature operation and a high carrier density are necessary. We note that these detrimental effects are only evident under detailed optical simulations that take sidewall angles into account, as well as the differing amounts of undercut in the upper and lower InP pedestals (Table 4.3). These are not typically simulated, yet are common experimental occurrences. For example, the gain sidewalls formed by RIE are not always vertical [22], although the fabrication process can be calibrated to minimize the deviation from a vertical sidewall [28]. The upper and lower InP pedestals are frequently cone shaped, due to anisotropic properties of the etchants, as detailed in Section II. Even though sidewalls that are more vertical than those in [22] can be obtained using the two-step InP selective etching process, there is usually at least some sidewall angle. Furthermore, due to the material-selectivity of the etchants, the InP layers with different doping types and concentrations inevitably have different undercut depths.

Table 4.3: Optical mode simulation of the lasing cavity mode of the as-fabricated as well as three increasingly idealized structures, at 77K

	As-fabricated	Realistic undercut; vertical gain sidewalls	All sidewalls vertical; realistic undercut ratio	All sidewalls vertical; 1:1 undercut ratio
Q	51	53	768	2445
g_{th} (cm^{-1})	10,622	9,809	373	103
λ_{cav} (nm)	1515	1512	1506	1504
Γ	0.259	0.270	0.495	0.562

To show the effects of the abovementioned differences between the fabricated and typically simulated structures, we construct the model of the lasing device with the exact geometric parameters measured from SEM images during various fabrication steps. We additionally model three increasingly idealized structures with the same device footprint and gain volume (Table 4.3, second to fourth rows) as the experimentally realized one (Table 4.3, first row). The first structure has a vertical gain sidewall, whose radius is set to match that measured at the center of gain of the fabricated device, but has as-fabricated pedestals (Table 4.3, second row); the second structure has a realistic undercut ratio between the upper and lower pedestal, albeit all sidewalls are set to vertical (Table 4.3, third row); and the third structure has vertical sidewalls and equal amount of undercuts in the upper and lower pedestal (Table 4.3, fourth row). Table 4.3 lists the simulated optical mode characteristics including λ_{cav}, g_{th}, Q and Γ, of the four structures at 77K. We notice that the idealized structures typically have much better performance. For structures with small undercut depth, such as the as-fabricated device, non-vertical sidewalls in particular prove detrimental to cavity Q, due to increased radiation loss to the substrate; such an effect has also been observed in simulations of non-undercut lasers [8]. A significant decrease in Q is also associated with a laser whose ratio of upper to lower pedestal diameter matches that obtained in experiment (0.8, as opposed to 1.0). This may be because the decreased upper pedestal diameter forces the mode more toward the bottom of the gain region, where it is more likely to be transferred to the bottom pedestal and scattered.

4.5 Device analysis - electrical and thermal

In this section, we analyze the self-heating effects in the fabricated nanolaser at 300K, where material parameters are more available than those at the experimental ambient temperature of 77K. We apply the effective heat source model used in VCSELs ([30]. §5.3), but modify it to include the heat generated from non-radiative recombination in the active region, which is insignificant in micro- or large-scale lasers, but which can play an important role in the self-heating of nanolasers. We consider Auger recombination, which is significant at high temperatures and/or carrier densities, as well as surface recombination, which is significant at high temperature and/or surface-to-volume ratios, as is the case in nanolasers. Therefore, we also include a heat source in the gain region which is attributed to non-radiative recombination, assuming that all non-radiative energy is converted to lattice vibration through the creation of phonons.

The rest of the cavity self-heating can be categorized into three mechanisms. The first mechanism is junction heating, the heat generated at the interfaces between the doped semiconductors and the un-doped gain region. The second mechanism is heterojunction heating, which is heat generated at all doped semiconductor layer interfaces. Both are expressed as $I.V_{jn}$, where I denotes current and V_{jn} is the potential difference at the nth junction. These two terms take the same form below threshold, where I is the injection current I_{inj} Above threshold, I for junction heating is clamped at the threshold current I_{th}, while the heterojunction heating continues to take I_{inj}. The third type of heating is Joule heating due to the series electrical resistance in all doped semiconductor layers, and takes the form $(I_{inj})2.R_n$, where the resistance R_n of the nth layer is calculated using our geometrical parameters, the doping concentration, and carrier mobility of the corresponding layer [32].

We use the software SILVACO's ATLAS, a two-dimensional electronic device simulator, to predict the heterojunction and junction heating. At each pump level, we obtain the potential difference necessary to forward bias the junctions, the carrier density, as well as the electron and hole quasi-Fermi levels (QFL). Given the operating temperature and properties of the device's constituent materials, SILVACO self-consistently solves the Poisson equation, the Schrodinger equation, and the carrier transport equations considering Fermi-Dirac statistics. Because sidewall angles are not expected to be as critical to the device's electrical behavior as to its optical behavior, for simplicity we model a range of devices with straight sidewalls, similar to those shown in the last two rows of Table

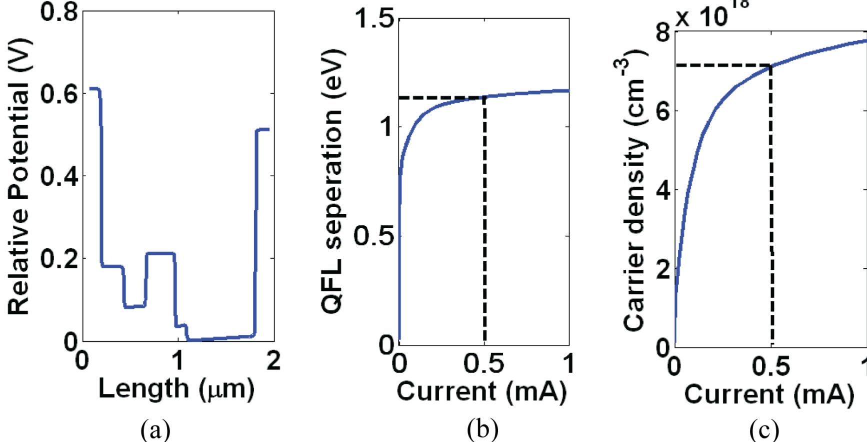

Figure 4.4: Electrical simulation results: (a) Potential difference across the pillar at 0.5mA bias current, where Length=0 corresponds to the top of the structure. (b) QFL separation as a function of bias current. (c) Carrier density as a function of bias current.

4.3, and vary the gain and pedestal radii within the range of widths measured in our fabricated device. We found that such variations did not affect the device's performance significantly; thus we take the average of the results.

At an injection current of 0.5mA, Fig. 4.4(a) plots the simulated electric potential along the pillar length with respect to the minimum potential level. Length=0 corresponds to the top of the laser pillar (the top of the n− InGaAs layer), and the device temperature is set to be 300K. From the voltage rise or drop at each interface, we calculate the amount of junction and heterojunction heating at the respective interfaces. Junction heating, summed from the contribution from the InP and InGaAs gain interfaces, is 0.122mW. We obtain heterojunction heating of 0.517mW in a similar manner. Joule heating is estimated to be 0.214mW. To calculate heating generated by non-radiative recombination, we first obtain the carrier density and the QFL separation as a function of bias current from SILVACO, plotted in Fig. 4.4(b) and (c), respectively. At 0.5mA, using the corresponding carrier density, the QFL separation which describes the transition energy, as well as the surface velocity and Auger coefficient at 300K [75], we estimate the heating to be 2.621mW. The total estimated heat source power at 0.5mA current is 3.474mW, comparable to the experimental value of 3.375mW injection power. We note that, in calculating the junction heating, we had used a threshold current of 0.4mA, as roughly estimated in Section II. If this value was under-estimated, junction heating would correspondingly increase. However, we do not expect this difference to

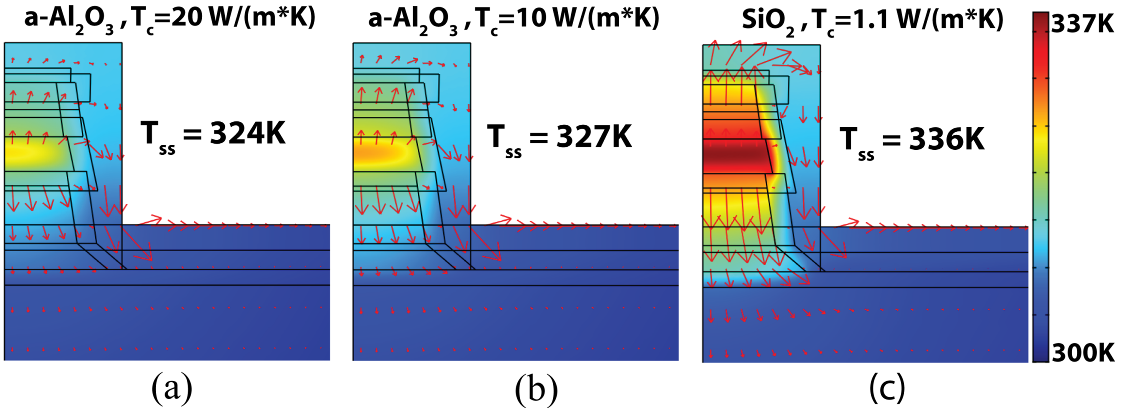

Figure 4.5: Temperature distribution, steady-state temperature T_{ss} and heat flux (indicated by the red arrows) of the fabricated device, with α-Al_2O_3 shield, taking (a) the highest literature thermal conductivity value of 20W/(m.K), (b) medium literature thermal conductivity value of 10W/(m.K). (c) SiO_2 shield with well-calibrated literature thermal conductivity value of 1.1W/(m.K).

affect the thermal performance significantly, because non-radiative heating is an order of magnitude greater than junction heating at such high injection levels. We also recognize the discrepancy between the experimental and simulated bias voltages at the same injection current. This is most likely due to the non-ideal Ohmic contacts of the fabricated device as well as defects at material interfaces, the behavior of which is not captured in the simulation, but which may contribute resistive and/or Schottky heating.

The heat sources at the various junctions and layers are subsequently input into COMSOL's 2D axial-symmetric steady-state heat conduction model for thermal analysis. In this model, the structure matches the fabricated geometry, including sidewall angles and undercut amounts. The bottom surface of the 350μm thick InP substrate is kept at the constant ambient temperature of 300K, and the far edge of the 220nm thick Ag cavity metal coating, 20μm from the laser, as schematically drawn in Fig. 4.1, is also set to 300K, allowing the possibility of heat conduction through the metal cladding layer. All other boundaries are set to symmetry/insulation, except for the top surface of the Ag, which is allowed to lose heat through radiation. The thermal conductivities of the constituent materials are listed in Table 4.1. Because the literature thermal conductivity T_c values for ALD-deposited α-Al_2O_3 range from 1.7 to 20W/(m.K), we perform two simulations with T_c of 20 and 10W/(m.K), respectively. For the lowest T_c value of 1.7W/(m.K), the thermal performance approaches that of a device with SiO_2 shield, which we also simulate for comparison.

Fig. 4.5 shows the temperature distribution, steady-state temperature T_{ss} and heat flux of the fabricated device, with different shield materials and/or thermal conductivities. We notice that while a higher thermal conductivity corresponds to a lower steady-state temperature, the steady-state temperatures reached with a lower-conductivity shield are also moderate. This is a consequence of the relatively large gain core diameter, which mitigates surface recombination and Joule heating, as well as the large upper and lower pedestals, which mitigate Joule heating and provide a large pathway for heat dissipation. Nonetheless, the arrows indicating the magnitude and direction of the heat flux highlight the advantage of the α-Al_2O_3 over SiO_2. In the case of the α-Al_2O_3 shield, a significant portion of the heat generated in the pillar is dissipated through the shield into the cavity metal. In the case of the SiO_2 shield, the path for heat dissipation is limited to the semiconductor pedestals.

Because material gain is dependent on the device temperature and pump level, it is beneficial to calculate the gain spectrum at different pump levels and the corresponding SILVACO – calculated carrier densities. This analysis procedure is detailed in Section V, when we design a device for room temperature operation. For the present purpose of analyzing the fabricated nanolaser, we note that material gain decreases as temperature increases, and consequently, lasing is harder to achieve, with all else equal. This decrease in material gain can be compensated by increased pumping, but at the expense of a broadened and blue-shifted material gain spectrum, leading to mode competition. Additionally, the surface recombination rate is related to the square root of temperature, and can become significant at high temperatures [75]. None of these effects is captured in the electromagnetic model alone. Combining all aspects of the analysis, we believe that the absence of lasing behavior of the fabricated device at temperatures higher than 77K is a result of the optical mode's high threshold gain (Table 4.3), rather than the self-heating in the device. In support of this conclusion, we compared the experimental performance of this device under CW and pulsed electrical pumping, with duration and repetition rate of the pulsed pumping chosen to reduce device heating. We observed similar performance of this device under CW and pulsed pumping, further indicating that self-heating had no major effect on the device.

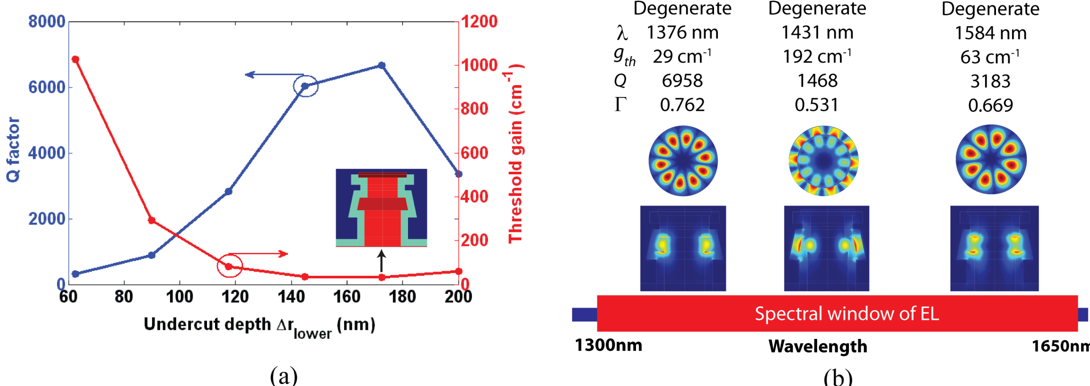

Figure 4.6: Room-temperature optical simulation results for laser with undercut: (a) Threshold gain g_{th}, cavity Q-factor, and diagram of the structure with the lowest g_{th} (b) Mode distribution of all modes that fall within the spectral window of EL and have g_{th} $< 200\text{cm}^{-1}$, for the device geometry shown in (a).

4.6 Cavity design for room-temperature operation

Keeping all geometrical parameters the same as the fabricated device (Fig. 4.2(e)) except for the amount of InP undercut, we design a structure that would operate at room temperature. We increase the pedestal undercut to improve the mode confinement and thus Q-factor and threshold gain, similar to [22]. Different from [22], we use a realistic upper and lower pedestal width ratio obtainable from the two-step InP selective etching process (which etches the differently-doped upper and lower pedestals at different rates). We use the experimentally-measured gain and top n- InGaAs layer sidewall angles; as we will show, even with angled gain sidewalls, a high degree of mode confinement to the gain region is possible. Here, we model vertical pedestal sidewalls, while noting that the sidewall angles achievable in fabrication will vary, but, compared to the poorly-confined case in Table 4.3, will not have as large a deleterious effect on modes that are well-confined to the gain region. The rigorous investigation of the effects of non-vertical pedestal sidewalls, combined with non-vertical gain sidewall and various undercut depths, is outside the scope of this report, but is a subject of future research.

The improvement of optical properties of the mode with increasing undercut depth is shown in Fig. 4.6(a), which shows the threshold gain gth and Q-factor of the lowest gth mode, at each undercut level. As the undercut depth increases, the mode's optical properties initially improve dramatically, as the mode is increasingly isolated from the substrate by the low-index shield and metal. Eventually, the mode becomes highly

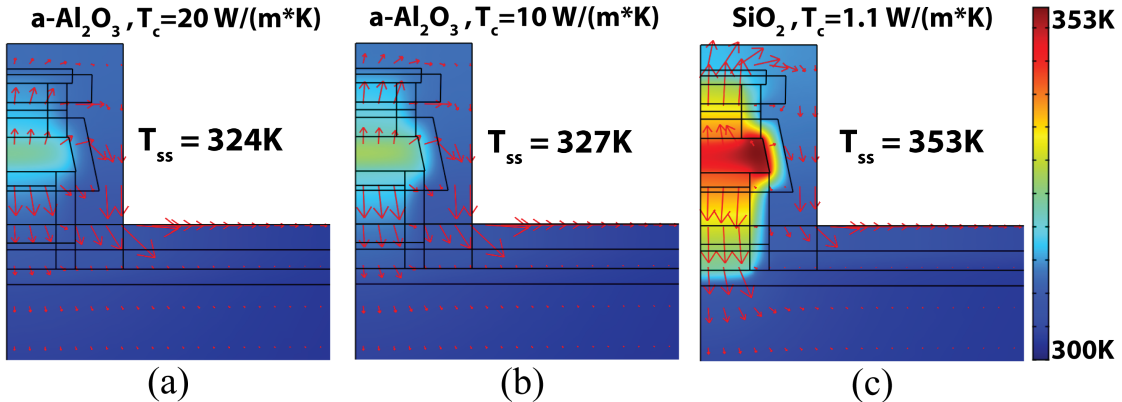

Figure 4.7: Temperature distribution, maximum steady-state temperature T_{ss} and heat flux (indicated by the red arrows) of the designed device, with (a) α-Al_2O_3 shield with the highest literature thermal conductivity value of 20W/(m.K), (b) α-Al_2O_3 shield with medium literature thermal conductivity value of 10W/(m.K), and (c) SiO_2 shield with well–calibrated literature thermal conductivity value of 1.1W/(m.K).

isolated from the substrate, making substrate scattering negligible, and the improvement saturates. Meanwhile, the cavity resonant wavelength of each mode blue-shifts as the undercut depth increases, and eventually, moves outside of the wavelength window of interest, 1300nm to 1650nm. This behavior is captured in Fig. 4.6(a): at Δr_{lower}~200nm, the original lasing mode has blue-shifted beyond the gain bandwidth window, leaving a higher order mode to take its place as the lowest gth mode, which has a lower Q and a slightly higher gth than the original mode. We define the optimal undercut depth to be the depth of the lower InP pedestal, Δr_{lower}, which is the lesser of the two undercuts, that corresponds to the minimum threshold gain in Fig. 4.6(a). We find the optimal Δr_{lower} to be 174nm, more than two times larger than that obtained in [22], which was $\Delta r_{lower}=\Delta r_{upper}$~80nm for both the R_{core}=350nm and 750nm structures. This optimal undercut design is shown in side view at the bottom of Fig. 4.6(a). Fig. 4.6(b) depicts the target structure's λ_{cav}, the electric field distribution, g_{th}, and Γ, for modes with $g_{th}<200cm^{-1}$ and whose resonant wavelengths fall within the material EL spectrum of 1300–1650nm. Compared to the fabricated structure with g_{th} of $10610cm^{-1}$ at 300K, a 99.7% reduction in threshold gain is obtained.

For the thermal analysis, following the procedure outlined in Section IV, we use SILVACO to estimate the heat generation in various regions of the device, at the same 0.5mA injection current used in Section IV. Fig. 4.7 shows the temperature distribution, maximum steady-state temperature T_{ss} and heat flux of the designed device, with dif-

Table 4.4: Simulated optical characteristics of the lowest-threshold gain mode of the designed device at 77K, 300K, and 327K

Temperature (K)	λ_{cav} (nm)	g_{th} (cm^{-1})	Q	Γ
77	1376	5	43350	0.762
300	1376	20	6958	0.762
327	1376	31	6487	0.762

ferent shield materials and/or thermal conductivities. The total heat generated in the undercut laser design is higher than that of our fabricated device (Fig. 4.5), largely attributed to the increase in Joule heating in the pedestal layers and junction heating at the interface between the lower InP pedestal and the highly doped p+ InGaAsP layer. Because this heating occurs near the edges of the laser stack, where heat may be more readily dissipated through the substrate and metal shield, the impact of this additional heating is minimal. In addition, SILVACO predicts ~2% decrease in carrier density of the designed device compared to that in the fabricated one, leading to a ~5% decrease in non-radiative heating power generated in the gain layer. The net effect is that the final temperature in the T_c=20W/(m.K) α-Al_2O_3 shield device is actually a fraction of a degree lower than that of the as-fabricated device, while the T_c=10W/(m.K) α-Al_2O_3 shield device is a only fraction of a degree higher than that of the as-fabricated device. In the case of the SiO_2 shield, however, we observe a 17K rise. This observation agrees with intuition: as the undercut is made deeper, and the pathway for heat dissipation through the pedestals decreases, the ability to dissipate heat through the shield layer becomes more important. We expect the same trend as the gain core radius is decreased.

Next, we analyze the optical performance of our design at the operating temperatures of 77K, 300K, and 327K (taking ε(Ag,327K)=−130.4−0.569i [9]); the latter is the predicted steady-state temperature (assuming a modest T_c value of 10W/(m.K) for the α-Al_2O_3 shield) when operated at an ambient temperature of 300K. The optical characteristics of the lowest threshold gain mode of the designed device, in terms of resonant wavelength λ_{cav}, cavity Q-factor, mode confinement factor Γ, and threshold gain gth, are tabulated in Table 4.4.

Next, we analyze the amount of material gain available at our simulated steady-state operating temperature and lasing wavelength, and compare this to the mode's simulated threshold gain. Following the semiclassical approach of [9], we compute prop-

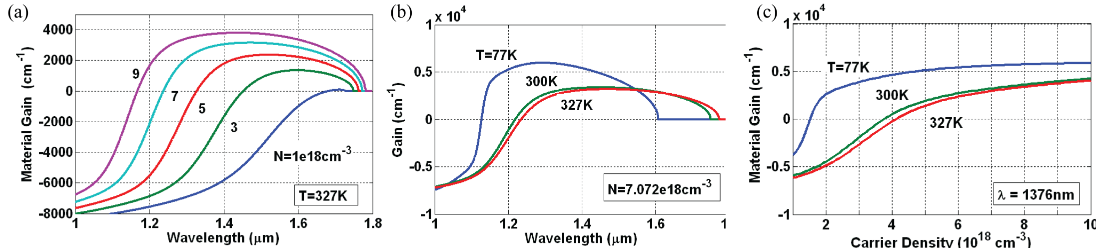

Figure 4.8: (a) Material gain spectrum at 327K, for a range of carrier densities. (b) Material gain spectrum at 0.5mA injection current, corresponding to a carrier density of 7.072e18cm^{-3}. (c) Material gain versus carrier density at the cavity resonance wavelength of 1376nm.

erties of the gain material at 77K, 300K, and 327K. Fig. 4.8(a) shows the material gain spectrum for a range of carrier densities from 1e18cm^{-3} to 9e18cm^{-3}, at 327K. At the 0.5mA injection current used in the thermal and electromagnetic simulations above, we find the carrier density of our designed device to be 7.072e18cm^{-3}. We plot the material gain spectrum at this injection (Fig. 4.8(b)), as well as the material gain with increasing carrier density at the wavelength of the lowest-threshold mode, 1376nm (Fig. 4.8(c)). Comparing the available material gain at the carrier density of 7.072e18cm^{-3} with the predicted threshold gain values listed in Fig. 4.6(b), even though the mode simulations do not capture the non-radiative loss that is directly related to temperature and carrier density, we expect that the laser could be operated at a much lower injection level than the 0.5mA considered. Lastly, with a very slight change in the gain core radius, the cavity mode can be tuned to fall in the middle of the gain spectrum. A similar highly-undercut approach will likely work for other shield materials, shield thicknesses, and gain volumes as well; a generalized investigation is the subject of future research.

4.7 Discussion

In the preceding sections, we detailed the first attempt at the joint consideration of the optical, electrical, thermal, and material gain properties of nanolasers, as well as proposed a shield that promises to mitigate current difficulties with nanolaser heat dissipation. We experimentally demonstrated this shield in a metallo-dielectric nanolaser design, and showed that fabrication differences from the idealized design explains the device's poor performance, including a failure to lase at higher pump powers or temperatures above 77K. Indeed, although the linewidth was observed to narrow, the device

may never have reached lasing threshold. This conclusion is supported by our realistic numerical models, which used geometrical parameters from our fabricated device, and predicted dramatically worse Q-factor and gain threshold than those achieved under the vertical sidewall and equal-undercut approximations typically used for numerical modeling. Indeed, this high threshold gain, which we found to be attainable for modest carrier densities only at low temperatures, was the major limitation preventing room-temperature lasing. Our thermal simulations showed that self-heating, often blamed for poor laser performance, was minimal in our case. Next, we predicted that a slight increase in undercut should enable room temperature behavior in a device with the same footprint and gain volume. We further validated our prediction by simulating our design's thermal performance, and found that the improved optical performance carried little to no penalty in terms of increased device self-heating. Finally, we compared our design's threshold gain to the available material gain at our predicted device operating temperature, and found that room-temperature lasing should be possible. Our simulations also show the thermal advantages of α-Al_2O_3 over SiO_2, an effect that is especially prominent as the pedestal undercut depth increases and/or the device size decreases.

As we have shown, the differences between nanolaser designs and the devices actually fabricated can have profound effects on device performance. Our proposed highly-undercut design assumes a gain and top contact sidewall angle that matches the experimentally-produced angle; in reality, this sidewall angle will vary from chip to chip, and even from the nanolaser's location within a single chip. In addition, we used the experimentally measured ratio of undercut depth $\Delta r_{upper}/\Delta r_{lower}$=0.8; generally, $\Delta r_{upper}/\Delta r_{lower}$ becomes smaller as Δr_{lower} becomes greater, and also depends on the nanolaser's location on the chip. Furthermore, while we had assumed the InP pedestals to both have vertical sidewalls, this is typically not the case, as is evidenced in Fig. 4.2(c) where we obtained a vertical upper pedestal but an angled lower one. To minimize the difference between designed and fabricated devices, controllability and repeatability in creating the InP undercut is of importance. We are currently working toward improving this fabrication step, as well as toward an analysis of the effects of this variation on nanolaser performance. We expect that these efforts will lead toward a future experimental demonstration of improvement via increased undercut. Furthermore, to ensure the robustness of our design, it should be shown to perform well across the range of experimentally observed variation in fabrication. These indeed are ongoing

research efforts but are not within the scope of this report.

In our thermal studies, we used the average of a range of thermal conductivities for α-Al_2O_3, from reported literature values. To obtain the value for a specific film, a 3-ω measurement can be conducted [44]. This measurement, however, is non-trivial, due to errors introduced by the two-dimensional heat spreading effect in the upper layer of the target film [76]. The precise determination of the heat conductivity of the deposited α-Al_2O_3 in our devices, as well as the optimization of the α-Al_2O_3 deposition technique for increased thermal conductivity, is a subject of future work.

In addition to α-Al_2O_3, other dielectric materials may also show promise as heat-dissipating shields. Recently, aluminum nitride (AlN) has emerged as an effective passivation material, when prepared by plasma-enhanced ALD [77]. With a higher thermal conductivity than α-Al_2O_3, AlN can be explored as an alternative shield material.

We recognize that our analysis does not fully capture the dynamics of the nanolaser's thermal behavior. As the steady-state temperature of the device rises above the ambient temperature, constituent materials' thermal parameters would accordingly change. Thermal feedback mechanisms should be included in future analysis. Furthermore, the heat conduction model in COMSOL, which uses macroscopic heat transfer equations, may break down on the micro-/nano- scale. When the device dimension becomes comparable to or smaller than the mean free path of constituent materials' heat carriers, we enter the microscale heat transfer regime [78]. Microscale conductive and radiative heat transfer in VCSELs and convective heat transfer in carbon nanotubes have been studied [78], although it has not been a subject of attention in the field of nanolasers.

In conclusion, the use of α-Al_2O_3 may improve the stability and reliability of CW electrically pumped nanolasers, and enable the design of laser cavities with new functionality, which have till now proven too lossy or too prone to self-heating for practical consideration. The broader treatment of nanolaser design demonstrated here, which considers the interplay of optical, electrical, thermal, and material gain properties, should greatly aid in the understanding of laser dynamics, as well as the development of new nanolaser designs.

4.8 Acknowledgements

The authors would like to thank Dr. Boris Slutsky and Mr. Dor Gabay for helpful discussions.

This chapter, in full, is an adaptation of the material as it appears in IEEE Journal of Quantum Electronics, 2014. Qing Gu, Janelle Shane, Felipe Vallini, Brett Wingad, Joseph S. T. Smalley, Newton C. Frateschi, and Yeshaiahu Fainman. (2014) The dissertation author was the second investigator and author of this paper, and performed the optical and thermal simulation work.

Chapter 5

Effect of undercut etch on performance and fabrication robustness of metal-clad semiconductor nanolasers

5.1 Abstract

We use optical, thermal, and electrical simulation to evaluate the effects of using varying amounts of undercut etch on wavelength-scale and sub-wavelength metal-clad semiconductor nanolasers (MCSELs). We find that as MCSEL diameter decreases, the optical performance becomes more sensitive to slight amounts of sidewall tilt. A modest amount of undercut (25%) dramatically improves optical performance, reducing modal threshold gain to 100cm^{-1} or lower for lasers with core radius of 225nm, 550nm, or 775nm, even in the presence of significant sidewall tilt (20° gain sidewall, or ±8° pedestal sidewall tilt). Finally, we examine the effects of the increased undercut on nanolaser thermal performance and find that the increased resistive heating is insignificant near threshold, even for subwavelength nanolasers.

5.2 Introduction

Metal-clad semiconductor nanolasers (MCSELs) have been improving in robustness and reliability since their first demonstration by Hill and colleagues in 2007[7]. This class of laser has a cavity enclosed by metal, providing mode confinement [79, 80] and thus decreasing laser and mode footprint to subwavelength scale in all three dimensions[7]. Attractive as wavelength-scale or subwavelength light sources for sensing or dense chip-scale photonic integration, MCSELs have advanced beyond their original optically-pumped[20] and/or cryogenic[7, 22] demonstrations to CW electrically-pumped subwavelength sources operating at room temperature[19]. As MCSELs move beyond these first proof-of-principle demonstrations, efficiency and robustness are both issues that future laser designs will need to address.

A major measure of the efficiency of a nanolaser is the threshold gain of the lasing mode. A low threshold gain not only makes the most efficient use of the pump, but also minimizes the effects of self-heating, which includes terms with square and cubic dependencies on pump current. At higher pump currents, the phenomenon of self-heating can raise the temperature in the gain region, here referred to as the laser's operating temperature, well above that of the ambient temperature. At higher temperatures, the cavity metal becomes more lossy[9], a particularly detrimental effect for nanolasers with high modal overlap with metal[21]. Additional self-heating will reduce the available material gain, and at extreme temperatures may destroy the laser. Even if heat can be effectively dissipated, the gain spectrum broadens and blue-shifts at higher currents, which can shift the gain maximum away from the designed cavity mode[9]. To increase laser output power and efficiency while avoiding the detrimental effects of self-heating, it is critical to reduce threshold gain.

Many strategies have been employed to reduce threshold gain in nanolasers. The threshold gain g_{th} of a lasing mode is defined as

$$g_{th} = \frac{n\omega_0}{c\Gamma Q}$$

where ω_0 is the modal frequency, n is the refractive index of the gain medium, c is the speed of light in vacuum. Γ is the mode-gain overlap, related to how well the cavity confines the mode to the gain region, while Q is the mode's quality factor, related to the amount of scattering and material absorption loss the mode experiences. Efforts to reduce threshold gain in MCSELs need to target Γ, Q, or both. For example, adding a thick

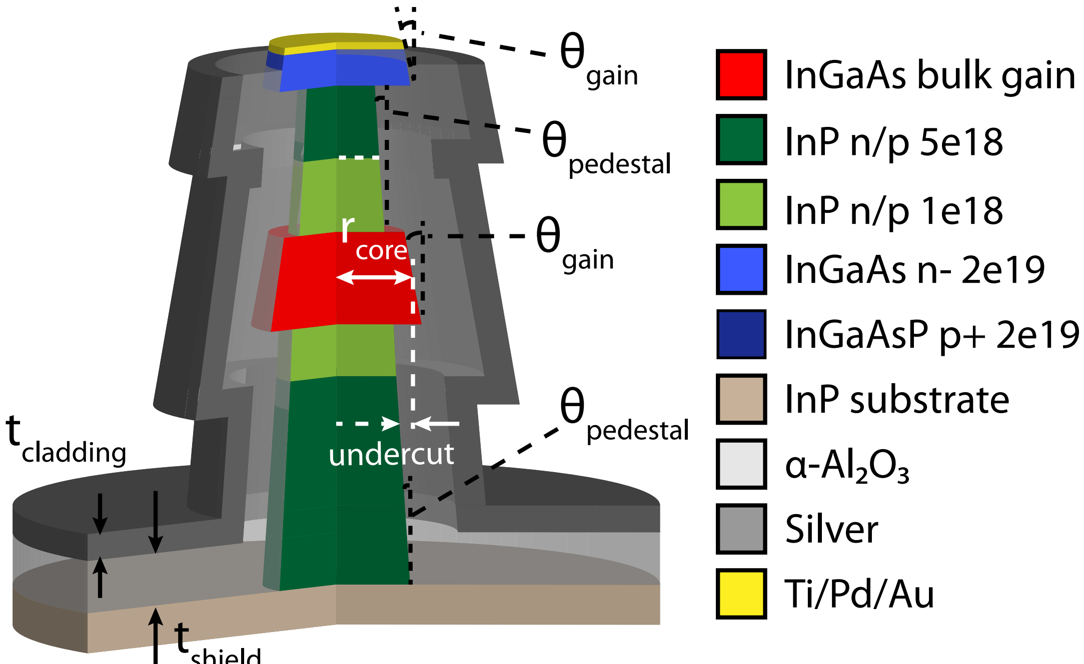

Figure 5.1: Diagram of an example simulated nanolaser, with gain sidewall angle θ_g and pedestal sidewall angle θ_p both positive. In the optical simulations, the area surrounding the silver cladding layer is also silver, since the skin depth of the emission wavelength is only a few nanometers. In the thermal simulations, the area surrounding the cladding is air. The laser is allowed to dissipate heat through the bottom of the 350 μm thick InP substrate, through radiation to air, and through a thermally conductive contact wire attached to the cladding 20 μm away.

dielectric shield between the gain and the metal cladding reduced the amount of modal overlap with the metal, increasing Q enough to allow room temperature operation[21, 20]. For electrically pumped MCSELs, an added challenge is the necessity of providing a pathway for electrical injection of carriers into the gain region; this necessitates the use of doped semiconductor pedestal layers above and below the gain region, impacting gain confinement due to the low refractive index contrast between pedestal and gain. A strategy used to reduce threshold gain in electrically pumped nanolasers is to undercut the pedestal layers, decreasing mode penetration into the surrounding semiconductor layers[22]. An example electrically pumped MCSEL with dielectric shield and undercut pedestals is shown in Fig. 5.1.

Any nanolaser design needs to not only have low g_{th}, but should also be robust with respect to fabrication variation. One of the major issues encountered during MC-

SEL fabrication is non-vertical gain and pedestal sidewalls. Even a slight sidewall tilt of a degree or less can be enough to profoundly affect the g_{th} of a fabricated nanolaser[81, 8]. Gu and coworkers analyzed the performance of a fabricated electrically-pumped device and found that the non-zero sidewall tilt achieved during fabrication raised g_{th} to the degree to which lasing was unlikely even at cryogenic temperatures[23]. One method of dealing with the detrimental effects of sidewall tilt is careful calibration of the etching process to compensate for regular fluctuation in etching chamber conditions; to consistently achieve sidewalls with less than a degree of tilt several calibration test samples must be etched and imaged before each nanolaser sample is etched[8].

In this paper, we show that undercut etching, already useful for reducing MCSEL g_{th}, also makes the nanolaser resistant to the effects of sidewall tilt. In Section 5.3.1 we first expand on the work of Ding and coworkers[8] by examining the effects of sidewall tilt on nanolasers without undercut, having core radii of 225nm, 550nm, and 775nm. We find that the effects of sidewall tilt become more dramatic as core radius decreases. In Section 5.3.2 we show that a moderate undercut (25%) eliminates the detrimental effects of sidewall tilt, producing threshold gains that would allow room-temperature operation even for nanolasers with gain sidewall tilts of 20°. We find that a 25% undercut will produce similarly good results regardless of nanolaser diameter, gain sidewall angle, or pedestal sidewall angle. In Section 5.4 we then analyze the effects of these undercuts on the heat generated by the nanolaser, and find that the additional undercut has no significant effect on the nanolaser self-heating, or on final operating temperature for a laser operating within an order of magnitude of threshold. In all cases, undercutting significantly lowered g_{th} compared to a laser with no undercut. We conclude that undercutting is a robust strategy for reducing threshold gain and sensitivity to sidewall angle, while carrying no significant heat penalty.

5.3 Optical simulation

5.3.1 Effect of sidewall tilt on threshold gain for lasers without undercut

The typical pedestal MCSEL fabrication process begins with the use of electron beam lithography to create a mask that defines the pillar's footprint, followed by reactive ion etching (RIE) to create the pillar. Depending on small fluctuations in etching chamber

conditions, an etching recipe calibrated to create vertical sidewalls may often produce angled sidewalls. Ding and Ning examined the effects of angled sidewalls on the TE_{01} mode of a nanolaser with 230nm radius and found that even a slight 1-2° sidewall tilt causes a factor of 5 decrease in cavity Q[8].

We use 3D finite element simulation (COMSOL) to simulate the effects of different amounts of sidewall tilt on nanolasers of different core radius. Each nanolaser is created from the InP/InGaAs/InP double heterostructure used in [7, 22, 23], whose gain medium is a 300nm thick layer of intrinsic bulk $In_{0.53}Ga_{0.47}As$. The lasers each have 170nm thick shields of α-Al_2O_3 (amorphous aluminum oxide), surrounded by silver cladding. We model the materials using their optical parameters at a temperature of 300K and a wavelegth of 1550nm; the permittivity used for silver is -130.6-3.33j, as calculated using a temperature-dependent Drude model and data from Johnson and Christy[71] by Smalley et al[9]. Each laser is fully etched to the bottom contact layer, giving the laser a height of 1745nm measured from the top of the top contact to the bottom of the pillar. We vary the angle of each laser's sidewalls while keeping the average gain radius constant; results are shown in Fig. 5.2.

From the simulation results, we find that nanolasers of 225nm, 550nm, and 775nm core radius are all sensitive to the effects of sidewall tilt, with the lasers suffering from increased radiative loss through the laser pedestal and decreased mode confinement as tilt increases. The effects of sidewall tilt become more extreme as gain radius decreases. In agreement with Ding and Ning[8], we find that a subwavelength nanolaser designed for the TE_{01} mode is extremely sensitive to sidewall angle. For the laser with core radius of 225nm (Fig. 5.2 b), a sidewall tilt of just 0.5° yields a threshold gain exceeding 1000 cm^{-1}, making room-temperature operation unlikely for our gain material at this wavelength, and inefficient for other gain materials. For larger nanolasers, the effects of sidewall tilt are still severe, with threshold exceeding 1000 cm^{-1} at 2° tilt for the 550nm core laser (Fig. 5.2 c), and at 3° tilt for the 775nm core laser (Fig. 5.2 d).

Some method of dealing with sidewall tilt is clearly needed if nanolasers are to be reliably produced for room-temperature operation. One strategy that has been successfully employed is to recalibrate the etching recipe each time a nanolaser sample is to be etched[8]. An alternative strategy that would avoid the time and expense of frequent recalibration is to develop a nanolaser design that is insensitive to the effects of sidewall tilt.

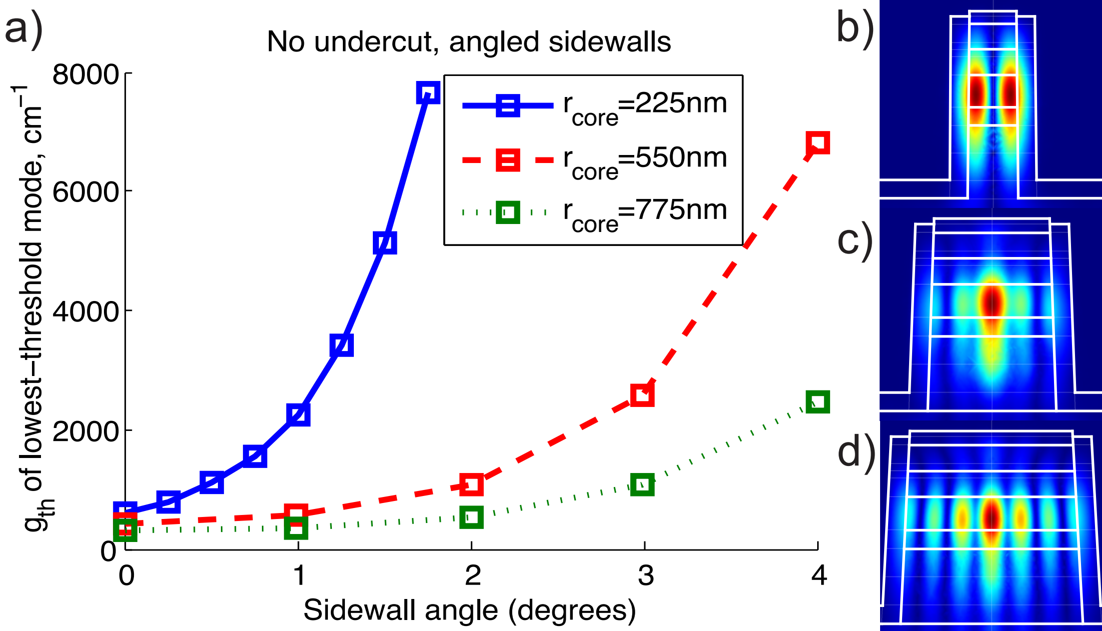

Figure 5.2: Effect of sidewall angle on lasers without undercut: (a) Threshold gain of the lowest-threshold modes for modeled lasers with average gain radius of 225nm (blue solid line), 550nm (red dashed line), and 775nm (green dotted line), as a function of laser sidewall angle. These lasers have no undercut etch. (b-d) Electric field of the lowest threshold mode for lasers with enough sidewall tilt to give them thresholds of about 1000 cm^{-1}. (b) Laser with r_{core} = 225nm and sidewall angle of 0.5°. (c) Laser with r_{core} = 550nm and sidewall angle of 2°. (d) Laser with r_{core} = 775nm and sidewall angle of 3°.

5.3.2 Effect of undercut etching on threshold gain for lasers with sidewall tilt

Here, we investigate the strategy of undercut etching for consistently producing MCSELs with low threshold gain, even in the presence of significant sidewall tilt. In this paper, “undercut” refers to the lower undercut, defined as the difference between the average radius r_{core} of the gain core and the average radius of the lower pedestal, as a percentage of r_{core} (see diagram in Fig. 5.1).

Undercut etching was used by Lee and colleagues to increase the vertical confinement in pedestal nanolasers by reducing the diameter of the pedestals relative to the gain region[22]. Another investigation looked at the effect of undercut etching on the optical properties and operating temperature of an optically pumped laser, where the self-heating is assumed to be independent of the amount of undercut etch[82]. Both of these investigations only considered vertical gain and pedestal sidewalls, and a single

laser diameter. In our case, we consider three laser diameters and a variety of gain and pedestal sidewall angles, based on those achieved during our nanolaser fabrication.

An example nanolaser with undercut etching and sidewall tilt is drawn in Fig. 5.1. Since the wet etching chemistry selectively etches the pedestal semiconductor layers and leaves the gain region intact, the amount of undercut can be controlled by adjusting the length of the wet etch step, usually on the order of a couple of seconds. The use of a two-step undercut etching process, with each step producing positively or negatively sloped pedestal sidewalls, allows the angle of the pedestal sidewall to be controlled[23].

The resulting etched nanolasers can have pedestal sidewall angles θ_p that are positive, negative, or zero, independent of the gain sidewall angle θ_g. Because the gain sidewalls angles are determined by the RIE step, these sidewalls always have $\theta_g \geq 0$. For this semiconductor material stack[7, 22, 23], because of the difference in doping type between the n-doped upper pedestal and the p-doped lower pedestal, the selective etching acts more quickly on the upper pedestal than on the lower pedestal. The result is a laser with a ratio of upper to lower undercut of < 1. Our simulations use an experimentally-measured upper to lower undercut ratio of 0.81; this ratio can vary in practice.

Three example lasers fabricated using the two-step etching process are shown in Fig. 5.3. The laser in Fig. 5.3 (a) has a core radius of 803 nm, $\theta_p = -16°$, $\theta_g = +1.5°$, an undercut ratio of 0.93, and an undercut of 12%, while the laser in Fig. 5.3 (b) has a core radius of 417 nm, $\theta_p = +7°$, $\theta_g = +11°$, an undercut ratio of 0.53, and an undercut of 15%. The laser in Fig. 5.3 (c) has a core radius of 201 nm, $\theta_p = -6°$ (for the lower pedestal), $\theta_g = +6°$, an undercut ratio of 0.61, and an undercut of 43%. These examples illustrate the variation in sidewall angle, as well as the range of undercuts that can be achieved.

To determine the effect of gain sidewall angle, pedestal sidewall angle, and undercut amount, we modeled a variety of nanolasers using COMSOL. For each nanolaser, we searched for modes in the wavelength range near the maximum of the available room-temperature gain. For the r_{core} = 550 nm and r_{core} = 775 nm lasers, we search in the free-space wavelength range λ_0 = 1500 to 1700 nm, which matches the available room-temperature material gain at a moderate carrier density of N= $3 \times 10^{18} cm^{-3}$ for our gain material. For the r_{core} = 225 nm laser, we expand this wavelength range to 1400 - 1820 nm so that as increasing amounts of undercut change the wavelength of the TE_{01} mode, we can still track its behavior. We tested undercut amounts from 0% - 30%

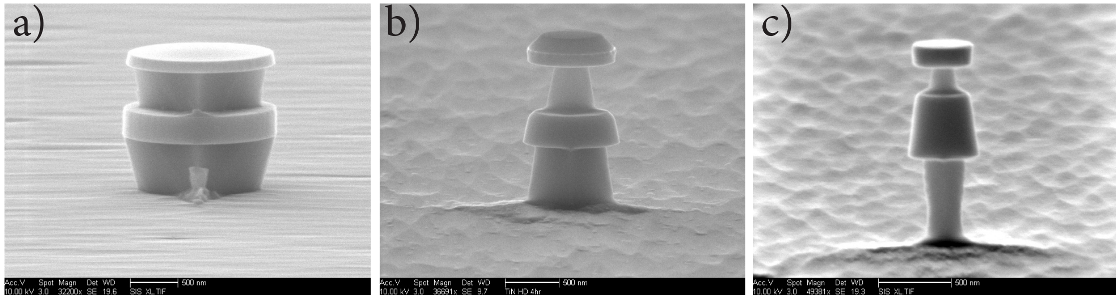

Figure 5.3: SEM images of three example nanolasers fabricated using the two-step undercut etching process[23]. (a) has a core radius of 803 nm, $\theta_p = -16°$, $\theta_g = +1.5°$, an undercut ratio of 0.93, and an undercut of 12%. (b) has a core radius of 417 nm, $\theta_p = +7°$, $\theta_g = +11°$, an undercut ratio of 0.53, and an undercut of 15%. (c) has a core radius of 201 nm, $\theta_p = -6°$ (for the lower pedestal), $\theta_g = +6°$, an undercut ratio of 0.61, and an undercut of 43%. The nanolaser in (c) has a slightly different layer composition than the others in this paper.

for nanolasers of each diameter, and independently varied the gain sidewall angle from $\theta_g = 0°$ to $+20°$, and the pedestal sidewall angle from $\theta_p = -8°$ to $+8°$. Each laser simulated had a dielectric shield of α-Al_2O_3 of thickness $t_{shield} = 170$nm, near the optimum shield thickness for minimum g_{th}. The threshold gain of the lowest-threshold mode for each nanolaser is shown in Fig. 5.4. In Fig. 5.5 we plot other characteristics (λ_0, Q, Γ, and substrate confinement) of the lowest-threshold mode for the $r_{core} = 225$nm laser at gain sidewall angles of $\theta_g = 0°$ and $+20°$; these characteristics display similar behavior for the individual modes of other nanolaser sizes and sidewall angles.

From Fig. 5.4 it is evident that threshold gain decreases with increasing undercut for nanolasers of all three diameters. Threshold gain is very sensitive to sidewall angles for lasers with little to no undercut, but by about 25% undercut, threshold gain is at or below 100cm^{-1} for lasers of any diameter, regardless of the gain or pedestal sidewall angle. Increasing undercut past 25% yields little to no improvement. Fig. 5.5 shows that by 25% undercut, Q no longer increases significantly (b), and radiation to the substrate becomes an insignificant source of loss (d); the limitation on Q becomes metal absorption, which is relatively unaffected by undercut.

For the $r_{core} = 225$nm laser, the decrease in threshold gain is monotonic as undercut increases; this is because the mode wavelength window is chosen such that the TE_{01} mode is always within range, even as the increasing undercut shifts the mode wavelength (Fig. 5.5 (a)). For the larger-radius lasers, the threshold gain of each individual mode still decreases monotonically. However, the decrease in mode wavelength caused by

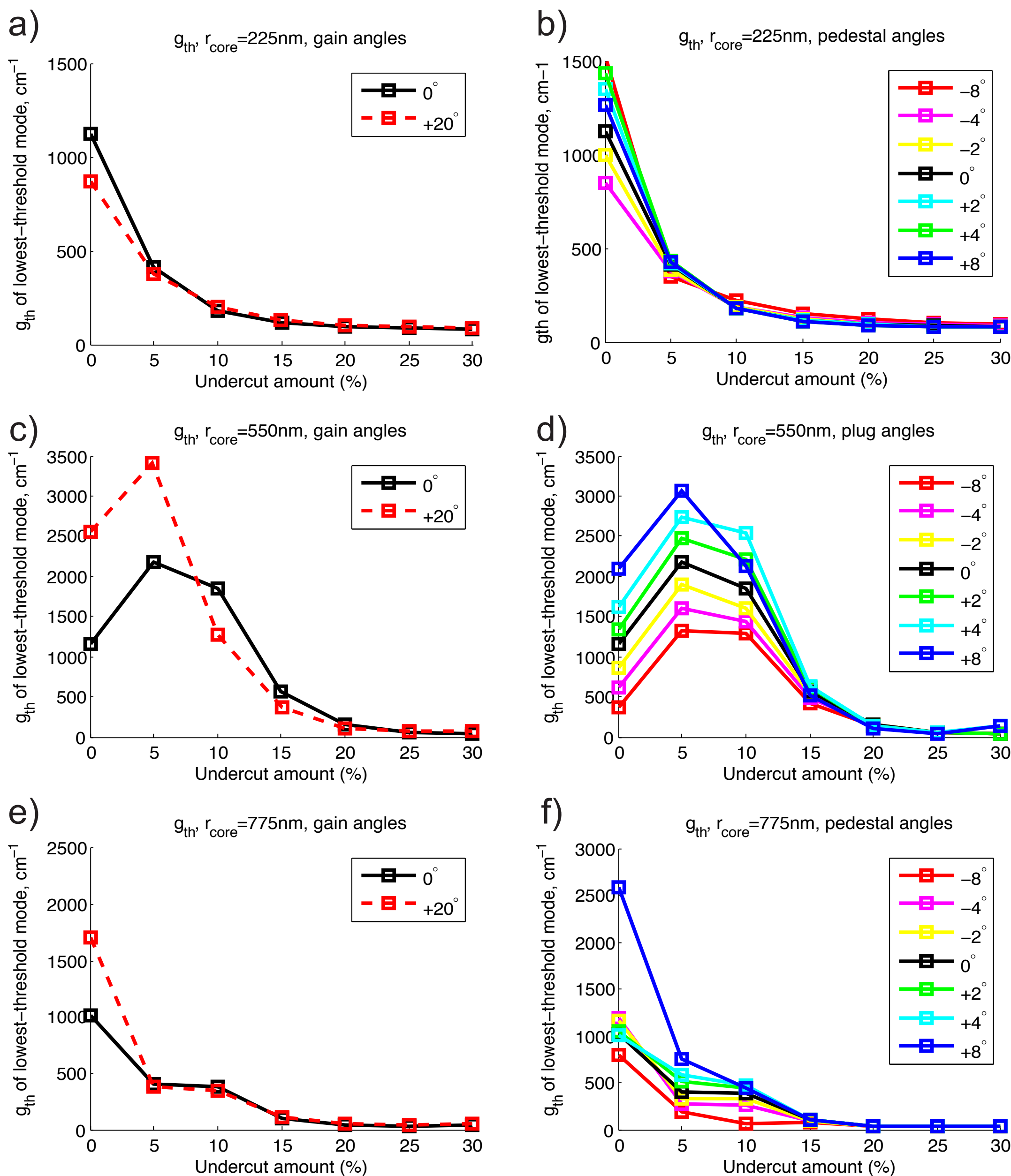

Figure 5.4: Effect of undercut on threshold gain of the lowest-threshold mode for nanolasers of $r_{core} = 225$nm (a-b), 550nm (c-d), and 775nm (e-f). In the left column, the gain sidewall angle θ_g is set to 0° (black solid line) or +20° (red dashed line), while the pedestal sidewall θ_p is kept vertical at 0°. In the right column, the gain sidewall angle θ_g is kept vertical at 0° while the pedestal sidewall θ_p is varied from -8° to +8°.

undercutting is more dramatic for these larger lasers, so that modes that are within the 1500nm - 1700nm wavelength window at 0% undercut quickly are shifted out of the window as undercut increases. For these larger lasers, multiple modes are in the gain window

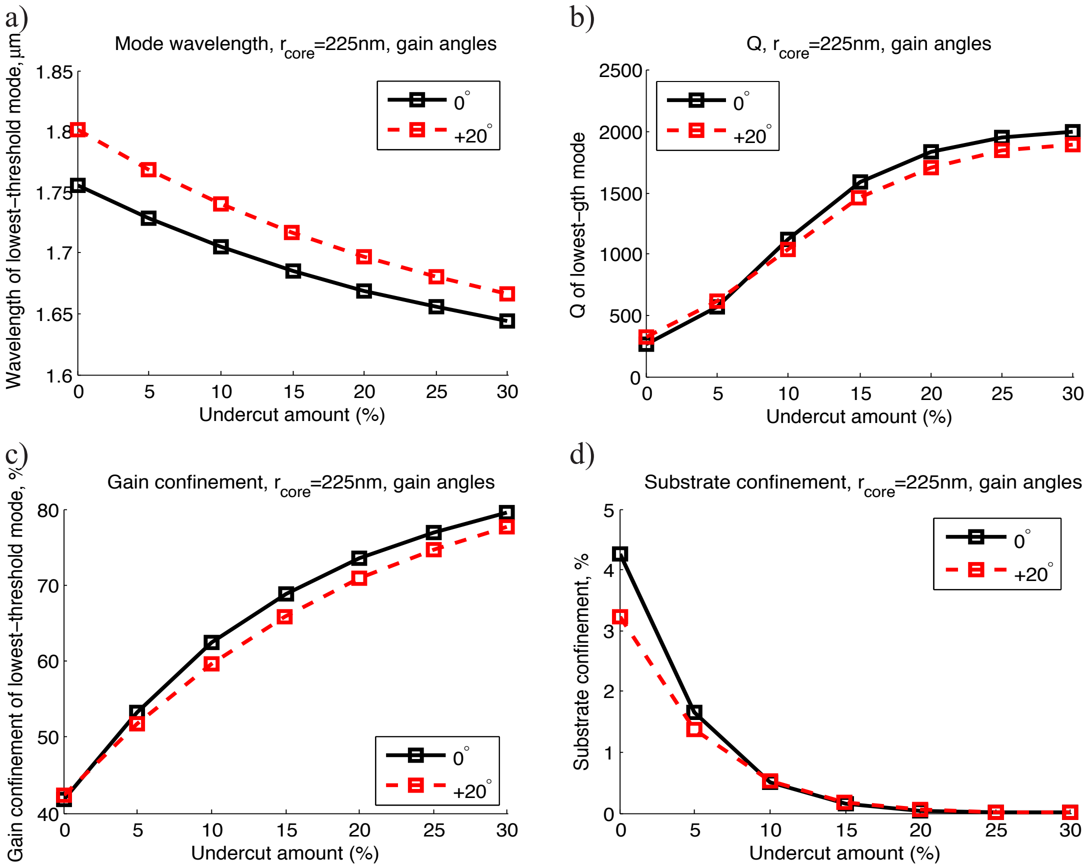

Figure 5.5: Effect of increasing undercut amount on the characteristics of the lowest-threshold mode (TE_{01}) for the $r_{core} = 225$nm laser. Gain sidewall angle θ_g is set to 0° (black solid line) or +20° (red dashed line), while the pedestal sidewall θ_p is kept vertical at 0°. (a) free-space modal wavelength, λ_0. (b) cavity quality factor, Q. (c) percentage of mode confined to the gain, Γ. (d) percentage of mode confined to the substrate.

simultaneously, so once the lowest-threshold mode exits the gain window, the new lowest-threshold mode may have a higher or lower threshold than the previous lowest-threshold mode. By the time undercut increases to around 15%, the mode is highly confined to the gain region, and therefore becomes less sensitive to the pedestal radius. Both the mode wavelength and the threshold gain change less as undercut increases further.

Fig. 5.4 (a) shows that for the r_{core}=225nm laser, when the gain sidewall alone is tilted and the pedestal sidewalls are vertical, at slight undercut amounts a severely tilted gain sidewall actually produces lower threshold than a laser with the same undercut and straight sidewalls. This is because the bottom of a gain region with angled sidewalls overhangs the lower pedestal more than that of a straight-sided gain region, reducing

leakage into the substrate for modes such as TE_{01} and whispering gallery modes, which are concentrated around the laser perimeter. Fig. 5.5 (c) shows the slightly higher gain confinement of the angled design, while Fig. 5.5 (d) shows the significantly reduced radiation into the substrate of the angled design. As the amount of undercut increases, this extra overhang becomes less significant, and the performance of the angled and non-angled sidewalls becomes comparable. For the r_{core}=550nm and 775nm lasers, the lowest-threshold modes at 0 undercut have a higher radial mode order than the TE_{01} and whispering gallery modes, and these modes are penalized by a gain sidewall angle, as seen in Fig. 5.4 (c) and (d).

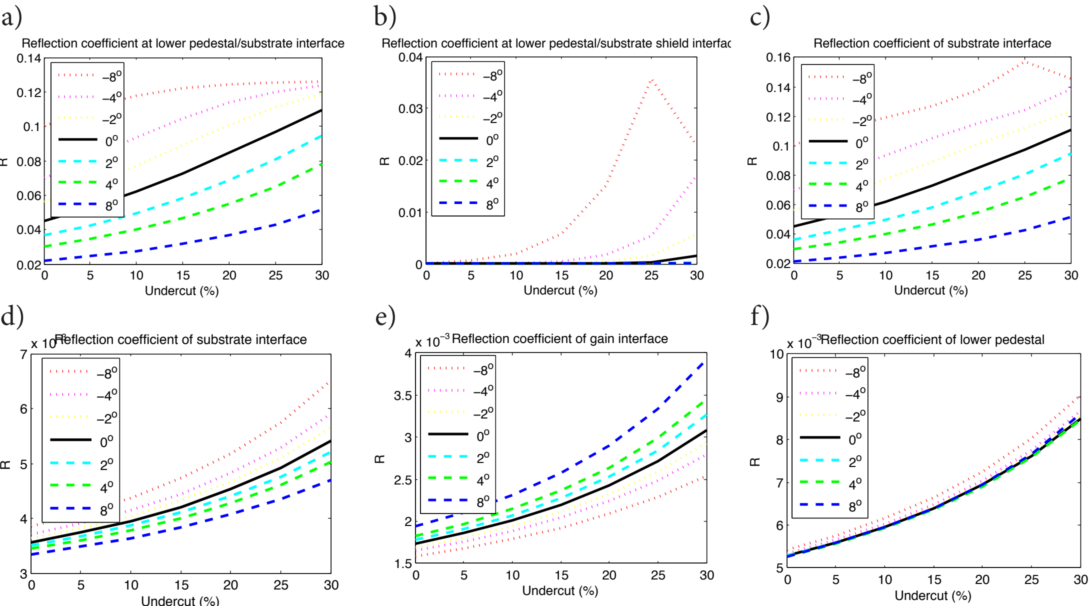

Figure 5.6: Reflection coeffient of the lower pedestal of a laser with r_{core}=225nm (a-c) or r_{core}=775nm (d-f). For the r_{core}=225nm laser, reflection coefficient is calculated for the substrate/lower pedestal semiconductor interface (a), the transition between substrate-covering and pedestal-covering shield (b), and the combined reflection coefficient of interfaces (a) and (b). For the r_{core}=775nm laser, reflection coefficient is calculated for the combined semiconductor/shield reflection at the substrate (d) and semiconductor/shield reflections at the pedestal/gain interface (e), with the combined reflection coefficient for all four interfaces shown in (f).

The pedestal sidewall angle affects performance differently depending on laser diameter and undercut amount, as seen in Fig. 5.4 (b, d, f). One effect of sidewall angle is to narrow the diameter of the laser pedestals at their top or bottom, changing the amount of effective index mismatch seen at the interfaces between substrate, pedestal,

gain, and top contact layers. Fig. 5.6 shows the calculated reflection coefficient resulting from effective index mismatch at various interfaces of the lower pedestal for lasers of r_{core}=225nm (top row) or r_{core}=775nm (bottom row). For this calculation, the laser is simulated as a 2D waveguide on either side of each interface. For the r_{core}=225nm laser, the effective index of each laser design is calculated at the frequency of the lowest-index mode, while for the r_{core}=775nm laser, a constant free-space wavelength of 1600nm is used, to make the results less dependent on our choice of gain wavelength window. For the r_{core}=775nm laser, as expected, the reflection coefficient at the lower pedestal/substrate interface is largest for negatively-angled sidewalls, for which the pedestal is narrowest next to the substrate (Fig. 5.6, d). Conversely, the reflection at the lower pedestal/gain interface is largest for positively-angled sidewalls (Fig. 5.6, e). From the combined reflection coefficient at these two interfaces, we see that the reflection at the substrate dominates slightly (Fig. 5.6, f). The reflection coefficients of the r_{core}=225nm laser are more complex, since the 2D pedestal mode is less confined and begins to interact with the cavity metal. Fig. 5.6 (a) shows the reflection coefficient at the lower pedestal/substrate interface, while (b) shows the reflection coefficient where the shield transitions between the layer covering the substrate and that covering the pedestal. At large negative sidewall angles, the mode at the pedestal bottom is poorly confined, so increasing amounts of undercut has little effect on its effective index, producing the saturation in reflection coefficient seen in Fig. 5.6 (a). However, at large negative sidewall angles, the transition in shield thickness shown in Fig. 5.6 (b) produces a large reflection, since both shield and cavity metal are in close proximity to the cavity mode. The resulting combined reflection coefficient from these two interfaces, equivalent to the plot for the r_{core}=775nm in Fig. 5.6 (d), is shown in Fig. 5.6 (c).

Due to the crystal structure of the pedestal layers, the wet etching steps that produce undercut etching are anisotropic, sometimes resulting in pedestals with square or partly square cross sections. This effect can be seen, for example, in the fabricated nanolaser in Fig. 5.3 (a). At 25% undercut, however, the effect of this square pedestal on threshold gain is minimal; an r_{core}=225nm laser with an ideal round pedestal and straight sidewalls has a threshold gain of $g_{th} = 86$ cm^{-1}, while a laser with square pedestals of the same cross-sectional area has $g_{th} = 101$ cm^{-1}. Other modes are affected more by pedestal cross-section; for the r_{core}=775nm laser, square pedestals cause the lowest-threshold mode of the 25% undercut round-pedestal laser to be replaced by another with less sensitivity

to square pedestal shape. The resulting change in laser threshold gain, an increase from 28 cm^{-1} to 197 cm^{-1}, is larger than that experienced by the r_{core}=225nm laser, but still allows for room-temperature operation.

The simulation results in Fig. 5.4 show the potential of undercut etching as a strategy for producing low-threshold nanolasers that are resistant to the effects of sidewall tilt. An undercut of 25% (measured by comparing the average diameter of the gain region and the lower pedestal region) produces a threshold gain at or below 100cm^{-1} at room temperature, low enough for room-temperature lasing. At this amount of undercut, the nanolaser performance is affected little by gain sidewall angles of 20° and plug sidewall angles of ±8°, or by error in the amount of undercut.

However, the decrease in pedestal diameter is expected to increase the Ohmic resistance of these nanolasers, potentially leading to increased laser self-heating. In Section 5.4, we perform electrical and thermal simulations of the undercut nanolasers to determine whether a 25% undercut will have detrimental effects on a nanolaser's operating temperature.

5.4 Electrical and thermal simulation

Due to their extremely small radius, Joule heating in nanolasers can be a significant contributor to nanolaser self-heating and can ultimately limit nanolaser performance, particularly for lasers with high threshold currents. The strategy of undercut etching in MCSELs has benefits in terms of optical performance and insensitivity to sidewall tilt (Section 5.3.2), but the reduction in pedestal diameter results in increased Ohmic resistance. Here, we simulate the effects of undercut etching on nanolaser resistance, total heat production, and the resulting nanolaser operating temperature at and above threshold.

5.4.1 Ohmic resistance

We calculate the Ohmic resistance of each nanolaser layer separately based on its radius, thickness, and conductivity using the standard formula for stack resistance [30]. Details of this calculation, as well as the layer doping levels and mobilities used to calculate conductivity, are given in [83]. In the total nanolaser resistance, we also include the resistance of the bottom contact layer, which behaves like a cylindrical thin film contact[33]. Although in these simulations there is no unetched InP layer above the bottom contact, in the case where the laser is not completely etched to the bottom

contact, we would use the geometry in the work by Zhang and colleagues[84]. We do not consider the wire contact resistance in these simulations; they are independent of undercut etching and the resistive heat generated is easily removed via conduction through the wires. We use straight gain and pedestal sidewalls in this calculation; extreme amounts of sidewall tilt will reduce the pedestal diameter at the top or bottom of the pedestal (depending on the direction of the tilt) and will increase the Ohmic resistance at that point, while decreasing it elsewhere. We also assume, as in the optical simulations, that the laser has an undercut ratio of 0.81; an extreme undercut ratio will increase the amount of Joule heating contributed by the upper pedestal. The resulting total Ohmic resistance, calculated for lasers of r_{core} = 225nm, 550nm, and 775nm at increasing amounts of undercut etching, is shown in Fig. 5.7.

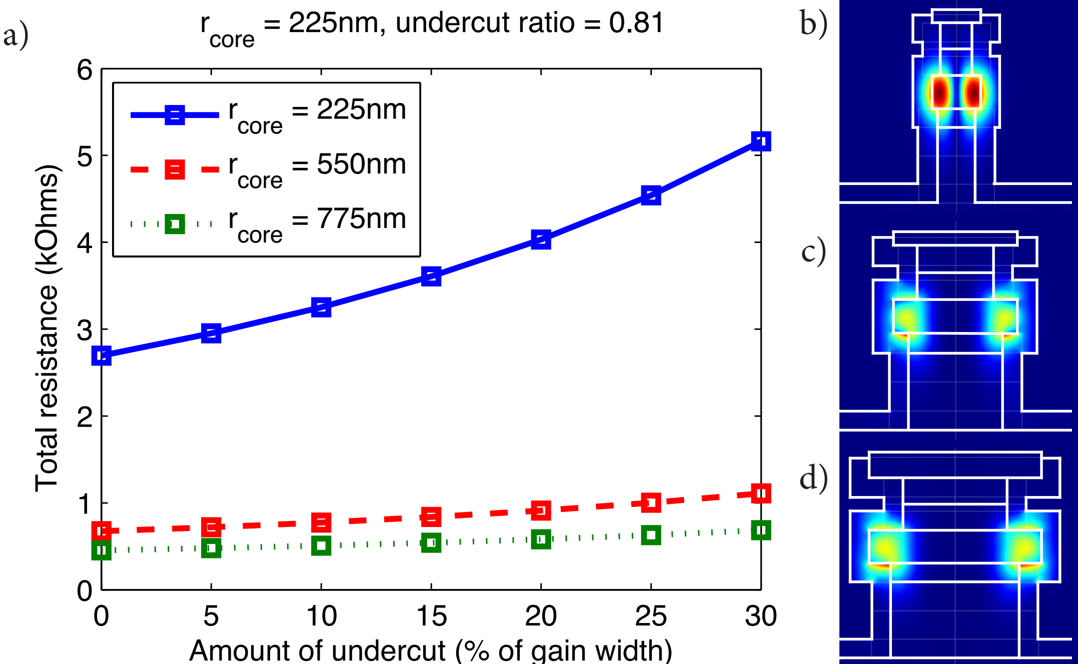

Figure 5.7: Effect of undercut etch on Ohmic resistance and electric field: (a) Total nanolaser resistance, calculated as a function of undercut for nanolasers with core radius of 225nm (blue solid line), 550nm (red dashed line), and 775nm (green dotted line). Undercut is defined as the difference between the average radius of the gain region and the lower pedestal, as a percentage of the gain radius. Here, the lasers have an undercut ratio of 0.81, meaning that the upper pedestal's radius is 81% that of the power pedestal. Resistance is the total Ohmic resistance for the entire nanolaser, including the bottom contact layer but excluding contact wire resistance. (b-d) Electric field of lowest-threshold mode for lasers with vertical sidewalls, 25% undercut, and (b) r_{core} = 225nm, (c) r_{core} = 550nm, and (d) r_{core} = 775nm.

As expected from the fact that Ohmic resistance is proportional to $1/{r_{core}}^2$, the total resistance of the $r_{core} = 225$nm laser is significantly higher than that of the larger-diameter lasers, and is more sensitive to the effects of undercut. Between 0% and 30% undercut, the resistance of the $r_{core} = 225$nm laser approximately doubles. Due to the different doping and mobilities of the different semiconductor layers, the layer that contributes the most resistive heating is the highly-doped region of the bottom pedestal, followed by the bottom contact layer. Because the bottom contact serves as a high thermal conductivity connection to the heat-conducting contact wire, the Joule heating contributed by these sources can be dissipated more effectively than heat sources located nearer to the gain region.

5.4.2 Self-heating

To calculate the final operating temperature of the nanolasers, we need to calculate not only Joule heating, but also Auger, surface recombination, junction, and heterojunction heating. Following the methods in [83], we calculate the amount of each self-heating source as a function of pump current for nanolasers of $r_{core} = 225$nm, 550nm, and 775nm. As in Section 5.4.1, we assume an undercut ratio of 0.81; in practice, this undercut ratio will vary.

With the exception of Joule heating, for every heating source calculation we simulate the laser's electrical behavior in SILVACO's ATLAS, a 2D electronic device simulator that self-consistently solves the Poisson equation, the Schrödinger equation, and the carrier transport equation, yielding the voltage drop at each point in the laser, the carrier density, and the quasi-Fermi level separation.

Auger heating is calculated as $P_A = U_A \cdot QFL$, where QFL is the quasi-Fermi level from SILVACO simulation and U_A is the Auger recombination rate. This Auger recombination rate U_A is given by $U_A = An^3V_{active}$ where A is the Auger recombination coefficient, n is the carrier density from SILVACO simulation, and V_{active} is the volume of the gain region. For A, we use $9.8 \times 10^{-29}cm^6/s$, the value given for InGaAs at 300K by [34].

We calculate surface recombination heating using $P_s = U_s \cdot V_{active} \cdot QFL$, where U_s is the rate of surface recombination in the gain region, V_{active} is the volume of the active region, and QFL is the quasi-Fermi level from SILVACO simulation. U_s is given by $U_s = \frac{n}{\tau_s}$, where n is the carrier density from SILVACO simulation, and τ_s is the

carrier lifetime, given by $\frac{1}{\tau_s} = \frac{A_{active}}{V_{active}} \upsilon_s$. Here, A_{active} is the surface area of the active region, and υ_s is the surface recombination velocity of InGaAs at 300K, calculated to be $\upsilon_s = 1.3 \times 10^4$ cm/s in [83] from values reported by Hill and colleagues[7].

The amount of self-heating at each junction is given by $P_{jn} = IV_{jn}$, where I is the pump current and V_{jn} is the voltage change at the nth junction. For operation above threshold, the heat produced at the heterojunctions (the two junctions adjacent to the gain region) is limited to the amount produced at threshold. In our calculation of device self-heating we make no assumptions about threshold current, since other experimental factors may increase threshold beyond that predicted by electrical and optical simulation. Therefore, we do not limit the heterojunction heating, which gives us a worst-case thermal performance. As the results will show, above the threshold currents for the undercut laser designs, heterojunction heating is a relatively minor contributor to total laser heating, so the heating is only slightly overestimated. We assume ideal contacts in this model; non-ideal contacts may introduce additional Schottky barrier heating (as well as Joule heating).

Fig. 5.8 shows the calculated self-heating generated in nanolasers of different core radii and undercuts, as a function of pump power. To compare self-heating behavior near and above lasing threshold, we first calculate the threshold currents enabled by each nanolaser design. For our threshold current calculations, we use the modal gain threshold from 5.3.2, compared with calculations of the material gain available at 300K[9] for the SILVACO-simulated carrier densities generated by each pump current. We compare modal threshold with the maximum material gain available at any wavelength, since each laser can be scaled in radius to match modal wavelength to gain maximum with minimum impact on modal threshold gain. This yields a threshold current of 0.6-8μA for the nanolasers with 25% and higher undercut, with the smaller-radius nanolasers having lower threshold currents thanks to the concentration of current in a smaller radius. Fig. 5.8 a, c, e) shows the range of pump currents near threshold (0-15μA), while b, d, f) shows a range of pump currents up to 500μA, far above threshold. For each type of nanolaser self-heating, we calculate heating for lasers with 0%, 25%, and 60% undercut (solid, dashed, and dotted lines).

As expected from the different dependencies of each self-heating source on pump current, the dominant self-heating sources in the near-threshold and high-current regimes will vary.

Near threshold (Fig. 5.8 a, c, e), surface recombination heating dominates, with Auger and junction/heterojunction heating gradually becoming more important as current increases. In this regime, the amount of heat generated has little dependence on the amount of undercut.

At current levels far above threshold (Fig. 5.8 b, d, f), due to the square dependence of resistive power dissipated on current, Joule heating can become more important. For the r_{core}=225nm lasers, Joule heating is significant in this regime for any amount of undercut, and a 25% undercut increases the amount of Joule heating by roughly half, compared to 0% undercut. At 60% undercut, far above that required for a low-threshold, sidewall tilt-resistant design, the generated heat is more extreme. For the larger lasers with 550nm and 775nm core radii, the increase in Joule heating with 25% undercut is slight, and the amount of Joule heat produced by even 60% undercut is less than a quarter of total nanolaser self-heating at 500μA pump current.

Because these heat sources are located in different regions of the nanolaser, their heat may be dissipated at different rates. Therefore, the operating temperature of the laser may not have a simple dependence on total heat generated. To determine the operating laser operating temperature, we performed thermal simulations using COMSOL's thermal package, using methods described in [83].

5.4.3 Operating temperature

The choice and thickness of the dielectric shield material affects a MCSEL's ability to dissipate heat through the shield into the metal cladding, as opposed to through the laser pedestals[83]. Following the optical simulation above, the shield consists of α-Al_2O_3 of 170nm thickness. The thermal conductivity of α-Al_2O_3 deposited via atomic layer deposition (ALD) depends on deposition conditions; the range reported in the literature is 1.7-20 $W \cdot m^{-1} \cdot K^{-1}$[35, 36, 37]. For our simulations of laser operating temperature, we use the most conservative value, 1.7 $W \cdot m^{-1} \cdot K^{-1}$. At this thermal conductivity we find that the shield is still a minor avenue of heat dissipation, although most heat is dissipated through the pedestal.

The calculated laser operating temperature at pump levels near threshold (a, c, e) and far above threshold (b, d, f) are shown in Fig. 5.9. As in the calculation of heat generated, for these thermal simulations we assume straight pedestal and gain sidewalls. Highly-angled pedestal sidewalls can create restrictions in the flow of heat dissipation

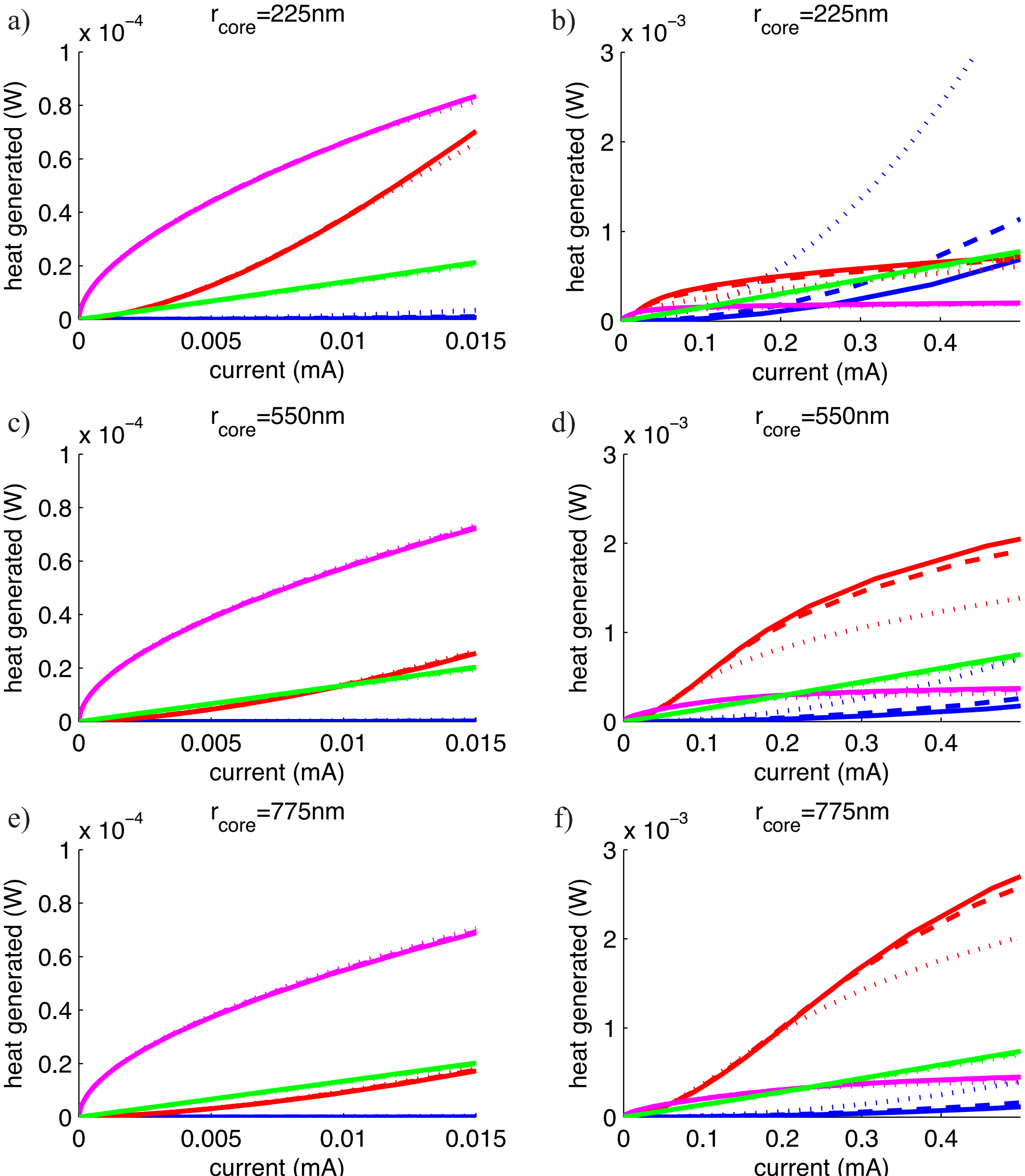

Figure 5.8: Amount of Auger (red), surface recombination (magenta), Joule (blue), and junction + heterojunction (green) self-heating as a function of pump current. Results are shown for lasers with undercut etch of 0% (solid), 25% (dashed), and 60% (dotted). a-b) Laser with r_{core}=225nm, c-d) laser with r_{core}=550nm, e-f) laser with r_{core}=775nm. Total self-heating of each type is shown for a current range near threshold (a, c, e) and well above threshold (b, d, f). The upper/lower pedestal undercut ratio used in these simulations is 0.81.

through the pedestal; for lasers with low-thermal-conductivity shields, the pedestal is the main method of heat dissipation, so this constriction could have an effect on the laser operating temperature.

Fig. 5.9 compares the steady-state operating temperatures of lasers with undercut etch of 0% (solid line), 25% (dashed line), and 60% (dotted line). In the 0-15μA regime, the temperature rise is slight, even for the smallest laser with extreme 60% undercut. In this regime, operating temperature has more dependence on undercut than heat generated (Fig. 5.8), since the smaller pedestal size of the higher-undercut lasers means a smaller conduit for heat dissipation.

At currents far above threshold, undercut has a significant effect on the r_{core} = 225nm laser operating temperature, thanks to the $1/A_{active}$ dependence of Ohmic resistance, and the I^2 dependence of Joule heating. Larger lasers are virtually unaffected by undercut, since Joule heating is only a minor source of self-heating for these lasers. The major source of self-heating for larger lasers, Auger recombination, actually decreases as undercut increases thanks to a change in QFL; however, this benefit is offset by the effects of increased Joule heating and decreased heat conduction through a narrower pedestal. Although more heat is generated in the high-current regime by the larger lasers compared to the r_{core}=225nm lasers, the large lasers have a lower operating temperature thanks to their increased ability to dissipate heat through larger pedestals.

At higher shield thermal conductivities, possible with α-Al_2O_3 or with other high thermal-conductivity dielectrics, we expect the smallest lasers to see the greatest benefit from the ability to dissipate heat through their shields, making these lasers less sensitive to the effects of undercut.

5.5 Conclusion

We examined undercut etching as a method for simultaneously decreasing nanolaser threshold and eliminating sensitivity to sidewall angle tilt in MCSELs. We first examined the effects of sidewall tilt on the threshold gain of lasers without undercut, and found that for a laser with core radius of 225nm, a 0.5° sidewall tilt approximately doubles threshold gain to above 1000 cm^{-1}, beyond the range for room-temperature operation for many common gain materials. For larger nanolasers, the effects of sidewall tilt are still severe, with threshold exceeding 1000 cm^{-1} at 2° tilt for the 550nm core laser, and at 3° tilt for the 775nm core laser.

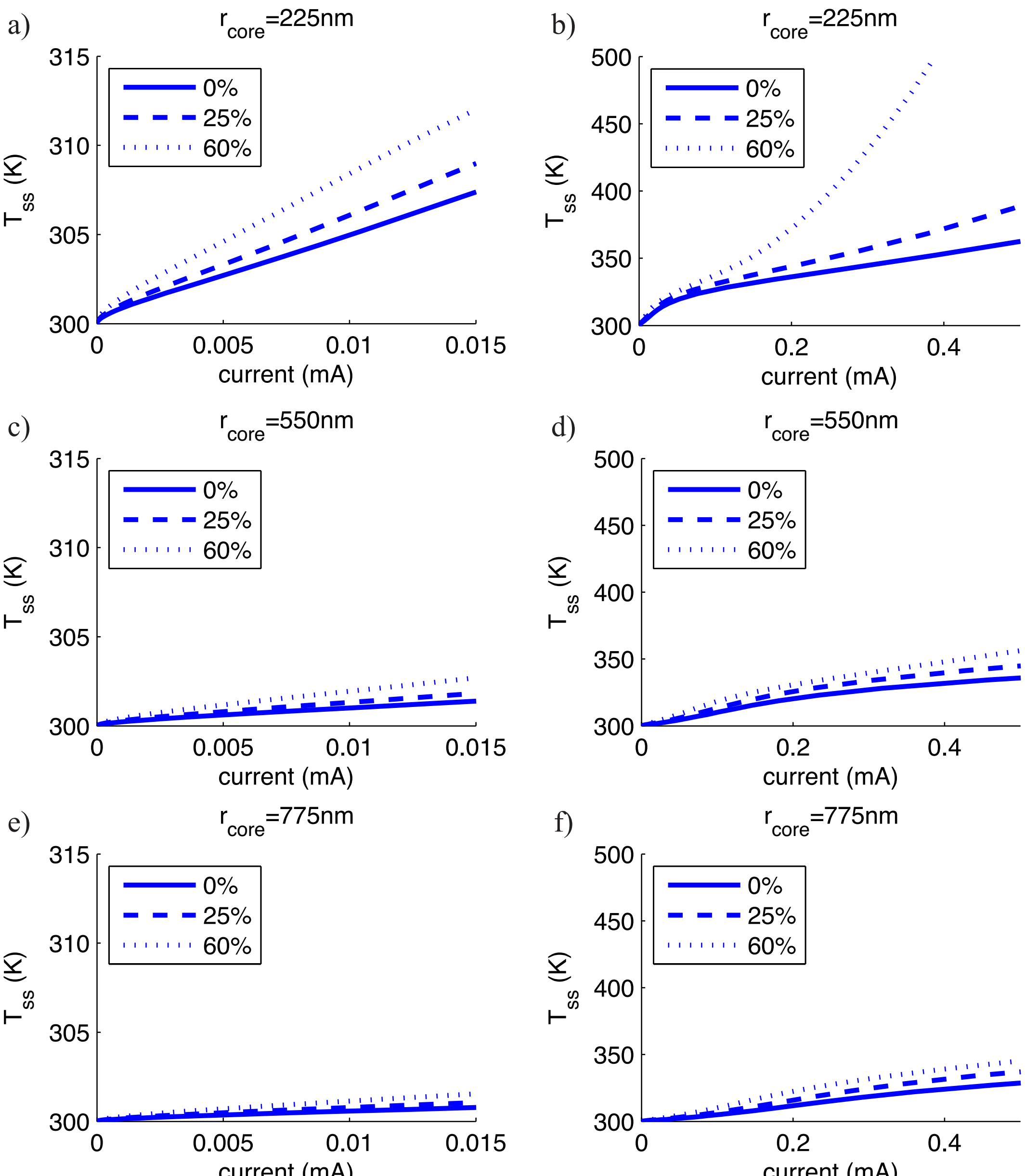

Figure 5.9: Laser steady-state operating temperature T_{ss} for a pump current range near threshold (a, c, e) and well above threshold (b, d, f), with an ambient temperature of 300K. Operating temperature is calculated for lasers with undercut etch of 0% (solid), 25% (dashed), and 60% (dotted), and an undercut raio of 0.81. Laser core radii are 225nm (a, d), 550nm (b, e), and 775nm (c, f).

Next, we simulated the effects of undercut etching on the threshold gain of nanolasers with various diameters and gain or pedestal sidewall tilts. We found that a 25% undercut etch is enough to reduce modal threshold gain to 100 cm^{-1} or lower for

lasers with core radius of 225nm, 550nm, or 775nm, even in the presence of significant sidewall tilt (20° gain sidewall, or ±8° pedestal sidewall tilt). At 25% undercut, the major limitation on cavity Q is metal absorption loss rather than radiation to the substrate; these lasers may benefit in particular from optimization of cavity metal quality[8].

To determine whether undercut etching has a significant effect on the laser's operating temperature, we used electrical and thermal simulation to determine the heat generated and operating temperature for lasers with different core radii and amounts of sidewall etch. A 25% undercut, or even an extreme 60% undercut, has no significant effect on operating temperature near our calculated threshold current of 0.6-8μA. At a current of 500μA, far above threshold, a 25% undercut has little or no effect on operating temperature for a laser with core radius of 550nm or 775nm. The smallest nanolaser considered, with core radius of 225nm, shows little temperature rise at 25% undercut up to a current of 200μA.

We note that the amount of gain and pedestal sidewall tilt that can be tolerated is limited, even for undercut nanolasers. Large sidewall angles may constrict the pedestal enough that the laser becomes mechanically unstable, prone to toppling during fabrication. In addition, these constrictions may produce high localized Ohmic resistance, carrying a larger self-heating penalty than the straight-sidewall lasers we considered in our thermal simulations. Finally, for lasers with small radius and long pedestals, large sidewall tilts would in theory cause the top of the pedestal to protrude beyond the edges of the gain region - although this situation would not be realizable using our current fabrication procedure, we included these geometries in our simulation for the sake of completeness.

Our simulations show the promise of undercut etching as a strategy for reducing threshold gain in MCSELs and compensating for the effects of sidewall tilt, with little or no thermal penalty. This strategy produces a nanolaser design with increased robustness, and with a low threshold gain that allows efficient use of pump current. In addition, these nanolasers can operate well above threshold with minimal self-heating. Our simulations used a conservative estimate for the shield thermal conductivity; a higher-conductivity dielectric shield would allow for increased heat dissipation through the shield, further increasing the potential of these nanolasers for high-power operation. Fabrication of these nanolaser designs is currently in progress.

5.6 Acknowledgements

This chapter, in full, is a reprint of material recently submitted for publication by Janelle Shane, Qing Gu, Alan, Potterton, and Yeshaiahu Fainman. The dissertation author was the primary author of this paper, and performed most of the simulations and data analysis. Qing Gu fabricated the lasers shown in Fig. 5.3, and took the SEM images for this figure. Alan Potterton performed the simulations of square vs round pedestal described in Section 5.3.2.

Chapter 6

Effect of dielectric shield material choice on metal-clad nanolaser optical and thermal performance

6.1 Introduction

As metal-clad nanolasers move toward higher output powers, the ability to manage heat becomes ever more critical. The choice of shield material can affect a nanolaser's ability to dissipate heat via conduction to the metal cladding, and a move toward shield materials with higher thermal conductivity may greatly increase the potential for operating safely at higher pump currents.

A typical electrically-pumped metal-clad nanolaser consists of a semiconductor gain core of radius r_{core} with doped semiconductor layers on either side to form the connection between top and bottom contact (Fig. 6.1). A metal cladding of thickness $t_{cladding}$ surrounds the entire laser, with a dielectric shield layer of thickness t_{shield} providing electrical isolation between top and bottom contact. For lasers operating using photonic modes (rather than plasmonic modes, which require high modal overlap with metal), some researchers have used a thicker dielectric layer to increase the optical isolation between the mode and the metal, reducing loss in the metal[21, 20, 19, 85].

However, some researchers have noted that the low thermal conductivity of dielectrics such as silicon nitride (SiNx) may cause problems with heat buildup, impacting laser performance[85, 19]. Not only does a higher operating temperature impact gain

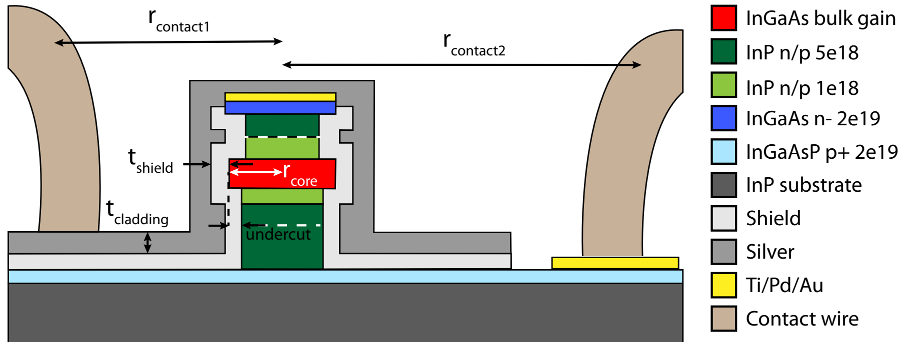

Figure 6.1: Diagram of an example metal-clad nanolaser with r_{core}=550nm and 25% undercut etching. In optical simulation, the area surrounding the metal cladding is also metal, due to the thin skin depth of optical mode in metal. In thermal simulation, the metal cladding is surrounded by air, and the laser is allowed to lose heat through conduction to the nearest contact wire, as well as conduction through the bottom of the substrate.

performance and increase metal loss, but the mechanical integrity of the laser may be impacted as well, due to thermally-induced stresses within and between materials. One strategy of enhancing heat dissipation is by using a thinner shield than that which would be optically optimum, which has the advantage of also reducing potential damage to the gain material during shield deposition[8, 19], at the expense of increased metal loss. Another strategy is to use shield materials with higher thermal conductivity; Gu and coworkers used amorphous aluminum oxide (α-Al_2O_3) as a shield material and presented simulations showing the thermal advantage of α-Al_2O_3 over more commonly-used silicon dioxide (SiO_2)[23]. However, due to the higher refractive index of α-Al_2O_3 compared to SiO_2, the laser's optical performance may have been less than it would have been with SiO_2.

Here, we simulate the optical and thermal performance of two commonly-used dielectric shield materials, SiO_2 and SiN_x, and two higher-conductivity shield materials, α-Al_2O_3 and aluminum nitride (AlN). We begin in Section 6.2 by looking at threshold gain (g_{th}) as a function of shield thickness for each of the four shield materials, for a nanolaser with r_{core}= 225nm or 775nm. Unlike the shield thickness investigation in [21], we look at the behavior of a laser whose upper and lower pedestals have been undercut by 25% compared to r_{core} (Fig. 6.1), which was found to be optimum for reducing threshold gain and increasing tolerance of sidewall tilt[86]. We also consider a design for which only r_{core} is fixed, with the total device radius allowed to increase as shield thickness

increases.

Next, in Section 6.3, we examine the effect of shield material on the operating temperature (maximum steady-state temperature in the gain region) and temperature distribution in nanolasers of r_{core}=225nm. We look at shields at their optimum optical thickness, as well as at thicknesses that are thin enough to increase thermal conductivity of the layer.

6.2 Optical simulation

To determine the effect of shield material choice on a lasers's optical performance, we used COMSOL's 3D finite element mode solver to simulate lasers of r_{core}=225nm or 775nm, with varying shield material and thickness t_{shield}. The refractive indexes used in simulation are found in Table 6.1; SiO_2 has the lowest refractive index at 1.4491, while AlN has the highest at 2.189. All simulations are performed using materials parameters at an ambient temperature of 300K, with the silver cladding using ϵ_r = -130.6-3.33j, as calculated by Smalley and colleagues[9] using a temperature-dependent Drude model and data from Johnson and Christy [71]. Refractive index of a material, as well as its other material parameters, depends on the deposition method; here, we use values either measured from materials deposited in our own fabrication facility, or literature values whose conditions match ours as nearly as possible. The semiconductor layer stack is the same as used in [7] and whose material parameters are tabulated in [83].

Each nanolaser has a lower pedestal with 25% undercut, defined here as the difference between r_{core} and pedestal radius, as a percentage of r_{core}. Due to the difference in etching rates for the upper and lower pedestal materials, the upper pedestal usually has a larger undercut than the lower pedestal. In our simulations, we use an experimentally-measured ratio of upper to lower pedestal radius of 0.81; in practice, this ratio will vary. In [86], 25% undercut was shown to produce a g_{th} of 100cm^{-1} or less for a nanolaser with α-Al_2O_3 shield of thickness 170nm and r_{core}=225, 550, or 775nm, regardless of sidewall angle, with minimal thermal penalty near threshold. The lasers in this current study are simulated to have straight sidewalls. As in [83] and [23], we assume that the semiconductor pillar is etched all the way down to the bottom contact layer. We search for modes with λ_0 in the range 1400-1750nm, which matches the available room-temperature material gain at a moderate carrier density of N=5$\times$10^{18} cm^{-3} for our gain material. According to our electrical simulations described in Section 6.3 below, this

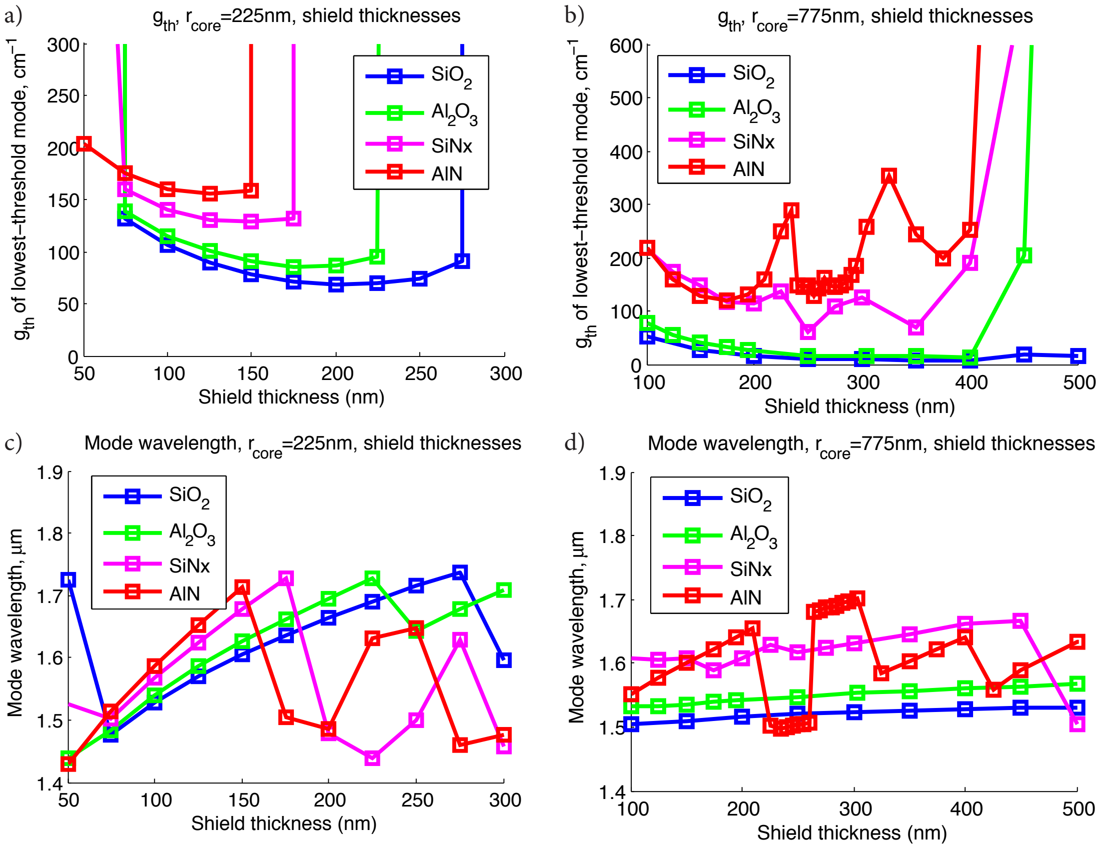

Figure 6.2: Simulated threshold gain (a, b) and mode wavelength (c, d) for nanolasers with 25% undercut and different dielectric shield materials. Shield materials are SiO_2 (blue line), α-Al_2O_3 (green line), SiN_x (magenta line), and AlN (red line). Nanolaser gain core radius is 225nm (a, c) or 775nm (b, d).

carrier density is achieved for the r_{core}=225nm 25% undercut laser at a theoretical pump current of 19μA. Calculated g_{th} for the lowest threshold mode of each laser are shown in Fig. 6.2 (a, b), with the free-space wavelength of the modes shown in Fig. 6.2 (c, d).

From Fig. 6.2 (a) it is evident that each shield has a different optimum optical thickness, with shields of lower refractive index having both a lower optimum g_{th} and a larger optimum t_{shield}. Sudden changes in g_{th} are caused when the wavelength of the lowest-g_{th} mode shifts enough that the mode leaves the gain window (Fig. 6.2 (c)). Because the optical mode overlaps more with shields of higher refractive index, the wavelength in lasers with these shields is more sensitive to shield thickness. For the r_{core} = 225nm laser, the TE_{01} mode is the only well-confined mode near the gain window, so g_{th} is only low while this mode is in range. For the r_{core} = 775nm laser (6.2 (b, d)),

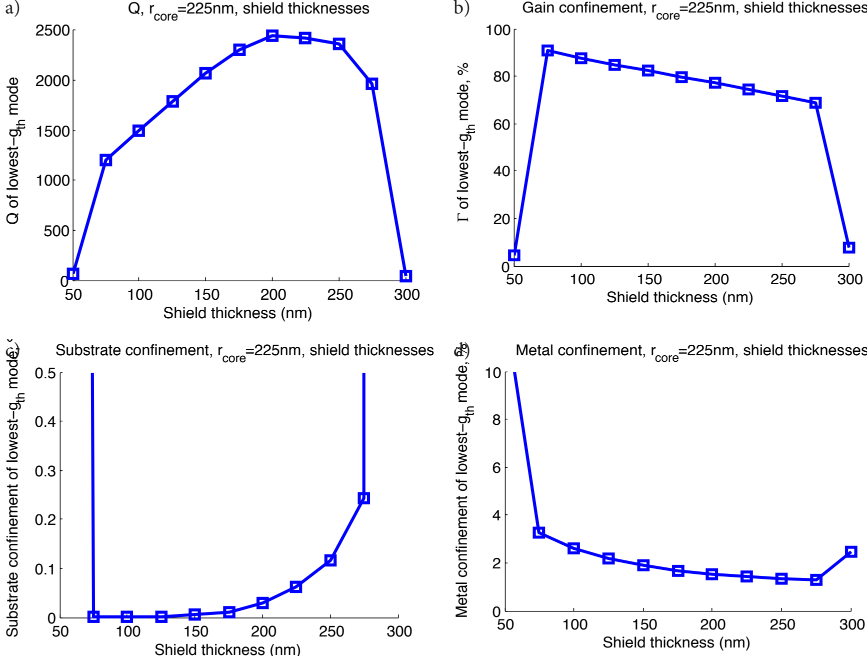

Figure 6.3: Behavior of laser with r_{core}=225nm and SiO_2 shield of thickness 50nm - 300nm. Parameters plotted are (a) threshold gain, (b) mode confinement Γ, (c) substrate confinement, and (d) metal confinement.

there are many more modes in the gain window, so the lowest-threshold mode changes frequently, producing discontinuities in g_{th} and λ_0, particularly for shields with higher refractive index (see discussion of Fig. 6.4 below).

Fig. 6.3 shows the interplay of factors leading to a g_{th} minimum for a single mode, using the example of an r_{core}=225nm laser with SiO_2 shield. The TE_{01} mode is the lowest-threshold mode for the range of shield thicknesses down to 75nm, and has an optimum in g_{th} for t_{shield} = 200nm (Fig. 6.3 (a)). At thin t_{shield}, modal overlap with metal increases (d), while at thicker t_{shield}, gain confinement (b) decreases due to increased radiation to the substrate (c). Below 75nm shield thickness and above 275nm thickness, the TE_{01} mode leaves the gain window, and the mode that takes its place as the lowest-threshold mode has much worse performance. For shields with higher refractive index, the same factors determine the optimum g_{th} point, with the g_{th} more sensitive to changes in t_{shield}.

To evaluate the optical performance of the strategy of using lasers with shields much thinner than the optical optimum[19, 8], we examine the performance of the r_{core} =

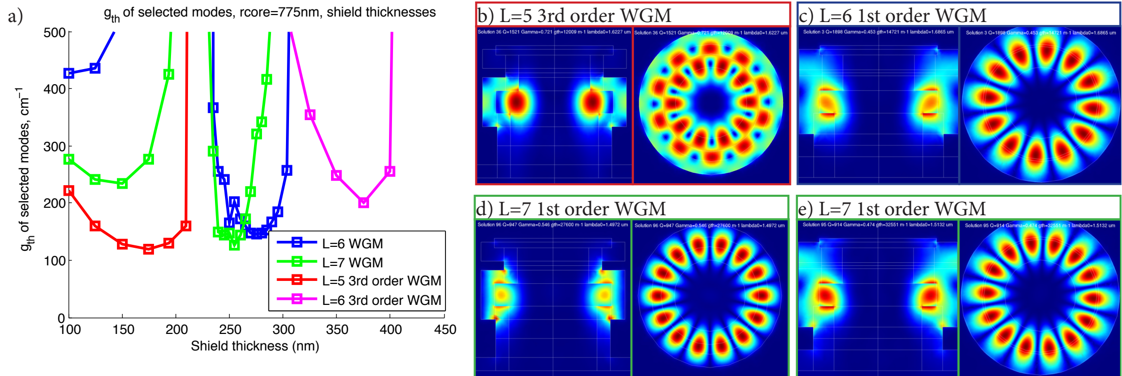

Figure 6.4: (a) g_{th} of lowest-threshold modes for r_{core}=225nm laser with AlN shield. (b-e) Normalized electric field of selected modes, viewed as side view (left) and top view (right). Modes are (b, red) L=5 3rd-order WGM at t_{shield}=175nm, (c, blue) L=6 1st-order WGM at t_{shield}=275nm, (d, green) L=7 1st-order WGM at t_{shield}=175nm, and (e, green) L=7 1st-order WGM at t_{shield}=275nm.

225nm laser with a SiNx shield of 25nm thickness. For this design, the lowest-threshold mode has a free-space wavelength of λ_0=1517nm, a threshold gain of g_{th}=783cm^{-1}, a Q of 261, and a confinement factor of 0.69. Although this threshold gain is achievable at room temperature for many gain materials, it is 5x higher than that of a laser with an AlN shield of optical optimum thickness.

Fig. 6.4 shows the g_{th} minima of the lowest-threshold modes of the r_{core}=775nm laser with AlN shield, a higher-resolution view of the t_{shield} range from Fig. 6.2 (b). The two 1st-order whispering gallery modes (WGM) have two minima visible, one on either side of t_{shield} = 265nm, where the shields covering the top contact and gain region meet. For this shield material and r_{core}, then, there exist values of t_{shield} for which the lasing mode is very sensitive to t_{shield} and to the shape of the shield exterior. Lasers using higher-index shields will need to be designed carefully to avoid values of t_{shield} for which no mode has a g_{th} minimum. On the other hand, lasers could be designed to take advantage of this sensitivity for wavelength switching.

Results of these optical simulations are summarized in Table 6.1, which lists the optimum shield thicknesses found for each shield material and laser diameter, with the exact minimum g_{th} and optimum t_{shield} limited by the number of shield thicknesses evaluated in simulation. The higher-index shields have the disadvantage of a higher g_{th} at any given shield thickness, but the advantage of requiring thinner shields, leading to smaller overall device size and to potentially less damage to the gain material during

shield deposition. In the next section, we explore the thermal performance of lasers with these shield materials.

6.3 Thermal simulation

Self-heating in electrically-pumped nanolasers is generated by surface and Auger recombination, Joule heating, junction heating, and heterojunction heating[83, 29]. Due to their different dependencies on pump current, each of these heating mechanisms may be dominant at different currents, so the location of the heating sources will change, potentially affecting the laser's ability to dissipate heat. The avenues for heat dissipation are conduction through the bottom of the 350μm thick InP substrate, conduction through the metal cladding to the top contact wire at a distance $r_{contact1}$=20μm away, and radiation through the metal cladding. Due to the higher thermal conductivity of the InGaAsP bottom contact material compared to that of the InP substrate, conduction to the top contact wire becomes the dominant heat dissipation mechanism.

Fig. 6.5 shows the heat generated by an r_{core}=225nm laser with 25% undercut and a ratio of upper to lower pedestal diameter of 0.81, as in the optical simulations above. Heat production is shown for a pump current of (a) 1μA, (b) 250 μA, and (c) 1mA, simulated with the help of SILVACO'S ATLAS using the methods described in [83]. We assume ideal contacts in this model; non-ideal contacts will contribute additional Joule and Schottky barrier heating at the interface between top contact and metal.

At 1μA current (a), approximately our calculated threshold current for a laser with r_{core}=225nm, 25% undercut, straight sidewalls, and 170nm α-Al_2O_3 shield, the dominant heat source is surface recombination in the gain region. By 250μA current (b), both Joule heating and junction heating become nearly as important as surface and Auger heating, so the generated heat becomes more distributed along the laser pedestal, making this heat easier to dissipate through top and bottom contact. At 1mA current (c), the dominant source of self-heating is Joule heating in the low-conductivity lightly-doped layer beneath the gain region, so the generated heat has to either dissipate through the shield, or travel nearly half the height of the laser to leave through the bottom contact. At very high currents, therefore, the ability to dissipate heat through the shield becomes more helpful.

Next, we used COMSOL's heat conduction module to simulate the steady-state temperature inside the laser at a range of pump currents. Fig. 6.6 shows the temperature

Table 6.1: Material parameters used in optical and thermal simulations, along with the optimum optical shield thicknesses found for each material and laser diameter. All values reported are for a temperature of 300K. The refractive indexes given for ALD α-$Al_2O_3$was measured at 633nm from a film deposited in our cleanroom.

material	n	k, W/(m*K)	ρ, kg/(m^3)	C_p, J/(kg*K)	optimum shield thickness (nm)	
					r_{core}=225nm	r_{core}=775nm
PECVD SiO_2	1.46[87]	1.1 [38]	2200 [43]	235 [41]	200	400
ALD α-Al_2O_3	1.64	1.7-20 [35, 36, 37]	3690 [37]	880 [37]	175	304
SiNx	1.99[87]	0.7[60]	2200[60]	370[88]	150	250
AlN	2.189 [39]	320 [89]	2500 [89]	710 [90]	125	175

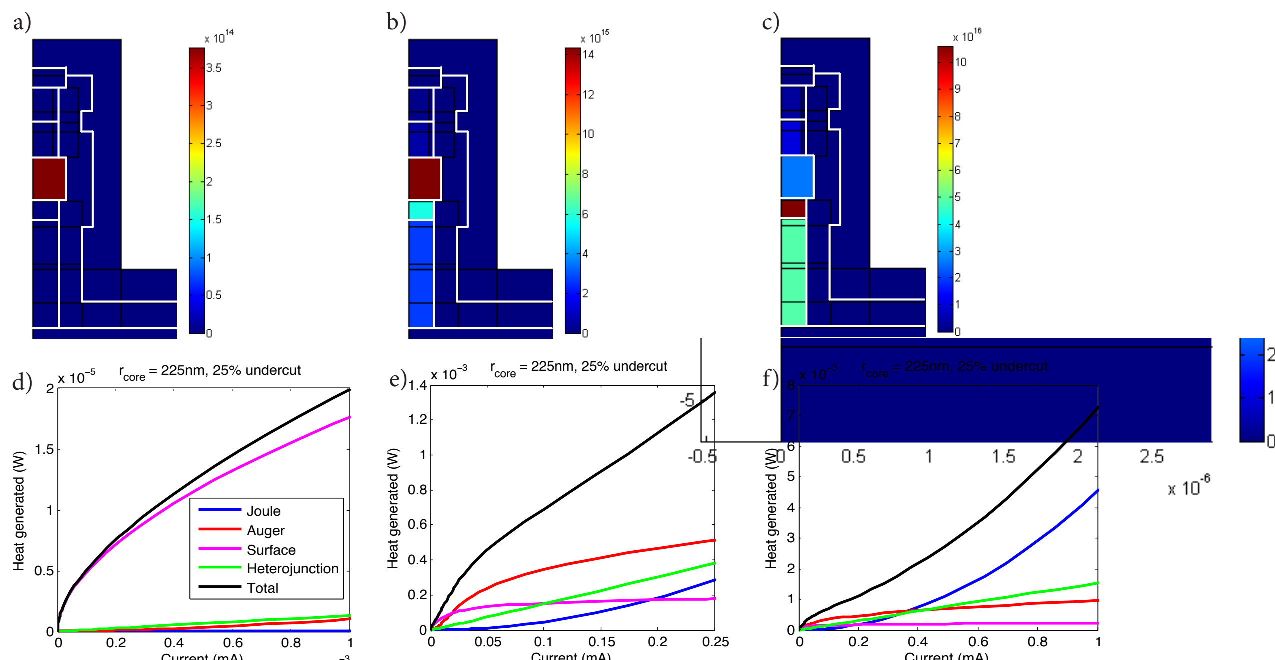

Figure 6.5: Amount and locations of heat sources for an r_{core}=225nm laser, at a pump current of (a, d) 1μA, (b, e) 250 μA, and (c, f) 1mA. Top row shows the locations of the heating sources, normalized to the maximum heat produced by the laser at that current, in W/m^3. Bottom row shows the contributions of each heating source type: Joule heating (blue), Auger recombination (red), surface recombination (magenta), junction + heterojunction heating (green), and total heat generated (black).

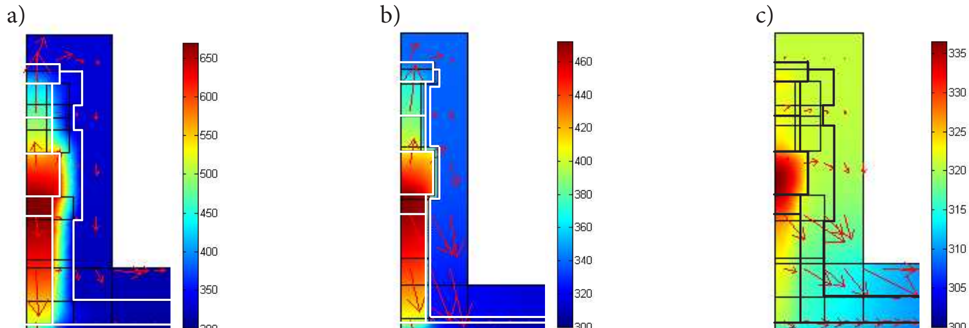

Figure 6.6: Steady-state temperature distribution at 1mA pump current in an r_{core}=225nm nanolaser with a shield consisting of (a) 150nm SiNx (optical optimum), (b) 25nm SiNx (average of thicknesses used in [68, 19]), and (c) 125nm AlN (optical optimum). Each image is normalized to the maximum temperature; for (a), the maximum temperature is 670K; for (b), the maximum temperature is 472K; for (c), the maximum temperature is 339K. Arrows indicate the direction and magnitude of heat flux.

distribution at 1mA pump current in a laser with r_{core} = 225nm, 25% undercut, and a shield consisting of (a) 150nm SiNx (optical optimum), (b) 25nm SiNx (average of thicknesses used in [68, 19]), and (c) 125nm AlN (optical optimum). The laser with the optically-optimum 150nm SiNx shield, the lowest thermal conductivity among the shields examined here, has an operating temperature of 670K, with most heat dissipated through the top and bottom pedestal of the laser. At 25nm thick, the SiNx shield is thin enough to dissipate some heat, and the laser operating temperature drops to 472K. The temperature gradient across the shield layer increases from about 2K/nm to 6K/nm. A laser with an optically-optimum AlN shield thickness (125nm) dissipates its heat primarily through the shield, and has an operating temperature of 336K. Because the AlN shield has higher thermal conductivity than the pedestal, the temperature gradient lies across the laser pedestal layers, rather than the shield.

Finally, in Figure 6.7 we plot the steady-state operating temperature T_{ss}, which we define as the maximum temperature in the laser, for an r_{core} = 225nm laser with 25% undercut. For the SiNx, SiO_2, α-Al_2O_3, and AlN curves shown with solid purple, blue, green, and red lines, respectively, the shield thickness used is the optical optimum thickness listed in Table 6.1. For the α-Al_2O_3 shield, the thermal conductivity varies depending on deposition conditions (Table 6.1), so we calculate T_{ss} using two reported shield thermal conductivity values from the literature, 20 W/(m*K) (green dashed line) and 10 W/(m*K) (green solid line). We also calculate the operating temperature of a

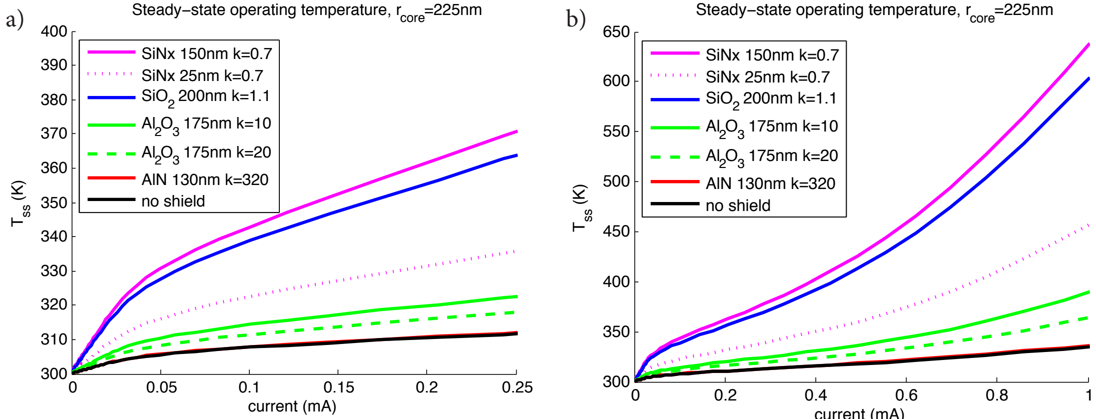

Figure 6.7: Maximum steady-state temperature of the gain region for an r_{core} =225nm laser with shield thickness set at the optically maximum thickness for each shield material (solid and dashed lines). Purple, blue, green, and red lines correspond to SiNx, SiO_2, α-Al_2O_3, and AlN, respectively. Results for the laser with α-Al_2O_3 shield are shown for a thermal conductivity of 10 W/(m*K), solid green line, and for 20 W/(m*K), dashed green line. Also plotted are steady-state temperatures for the laser with no shield (solid black line) and a 25nm shield of SiNx (purple dotted line). Two current ranges are shown, (a) up to 250μA, and (b) up to 1mA

laser with a 25 nm shield of SiNx (purple dotted line). For comparison we include a simulation with no dielectric shield (black line).

The optically optimum thicknesses of these shield materials are all comparable (125nm - 200nm), so at this thickness, the shield's thermal conductivity has the strongest effect on its thermal performance. By 0.5-1mA pump current, typical for an experimentally-demonstrated room-temperature electrically-pumped wavelength-scale nanolaser[22, 19, 23], the difference in operating temperatures is significant. Lasers with SiNx and SiO_2 shields of optically-optimum thicknesses have operating temperatures of around 600K at 1mA pump current, while a laser with an AlN shield has an operating temperature of 339K, a performance nearly identical to that of a laser with no dielectric shield (337K operating temperature). Reducing the thickness of the SiNx to 25nm yields a significant improvement in thermal performance, although the performance is not as good as that of α-Al_2O_3 or AlN, and comes at the expense of increased threshold gain.

6.4 Conclusion

We examined the optical and thermal performance of different dielectric materials as shield layers in metal-clad photonic-mode nanolasers. Each mode has an optimum optical thickness for a given shield material, with the optimal thicknesses for lasers with lower refractive index occurring at longer wavelength and producing lower threshold gains. A shield's thermal performance depends more strongly on its thermal conductivity than on the optimal thickness determined by its refractive index. Reducing a shield's thickness to well below its optical optimum significantly improves thermal performance, at the expense of greatly increased threshold gain.

The results here indicate that differing strategies may be of use, depending on whether laser is intended to operate near threshold or well above it. For lasers designed to operate near threshold, a low-index shield such as SiO_2 may be the best choice, since the high index contrast between shield and semiconductor produces a low threshold gain. For lasers designed for higher output powers, or with high threshold currents caused by other factors such as material damage, operation at currents far above threshold may cause significant heat production, and a high-conductivity shield has a clear advantage. At 1mA current, AlN performs better than a 25nm shield of SiNx, and nearly as well as a laser with no dielectric shield at all. In addition, the temperature gradient of a laser with AlN shield is much less extreme than in a laser with a low-conductivity shield such as SiNx, and occurs in the semiconductor pedestal rather than across the shield layer, which may reduce stress on the materials.

The simulations here were performed assuming an undercut of 25% on both upper and lower pedestals. For higher undercut amounts, or for cases where one of the pedestals is etched more than the other, the importance of shield thermal conductivity will increase as the heat dissipation pathway through the pedestals shrinks, and as the amount of Joule heating increases. Optically, the amount of undercut etch, as well as non-vertical gain and pedestal sidewall angles, will likely affect the optimum shield thickness.

For all of these lasers, the metal cladding was assumed to have a thickness of $t_{cladding}$ = 200nm. Due to the directionality of the sputtering method for depositing metal cladding, lasers with undercut etching may have restrictions in this cladding that reduces the efficiency of heat conduction. This effect will be most important for a shield with moderate conductivity, since a laser with low-conductivity shield dissipates heat through its pedestal rather than through the laser's cladding, and a laser with high-

conductivity shield can bypass the constriction by routing heat through the shield.

The analysis here shows that AlN is the best shield choice for lasers operating at high currents, whether for higher output power or because of fabrication imperfections that increase threshold current. However, other considerations not explored here may also be important in the choice of shield material and thickness, such as damage to the semiconductor layers during deposition of a thick shield, or performance as a passivation layer. Changes in fabrication technique may enable higher thermal conductivity in a shield with low refractive index, and improved heat sink design, such as the use of a substrate with higher thermal conductivity, may enable better thermal performance in lasers with low-conductivity shields. As metal-clad nanolasers move toward integration with silicon, they may benefit from many of the techniques that have enabled better thermal performance in VCSELS and larger lasers.

6.5 Acknowledgements

All simulations and analysis in this chapter were performed by Janelle Shane. Dr. Qing Gu and Mr. Dor Gabay are acknowledged for helpful discussions.

Chapter 7

Conclusion and future work

7.1 Conclusion

The work in this dissertation represented a detailed simulation-based investigation into the performance of realistic metal-clad semiconductor nanolasers. The insights drawn from these simulations led to explanations of the behavior of recently-fabricated nanolasers, as well as to design changes that should greatly improve nanolaser performance and robustness.

Chapters 2 and 3 outlined some of the tools used in this thesis, optical and thermal simulations at a level of detail not previously used in metal-clad nanolaser research. In Chapter 4, these tools were applied to a recently-fabricated laser whose performance had been poor. Simulations revealed that the poor performance of the laser was not due to self-heating, as had been previously assumed, but to a non-ideal cavity shape, with slanted sidewalls producing poor gain confinement. This slight but critical deviation from design would not have been revealed by the straight-walled simulations typically performed for nanolasers. An increase in the amount of undercut was found to improve the performance, producing a design that should allow lasing at room temperature.

Chapter 5 further explored the interplay of sidewall angle and undercut etching. Optical simulations showed that although just an 0.5° sidewall angle can dramatically raise a nanolaser's threshold gain to 1000 cm^{-1}, a 25% undercut makes nanolasers very resistant to sidewall tilt. Nanolasers with 25% undercut had threshold gains below 100 cm^{-1} for gain and pedestal sidewall angles over the entire range seen in fabrication (up to 20° for gain and ±8° for pedestals). Because undercut etching involves narrowing the

pedestals through which the pump current flows, thermal simulations were needed to verify that the additional self-heating introduced by undercutting would not prove too detrimental. Near threshold currents, the additional self-heating proved to be negligible, but at higher currents, the smallest lasers heated significantly. To allow operation at higher currents, even for non-undercut lasers, some method of heat management is required. One method of heat management is by choosing dielectric shields with high enough thermal conductivity to allow heat dissipation through the shield into the cladding.

Chapter 6 looks at the optical and thermal performance of four different dielectric shield materials, two of which are commonly used in nanolasers, one of which was demonstrated for the first time in the work reprinted in Chapter 4, and one of which has not yet been demonstrated in nanolasers. The lowest-index shields have the largest optically optimum thicknesses and the best optical performance. The difference in thermal performance among shield materials is large, with the two lowest-conductivity shields heating by 300K at 1mA current, while the highest-conductivity shield, AlN, heats only by 37K, nearly identical performance to the case with no shield at all. Although the AlN shield has the highest refractive index, and therefore the largest threshold gain, at 25% undercut its optical performance is good enough to achieve room-temperature lasing for the bulk InGaAs gain material used in our studies. AlN, therefore, is an excellent shield candidate for future generations of metal-clad nanolasers with high output powers.

The discussion below identifies areas of ongoing and future investigation, in directions that should yield further improvements in our simulations.

7.2 Identification of additional factors affecting nanolaser performance

7.2.1 Pedestal shape

Fabricated lasers show a great variation in the shape of the lower pedestal. Chapter 5 investigated the effect of the sidewall angle of pedestals with cone-shaped sidewalls. However, pedestal sidewalls frequently have sidewalls whose slope changes, and the effects of these changes on optical behavior are currently not well understood. For example, the nanolaser whose SEM image is shown in Fig. 7.2 was simulated to have a threshold gain of 105 cm^{-1}, although according to the definition of undercut in Chapter 5 it had no undercut and should therefore have had a high threshold gain.

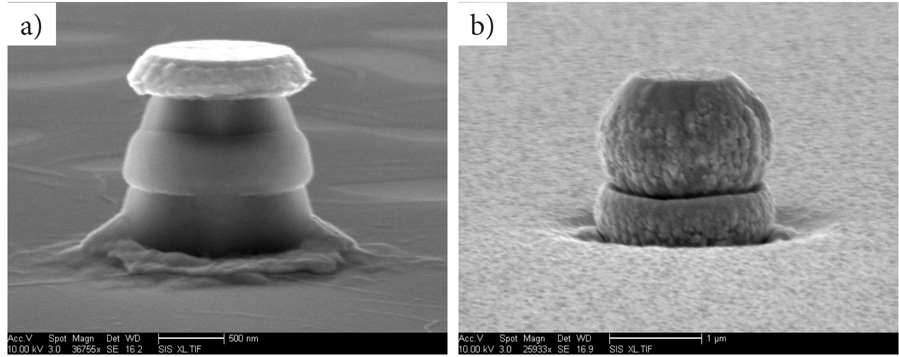

Figure 7.1: An electrically pumped nanolaser before (a) and after (b) deposition of metal cladding. Scale bar on (a) is 500nm, while scale bar on (b) is 1000nm.

A more detailed piecewise investigation of pedestal sidewalls, for example using an analysis based on waveguide cutoff[21], may reveal the effects of changing sidewall slope, or the effects of positively versus negatively-sloped pedestal sidewalls.

7.2.2 Cladding shape and thickness

The thickness of the metal cladding surrounding the laser affects the laser's ability to dissipate heat, for lasers with thermally-conductive shields. When the cladding becomes too thick, it prevents the liftoff step from forming the metal contacts. A study of nanolaser operating temperature vs cladding thickness may reveal a thickness beyond which minimal thermal benefit is seen. This thickness may depend on the size, positioning, and thermal conductivity of the electrical contact wires, which currently provide the most important avenue for heat dissipation. The circularly-symmetric thermal simulations in this dissertation may need to be altered to account for cases where the path to the contact wire, rather than exit from the laser, is the primary source of thermal resistance.

Another important consideration may be the shape of the metal cladding. Because the sputtering method used to deposit this metal is directional, a highly-undercut laser may have areas where the metal cladding is thin, or where air gaps are created (see example SEM images in Fig. 7.2). These may affect the laser's electrical, thermal, and optical behavior.

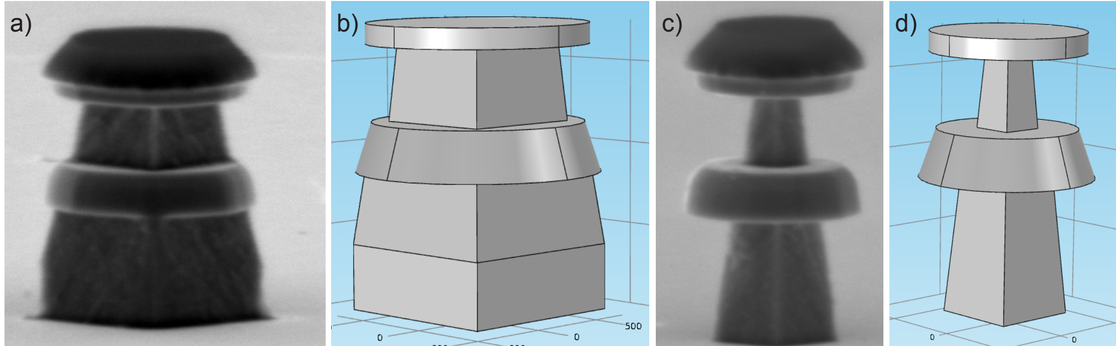

Figure 7.2: SEM images (a, c) and COMSOL model geometries (b, d) of two fabricated lasers, shown without dielectric shield or metal cladding. Both worked only at cryogenic temperatures and had threshold currents of 1mA or more, but in optical/electrical simulation had thresholds of only 10μA for room temperature operation. All lasers are shown without shields.

7.2.3 Detailed simulation of fabricated lasers

Comparing simulated lasers with their laboratory performance may reveal additional effects that are currently unaccounted for in simulation. For example, two recently-fabricated nanolasers with significant undercut etching and thermally-conductive shields were found to perform poorly, failing to lase above 77K, and requiring high threshold currents (1-3mA). Both lasers, shown in Fig. 7.2, were optically simulated, including sidewall angles and square pedestal shapes, and were found to have threshold gains of 105 cm^{-1} (a) and 80 cm^{-1} (c, d) for room-temperature operation, corresponding to threshold currents of only about 10μA. These lasers displayed no obvious problems such as badly-formed contacts or high leakage currents (which would indicate a short circuit or other current path in parallel with the laser). The lasers have diameters of 750nm (a, b) and 550nm (c, d), which, in combination with their use of a thermally-conductive α-Al_2O_3 dielectric shield layer, should ensure little to no temperature rise (see results in Chapters 5 and 6). The addition of new simulation aspects, such as the effects of thermally-induced strain, non-ideal contacts, defects at material interfaces, material damage, or the effects of surface passivation on surface recombination, could help illuminate the reason for failure, and point the way toward new improvements.

7.3 Closed-loop multidomain simulation

The simulations in this dissertation are partially integrated with one another, with information from electrical and material simulations used as inputs to thermal simulations, which then set the material parameters for optical simulation. However, a closed-loop simulation would allow more complex feedback mechanisms to be investigated. Similar work has been undertaken for VCSELS[29].

One of the main mechanisms for feedback is through changing material parameters. These may be affected by changing temperatures and carrier densities, parameters that are often time-dependent and position-dependent.

Some of the work in this dissertation already accounts for the effects of changing temperature on metal loss and material gain availability (see Chapter 3 and Chapter 4 for examples). Temperature also has a minor effect on refractive index, which can have an effect on the number and wavelength of cavity modes[9]. In addition, thermal material parameters are also temperature-dependent, a dependency that was not explored in this dissertation due to the lack of available experimental data for many materials used in these nanolasers. The ability to close the loop thermally will depend on the ability to measure these parameters, or to extrapolate with confidence from existing data.

So far in this work, the effects of carrier density on material parameters have not been explored. Due to the effects of pump current spatial distribution and spatially-dependent carrier depletion by stimulated emission, carrier densities may very significantly both spatially and temporally. Carrier density is known to have an effect on a material's refractive index as well as on its nonlinear coefficients, so both mechanisms may affect the time-dependent behavior of nanolasers.

Due to the current use of a different simulation program for the electrical portion of the simulations, as well as to the slowness of 3D optical simulation (up to several hours for the largest lasers), a closed-loop simulation program would need to be substantially different from the existing solution. By restricting the nanolaser to the smallest size, with a circularly-symmetric TE_{01} mode, the optical modeling could use 2D symmetry, substantially reducing solution time at the expense of flexibility.

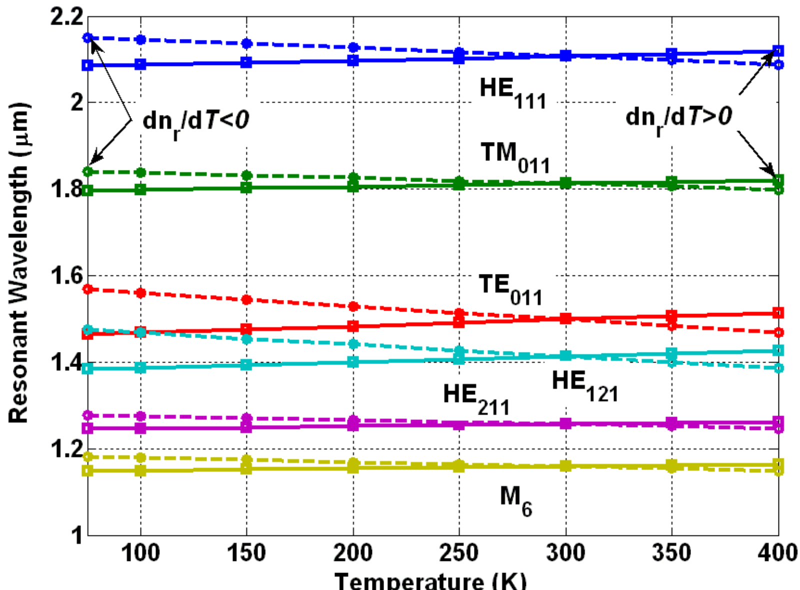

Figure 7.3: Resonant wavelength of selected modes of a nanolaser with r_{core}=250nm and a SiO_2 shield of thickness t_{shield}=100nm.

7.4 Experimental measurement of laser operating temperature

It is of strong interest in nanolaser studies to be able to measure the operating temperature of the gain region interior. However, this has so far proved a challenge due to the small size of the cavity and to the large temperature gradients that exist between different regions of the nanolaser.

By monitoring the shifting wavelength of cavity modes (Fig. 7.3), the amount of temperature-dependent refractive index and bandgap change in the cavity can be inferred. The amplified spontaneous emission from these cavity modes may only be narrow enough for this technique when the device is near threshold, meaning that measuring the amount of temperature rise from ambient may prove difficult. However, if a passive technique of measuring cavity resonance can be used, for example, through absorption, this wavelength shift might be calibrated with the use of a temperature-controlled stage or chamber.

7.5 Investigation of strain gradients

The thermal simulations reported in Chapter 6 revealed that under the conditions of high operating temperature and low shield thermal conductivity, strong temperature gradients can appear in the dielectric shield layer. These temperature gradients, or even a large rise in overall temperature for a laser made of materials with different thermal expansion coefficients, can lead to thermal strain. The mechanical stresses introduced by thermal strain are already suspected to be a cause of laser failure[8]. It would be useful in future investigations to determine the failure points of the materials that make up a nanolaser, as well as the strength of the strain-induced optical changes.

Thermally-induced strain may also induce high nonlinear coefficients that may be of use in wavelength conversion and modulation. Some commonly-used shield materials such as silicon nitride and silicon dioxide have already been used to strain silicon for use in nonlinear optics devices[91].

7.6 Acknowledgements

The SEM images in Fig. 7.2 were taken by Qing Gu, from lasers she designed and fabricated. The 3D COMSOL modelling results for these two lasers, shown in Fig. 7.2 and described in the associated text, were performed by summer REU student Alan Potterton under the supervision of Janelle Shane.

Fig. 7.3 is a reprint of simulations by Joseph Smalley, which appears in a paper currently accepted for publication in Nanophotonics Journal, 2014. Qing Gu, Joseph S. T. Smalley, Janelle Shane, Olesya Bondarenko and Yeshaiahu Fainman. (2014) The dissertation author was an author of this review paper.

Bibliography

[1] B. R. Koch, E. J. Norberg, B. Kim, J. Hutchinson, J.-H. Shin, G. Fish, and A. Fang, "Integrated Silicon Photonic Laser Sources for Telecom and Datacom," in *Optical Fiber Communication Conference and Exposition and the National Fiber Optic Engineers Conference (OFC/NFOEC), 2013*, pp. 1–3, 2013.

[2] G. Roelkens, L. Liu, D. Liang, R. Jones, A. Fang, B. Koch, and J. Bowers, "III-V/silicon photonics for on-chip and intra-chip optical interconnects," *Laser & Photonics Reviews* **4**, pp. 751–779, Jan. 2010.

[3] O. Bondarenko, Q. Gu, J. Shane, A. Simic, B. Slutsky, and Y. Fainman, "Wafer bonded distributed feedback laser with sidewall modulated Bragg gratings," *Applied Physics Letters* **103**(4), p. 043105, 2013.

[4] Q. Gu, B. Slutsky, F. Vallini, J. S. T. Smalley, M. P. Nezhad, N. C. Frateschi, and Y. Fainman, "Purcell effect in sub-wavelength semiconductor lasers," *Optics Express* **21**(13), p. 15603, 2013.

[5] G. Björk, A. Karlsson, and Y. Yamamoto, "Definition of a laser threshold," *Physical Review A* **50**(2), p. 1675, 1994.

[6] C. Z. Ning, "What is Laser Threshold?," *IEEE Journal of Selected Topics in Quantum Electronics* **19**, pp. 1503604–1503604, May 2013.

[7] M. T. Hill, Y.-S. Oei, B. Smalbrugge, Y. Zhu, T. de Vries, P. J. van Veldhoven, F. W. M. van Otten, T. J. Eijkemans, J. P. Turkiewicz, H. de Waardt, E. J. Geluk, S.-H. Kwon, Y.-H. Lee, R. Nötzel, and M. K. Smit, "Lasing in metallic-coated nanocavities," *Nature Photonics* **1**, pp. 589–594, Sept. 2007.

[8] K. Ding and C. Z. Ning, "Fabrication challenges of electrical injection metallic cavity semiconductor nanolasers," *Semiconductor Science and Technology* **28**, p. 124002, Nov. 2013.

[9] J. S. T. Smalley, Q. Gu, and Y. Fainman, "Temperature Dependence of the Spontaneous Emission Factor in Subwavelength Semiconductor Lasers," *IEEE Journal of Quantum Electronics* **50**, pp. 175–185, Mar. 2014.

[10] S. L. McCall, A. F. J. Levi, R. E. Slusher, S. J. Pearton, and R. A. Logan, "Whispering-gallery mode microdisk lasers," *Applied Physics Letters* **60**(3), p. 289, 1992.

[11] D. J. Gargas, M. C. Moore, A. Ni, S.-W. Chang, Z. Zhang, S. L. Chuang, and P. Yang, "Whispering Gallery Mode Lasing from Zinc Oxide Hexagonal Nanodisks," *ACS Nano* **4**, pp. 3270–3276, June 2010.

[12] J. Hofrichter, O. Raz, L. Liu, G. Morthier, F. Horst, P. Regreny, T. De Vries, H. J. S. Dorren, and B. J. Offrein, "All-optical wavelength conversion using mode switching in InP microdisc laser," *Electronics Letters* **47**(16), p. 927, 2011.

[13] Q. Song, H. Cao, S. T. Ho, and G. S. Solomon, "Near-IR subwavelength microdisk lasers," *Applied Physics Letters* **94**(6), p. 061109, 2009.

[14] R. F. Oulton, V. J. Sorger, T. Zentgraf, R.-M. Ma, C. Gladden, L. Dai, G. Bartal, and X. Zhang, "Plasmon lasers at deep subwavelength scale," *Nature* **461**, pp. 629–632, Jan. 2009.

[15] Y. J. Lu, J. Kim, H. Y. Chen, C. Wu, N. Dabidian, C. E. Sanders, C. Y. Wang, M. Y. Lu, B. H. Li, X. Qiu, W. H. Chang, L. J. Chen, G. Shvets, C. K. Shih, and S. Gwo, "Plasmonic Nanolaser Using Epitaxially Grown Silver Film," *Science* **337**, pp. 450–453, July 2012.

[16] W. Zhou and Z. Ma, "Breakthroughs in Photonics 2012: Breakthroughs in Nanomembranes and Nanomembrane Lasers," *IEEE Photonics Journal* **5**, p. 0700707, Mar. 2013.

[17] K.-Y. Jeong, Y.-S. No, Y. Hwang, K. S. Kim, M.-K. Seo, H.-G. Park, and Y.-H. Lee, "Electrically driven nanobeam laser," *Nature Communications* **4**, pp. 1–6, Nov. 2013.

[18] M. T. Hill, M. Marell, E. S. Leong, B. Smalbrugge, Y. Zhu, M. Sun, P. J. van Veldhoven, E. J. Geluk, F. Karouta, and Y.-S. Oei, "Lasing in metal-insulator-metal sub-wavelength plasmonic waveguides," *Optics Express* **17**(13), pp. 11107–11112, 2009.

[19] K. Ding, M. T. Hill, Z. C. Liu, L. J. Yin, P. J. van Veldhoven, and C. Z. Ning, "Record performance of electrical injection sub-wavelength metallic-cavity semiconductor lasers at room temperature," *Optics Express* **21**(4), pp. 4728–4733, 2013.

[20] M. P. Nezhad, A. Simic, O. Bondarenko, B. Slutsky, A. Mizrahi, L. Feng, V. Lomakin, and Y. Fainman, "Room-temperature subwavelength metallo-dielectric lasers," *Nature Photonics* **4**, pp. 395–399, Apr. 2010.

[21] A. Mizrahi, V. Lomakin, B. A. Slutsky, M. P. Nezhad, L. Feng, and Y. Fainman, "Low threshold gain metal coated laser nanoresonators," *Optics Letters* **33**(11), pp. 1261–1263, 2008.

[22] J. H. Lee, M. Khajavikhan, A. Simic, Q. Gu, O. Bondarenko, B. Slutsky, M. P. Nezhad, and Y. Fainman, "Electrically pumped sub-wavelength metallo-dielectric pedestal pillar lasers," *Optics Express* **19**, pp. 21524–21531, Oct. 2011.

[23] Q. Gu, J. Shane, F. Vallini, B. Wingad, J. S. Smalley, N. C. Frateschi, and Y. Fainman, “Amorphous Al_2O_3 shield for thermal management in electrically pumped metallo-dielectric nanolasers,” *IEEE Journal of Quantum Electronics* **50**, pp. 499–509, July 2014.

[24] F. Vallini, Q. Gu, M. Kats, Y. Fainman, and N. C. Frateschi, “Carrier saturation in multiple quantum well metallo-dielectric semiconductor nanolaser: Is bulk material a better choice for gain media?,” *Optics Express* **21**(22), p. 25985, 2013.

[25] M. Khajavikhan, A. Simic, M. Katz, J. H. Lee, B. Slutsky, A. Mizrahi, V. Lomakin, and Y. Fainman, “Thresholdless nanoscale coaxial lasers,” *Nature* **482**, pp. 204–207, Jan. 2012.

[26] O. Hess, J. B. Pendry, S. A. Maier, R. F. Oulton, J. M. Hamm, and K. L. Tsakmakidis, “Active nanoplasmonic metamaterials,” *Nature Materials* **11**, pp. 573–584, July 2012.

[27] W. S. Hobson, U. Mohideen, S. J. Pearton, R. E. Slusher, and F. Ren, “SiN x/sulphide passivated GaAs/AlGaAs microdisk lasers,” *Electronics Letters* **29**(25), pp. 2199–2200, 1993.

[28] K. Ding and C. Z. Ning, “Metallic subwavelength-cavity semiconductor nanolasers,” *Light: Science & Applications* **1**, p. e20, July 2012.

[29] C. Z. Ning, R. A. Indik, and J. V. Moloney, “Self-consistent approach to thermal effects in vertical-cavity surface-emitting lasers,” *JOSA B* **12**(10), pp. 1993–2004, 1995.

[30] S. F. Yu, *Analysis and design of vertical cavity surface emitting lasers*, Wiley - VCH, Jan. 2003.

[31] N. M. Schmidt and Y. A. Goldberg, Handbook Series on Semiconductor Parameters *Volume 2: Ternary And Quaternary III-V Compounds*, vol. 2 of *Handbook Series on Semiconductor Parameters*, World Scientific, London, Jan. 1996.

[32] N. M. Schmidt and Y. A. Goldberg, Handbook Series on Semiconductor Parameters *Volume 1: Si, Ge, C (Diamond), GaAs, GaP, GaSb, InAs, InP, InSb*, vol. 1 of *Handbook Series on Semiconductor Parameters*, World Scientific, London, Jan. 1996.

[33] P. Zhang, Y. Y. Lau, W. Tang, M. R. Gomez, D. M. French, J. C. Zier, and R. M. Gilgenbach, “Contact resistance with dissimilar materials: bulk contacts and thin film contacts,” in *Electrical Contacts (Holm), 2011 IEEE 57th Holm Conference on*, pp. 1–6, IEEE, Sept. 2011.

[34] G. P. Agrawal and N. K. Dutta, *Semiconductor lasers*, Van Nostrand Reinhold, New York, Jan. 1993.

[35] S. Yoneoka, J. Lee, M. Liger, G. Yama, T. Kodama, M. Gunji, J. Provine, R. T. Howe, K. E. Goodson, and T. W. Kenny, “Electrical and Thermal Conduction in Atomic Layer Deposition Nanobridges Down to 7 nm Thickness,” *Nano letters* **12**, pp. 683–686, Feb. 2012.

[36] J. R. Wank, S. M. George, and A. W. Weimer, "Nanocoating individual cohesive boron nitride particles in a fluidized bed by ALD," *Powder Technology* **142**, pp. 59–69, Apr. 2004.

[37] E. Dörre and H. Hübner, *Alumina: processing, properties, and applications*, Springer-Verlag, Berlin, Jan. 1984.

[38] M. B. Kleiner, S. A. Kuhn, and W. Weber, "Thermal conductivity measurements of thin silicon dioxide films in integrated circuits," *Electron Devices, IEEE Transactions on* **43**(9), pp. 1602–1609, 1996.

[39] S. Adachi, Physical Properties of III-V Semiconductor Compounds, John Wiley & Sons, Inc., Mörlenbach, Jan. 1992.

[40] N. A. Lange, *Lange's Handbook of Chemistry*, McGraw-Hill Professional, 15 ed., Jan. 1999.

[41] S. Andersson and L. Dzhavadov, "Thermal conductivity and heat capacity of amorphous SiO2: pressure and volume dependence," *Journal of Physics: Condensed Matter* **4**(29), p. 6209, 1992.

[42] D. R. Lide, *CRC Handbook of Chemistry and Physics*, CRC Press, 84 ed., June 2003.

[43] E. Bassous, "Fabrication of novel three-dimensional microstructures by the anisotropic etching of (100) and (110) silicon," *IEEE Transactions on Electron Devices* **25**, pp. 1178–1185, Oct. 1978.

[44] D. G. Cahill, "Thermal conductivity measurement from 30 to 750 K: the 3ω method," *Review of Scientific Instruments* **61**(2), p. 802, 1990.

[45] D. G. Cahill, M. Katiyar, and J. R. Abelson, "Thermal conductivity of alpha-Si:H thin films," *Physical Review B* **50**(9), p. 6077, 1994.

[46] T. Borca-Tasciuc, A. R. Kumar, and G. Chen, "Data reduction in 3ω method for thin-film thermal conductivity determination," *Review of Scientific Instruments* **72**(4), p. 2139, 2001.

[47] R. Y. Wang, R. A. Segalman, and A. Majumdar, "Room temperature thermal conductance of alkanedithiol self-assembled monolayers," *Applied Physics Letters* **89**(17), p. 173113, 2006.

[48] A. Majumdar, "Scanning thermal microscopy," *Annual review of materials science* **29**(1), pp. 505–585, 1999.

[49] K. Kim, W. Jeong, W. Lee, and P. Reddy, "Ultra-High Vacuum Scanning Thermal Microscopy for Nanometer Resolution Quantitative Thermometry," *ACS Nano* **6**, pp. 4248–4257, May 2012.

[50] S. Shen, A. Henry, J. Tong, R. Zheng, and G. Chen, "Polyethylene nanofibres with very high thermal conductivities," *Nature Nanotechnology* , pp. 1–5, Mar. 2010.

[51] T. Luo and G. Chen, "Nanoscale heat transfer – from computation to experiment," *Physical Chemistry Chemical Physics* **15**(10), pp. 3389–3412, 2013.

[52] J. Y. Suh, C. H. Kim, W. Zhou, M. D. Huntington, D. T. Co, M. R. Wasielewski, and T. W. Odom, "Plasmonic Bowtie Nanolaser Arrays," *Nano Lett* **12**, pp. 5769–5774, Nov. 2012.

[53] M.-K. Kim, Z. Li, K. Huang, R. Going, M. C. Wu, and H. Choo, "Engineering of metal-clad optical nanocavity to optimize coupling with integrated waveguides," *Optics Express* **21**(22), p. 25796, 2013.

[54] J. S. T. Smalley, M. W. Puckett, and Y. Fainman, "Invariance of optimal composite waveguide geometries with respect to permittivity of the metal cladding," *Optics Letters* **38**(23), p. 5161, 2013.

[55] B. M. Green, K. K. Chu, E. M. Chumbes, J. A. Smart, J. R. Shealy, and L. F. Eastman, "The effect of surface passivation on the microwave characteristics of undoped AlGaN/GaN HEMTs," *Electron Device Letters, IEEE* **21**(6), pp. 268–270, 2000.

[56] M. P. Nezhad, K. Tetz, and Y. Fainman, "Gain assisted propagation of surface plasmon polaritons on planar metallic waveguides," *Optics Express* **12**(17), pp. 4072–4079, 2004.

[57] M. H. Shih, M. Bagheri, A. Mock, S. J. Choi, J. D. O'Brien, P. D. Dapkus, and W. Kuang, "Identification of modes and single mode operation of sapphire-bonded photonic crystal lasers under continuous-wave room temperature operation," *Applied Physics Letters* **90**(12), p. 121116, 2007.

[58] S. Chu, G. Wang, W. Zhou, Y. Lin, L. Chernyak, J. Zhao, J. Kong, L. Li, J. Ren, and J. Liu, "Electrically pumped waveguide lasing from ZnO nanowires," *Nature Nanotechnology* **6**, pp. 506–510, July 2011.

[59] B. Min, J. S. Lee, K. Cho, J. W. Hwang, H. Kim, M. Y. Sung, S. Kim, J. Park, H. W. Seo, and S. Y. Bae, "Semiconductor nanowires surrounded by cylindrical Al_2O_3 shells," *Journal of Electronic Materials* **32**(11), pp. 1344–1348, 2003.

[60] S. M. Lee and D. G. Cahill, "Heat transport in thin dielectric films," *Journal of Applied Physics* **81**(6), p. 2590, 1997.

[61] M. T. Alam, M. P. Manoharan, M. A. Haque, C. Muratore, and A. Voevodin, "Influence of strain on thermal conductivity of silicon nitride thin films," *Journal of Micromechanics and Microengineering* **22**, p. 045001, Mar. 2012.

[62] X. Duan, Y. Huang, R. Agarwal, and C. M. Lieber, "Single-nanowire electrically driven lasers," *Nature* **421**(6920), pp. 241–245, 2003.

[63] M. W. Kim and P. C. Ku, "Semiconductor nanoring lasers," *Applied Physics Letters* **98**(20), p. 201105, 2011.

[64] H. Yang, D. Zhao, S. Chuwongin, J.-H. Seo, W. Yang, Y. Shuai, J. Berggren, M. Hammar, Z. Ma, and W. Zhou, "Transfer-printed stacked nanomembrane lasers on silicon," *Nature Photonics* **6**, pp. 615–620, July 2012.

[65] B. Hoex, S. B. S. Heil, E. Langereis, M. C. M. van de Sanden, and W. M. M. Kessels, "Ultralow surface recombination of c-Si substrates passivated by plasma-assisted atomic layer deposited Al_2O_3," *Applied Physics Letters* **89**(4), p. 042112, 2006.

[66] U. Khalique, M. Marell, F. Karouta, W. Keuning, W. Kessels, M. T. Hill, and M. K. Smit, "Investigation of Al_2O_3Deposited by ALD as Passivation Layers for InP-based Nano Lasers," *Proceedings Symposium IEEE/LEOS* , pp. 195–198, 2008.

[67] Q. Gu, B. Wingad, F. Vallini, B. Slutsky, M. Katz, M. P. Nezhad, N. C. Frateschi, and Y. Fainman, "Electrically pumped metallo-dielectric pedestal nanolasers," in *2013 Conference on Lasers and Electro-Optics Pacific Rim (CLEO-PR)*, Optical Society of America, 2013.

[68] K. Ding, Z. C. Liu, L. J. Yin, M. T. Hill, M. J. H. Marell, P. J. van Veldhoven, R. Nöetzel, and C. Z. Ning, "Room-temperature continuous wave lasing in deep-subwavelength metallic cavities under electrical injection," *Physical Review B* **85**, p. 041301, Jan. 2012.

[69] J.-S. G. Bouillard, W. Dickson, D. P. O'Connor, G. A. Wurtz, and A. V. Zayats, "Low-Temperature Plasmonics of Metallic Nanostructures," *Nano letters* **12**, pp. 1561–1565, Mar. 2012.

[70] G. R. Parkins, W. E. Lawrence, and R.-W. Christy, "Intraband optical conductivity σ (ω, T) of Cu, Ag, and Au: Contribution from electron-electron scattering," *Physical Review B* **23**(12), p. 6408, 1981.

[71] P. B. Johnson and R.-W. Christy, "Optical constants of the noble metals," *Physical Review B* **6**(12), p. 4370, 1972.

[72] D. R. Cassidy and G. H. Cross, "Universal method to determine the thermo-optic coefficient of optical waveguide layer materials using a dual slab waveguide," *Applied Physics Letters* **91**(14), p. 141914, 2007.

[73] F. G. Della Corte, G. Cocorullo, M. Iodice, and I. Rendina, "Temperature dependence of the thermo-optic coefficient of InP, GaAs, and SiC from room temperature to 600 K at the wavelength of 1.5 μm," *Applied Physics Letters* **77**(11), p. 1614, 2000.

[74] A. Matsudaira, C.-Y. Lu, M. Zhang, S. L. Chuang, E. Stock, and D. Bimberg, "Cavity-Volume Scaling Law of Quantum-Dot Metal-Cavity Surface-Emitting Microlasers," *IEEE Photonics Journal* **4**(4), pp. 1103–1114.

[75] A. Forchel, B. Menschig, B. E. Maile, H. Leier, and R. Germann, "Transport and optical properties of semiconductor quantum wires," *Journal of Vacuum Science & Technology B: Microelectronics and Nanometer Structures* **9**, p. 444, Mar. 1991.

[76] S. Shin, H. N. Cho, B. S. Kim, and H. H. Cho, "Influence of upper layer on measuring thermal conductivity of multilayer thin films using differential 3-ω method," *Thin Solid Films* **517**, pp. 933–936, Nov. 2008.

[77] K. J. Chen and S. Huang, "AlN passivation by plasma-enhanced atomic layer deposition for GaN-based power switches and power amplifiers," *Semiconductor Science and Technology* **28**, p. 074015, June 2013.

[78] G. Chen and A. Shakouri, "Heat Transfer in Nanostructures for Solid-State Energy Conversion," *Journal of Heat Transfer* **124**(2), p. 242, 2002.

[79] A. V. Maslov and C.-Z. Ning, "Metal-encased semiconductor nanowires as waveguides for ultrasmall lasers," *2007 Conference on Lasers and Electro-Optics (CLEO)* , p. JWA121, 2007.

[80] A. V. Maslov and C. Z. Ning, "Size reduction of a semiconductor nanowire laser by using metal coating," *Proceedings of the SPIE - The Physics and Simulation of Optoelectronic Devices XV* **6468**, p. 64680I, 2007.

[81] M. J. H. Marell, *Gap plasmon mode distributed feedback lasers.* PhD thesis, Eindhoven University of Technology, May 2011.

[82] Z. Liu, J. M. Shainline, G. E. Fernandes, J. Xu, J. Chen, and C. F. Gmachl, "Continuous-wave subwavelength microdisk lasers at λ= 1.53 μm," *Optics Express* **18**, pp. 19242–19248, Aug. 2010.

[83] J. Shane, Q. Gu, F. Vallini, B. Wingad, J. S. T. Smalley, N. C. Frateschi, and Y. Fainman, "Thermal considerations in electrically-pumped metallo-dielectric nanolasers," in *SPIE OPTO*, B. Witzigmann, M. Osinski, F. Henneberger, and Y. Arakawa, eds., p. 898027, SPIE, Mar. 2014.

[84] P. Zhang and Y. Y. Lau, "An exact field solution of contact resistance and comparison with the transmission line model," *Applied Physics Letters* **104**, p. 204102, May 2014.

[85] K. Ding, L. Yin, M. T. Hill, Z. Liu, P. J. van Veldhoven, and C. Z. Ning, "An electrical injection metallic cavity nanolaser with azimuthal polarization," *Applied Physics Letters* **102**(4), p. 041110, 2013.

[86] J. Shane, Q. Gu, A. Potterton, and Y. Fainman, "Effect of undercut etch on performance and fabrication robustness of metal-clad semiconductor nanolasers." Aug. 2014.

[87] K. Ikeda, R. E. Saperstein, N. Alic, and Y. Fainman, "Thermal and Kerr nonlinear properties of plasma-deposited silicon nitride/ silicon dioxide waveguides," *Optics Express* **16**(17), p. 12987, 2008.

[88] B. L. Zink and F. Hellman, "Specific heat and thermal conductivity of low-stress amorphous Si–N membranes," *Solid State Communications* **129**, pp. 199–204, Jan. 2004.

[89] M. Bosund, T. Sajavaara, M. Laitinen, T. Huhtio, M. Putkonen, V.-M. Airaksinen, and H. Lipsanen, "Properties of AlN grown by plasma enhanced atomic layer deposition," *Applied Surface Science* **257**, pp. 7827–7830, June 2011.

[90] R. Kato, A. Maesono, and R. P. Tye, "Thermal conductivity measurement of submicron-thick films deposited on substrates by modified ac calorimetry (laser-heating Angstrom method)," *International Journal of Thermophysics* **22**, pp. 617–629, Mar. 2001.

[91] R. S. Jacobsen, K. N. Andersen, P. I. Borel, J. Fage-Pedersen, L. H. Frandsen, O. Hansen, M. Kristensen, A. V. Lavrinenko, G. Moulin, H. Ou, C. Peucheret, B. Zsigri, and A. Bjarklev, "Strained silicon as a new electro-optic material," *Nature* **441**, pp. 199–202, May 2006.